Survey Paper

Recent advances in diffusion MRI modeling: Angular and radial reconstruction

Haz-Edine Assemlal [a,*], David Tschumperlé [b], Luc Brun [b], Kaleem Siddiqi [a]

[a] School of Computer Science & Center for Intelligent Machines, McGill University, 3480 University Street, Montréal, QC, Canada H3A2A7
[b] GREYC (CNRS UMR 6072), 6 Bd Maréchal Juin, 14050 Caen Cedex, France

ARTICLE INFO

ABSTRACT

Recent advances in diffusion magnetic resonance image (dMRI) modeling have led to the development of several state of the art methods for reconstructing the diffusion signal. These methods allow for distinct features to be computed, which in turn reflect properties of fibrous tissue in the brain and in other organs. A practical consideration is that to choose among these approaches requires very specialized knowledge. In order to bridge the gap between theory and practice in dMRI reconstruction and analysis we present a detailed review of the dMRI modeling literature. We place an emphasis on the mathematical and algorithmic underpinnings of the subject, categorizing existing methods according to how they treat the angular and radial sampling of the diffusion signal. We describe the features that can be computed with each method and discuss its advantages and limitations. We also provide a detailed bibliography to guide the reader.

© 2011 Elsevier B.V. All rights reserved.

1. Introduction

1.1. Context

Diffusion magnetic resonance imaging (dMRI) allows one to examine the microscopic diffusion of water molecules in biological tissue *in vivo*. Water molecules are in constant thermal motion, with a locally random component, but this motion is constrained by the presence of surrounding structures including nerves, cells and surrounding tissue. Measurements of this diffusion, therefore, reveal micro-structural properties of the underlying tissue. In practice, this imaging modality requires the collection of successive images with magnetic field gradients applied in different directions. A reconstruction step is then used to estimate the 3D diffusion probability density function (PDF) from the acquired images.

Since the development of the first dMRI acquisition sequence in the mid 1960s, many applications of this modality have emerged. These can be classified into two main categories. The first category aims at diagnosing certain brain abnormalities that alter the dynamics of the diffusion of water in the brain, *e.g.*, as in the case of a stroke. Such changes can be detected very easily in diffusion images, but remain invisible in other "static" imaging modalities, *e.g.*, anatomical MRI and CT. The dMRI has been increasingly exploited by neurologists for the diagnosis of a wide variety of brain pathologies including: tumors (cerebral lymphoma, epidermoid and cholesteatoma cysts), infections (pyogenic brain abscess, encephalitis herpes); degenerative diseases (Creutzfeld–Jakob

Disease); inflammatory conditions (multiple sclerosis), and trauma (shock, fracture) (Ron and Robbins, 2003; Moritani et al., 2004).

The second class of applications of dMRI focus on the study of the neuroanatomy of the human brain and more specifically on the understanding of its microstructure. In a diffusion image, each voxel has a signal which results from the motion of a large number of water molecules, revealing features of a portion of tissue at an atomic scale. Early in the dMRI literature it became apparent that this summary of local diffusion depends on attributes of the vector magnetic field gradient, and how it affects the profile of the diffusion signal in both the angular and radial directions. However, the hardware requirements being demanding for MRI scanners of that time, it was not until the early nineties that this kind of imaging could be initiated.

The founding method in this area is Diffusion Tensor Imaging (DTI), where a second-order tensor **D** is used to model the PDF within a voxel, a model which is adequate when there is a single coherent fibers population present. This tensor may be visualized as an ellipsoid with its three axes given by the eigenvectors of **D**, scaled by their corresponding eigenvalues. The eigenvector with the largest eigenvalue reflects the orientation of the fiber population. The extraction of further information from DTI can then take several forms, such as scalar factional anisotropy indices which express the degree to which diffusion is restricted to particular directions at a voxel.

Advances in MRI now enable one to acquire dMRI images with a larger number of magnetic field gradient diffusion encoding directions, typically 64–100, compared to the six directions that are the minimum necessary for DTI. With such angular sampling, the tensor formulation can be replaced with mathematical models of

* Corresponding author.
E-mail address: assemlal@cim.mcgill.ca (H.-E. Assemlal).

higher dimension, leading to high angular resolution diffusion imaging (HARDI) reconstructions. These models allow for better detection and representation of complex sub-voxel fiber geometries. From HARDI it is in fact possible to obtain a more accurate fiber orientation distribution function (ODF) within a voxel without a prior assumption on the number of fiber populations present, via a spherical deconvolution method (Tournier et al., 2004). There is also a growing interest in the development of tractography algorithms to group such local estimates to reconstruct complete fiber tract systems (Mori et al., 1999). Typical examples of such algorithms are described in the recent proceedings of the 2009 MICCAI Diffusion Modeling and Fiber Cup Workshop. With such algorithms in hand, it becomes possible to not only recover connectivity patterns between distinct anatomical regions in the human brain, but also to define continuous measures of the degree of connectivity between two such regions.

Whereas the reconstruction of a more precise angular diffusion profile has been the subject of much work in the dMRI community, the study of the radial profile of the diffusion signal has also been carried out using nuclear magnetic resonance (NMR) spectroscopy in place of existing MRI scanners. Spectrometers can be used to acquire radial diffusion profiles with great accuracy, but at the expense of being limited to a small, spatially unresolved, sample. The use of this method reveals a phenomenon of "diffusion–diffraction" caused by the interference between water molecules and the walls of the microscopic structures within biological tissue. From the observation of this phenomenon, it is theoretically possible to extract features *in vivo* of brain structure at a microscopic scale, including average cell size, axon diameter, probability of diffusion permeability of the walls, *etc.*

This article presents an in depth review of the diffusion MRI reconstruction and modeling literature, including low angular resolution methods, high angular resolution methods, methods to sample the radial component of the diffusion signal and methods to combine both angular and radial sampling. Our intent is to provide a comprehensive treatment while emphasizing the mathematical and algorithmic underpinnings of each method. We begin by introducing the necessary mathematical background. We first define the notation used throughout this paper in Section 1.2. We briefly present the scanner sequence used in dMRI to acquire the signal in Sections 1.3 and 1.4, which is widely described using two formalisms: the Stejskal–Tanner equation (Section 1.5) and the *q*-space formalism (Section 1.6). We then review the typical shape of the diffusion signal in the literature in Section 1.7.

1.2. Notation

Let $\Omega_x \subset \mathbb{R}^3$ be the position space (**x**-space), a vector space of dimension 3, whose natural orthonormal basis is the family of vectors $\{\mathbf{e}_x = (1,0,0), \mathbf{e}_y = (0,1,0), \mathbf{e}_z = (0,0,1)\}$. Let $\mathbf{x} \in \Omega_x$ be a vector so that the coordinates are expressed as $\mathbf{x} = (x,y,z)^T$. Similarly, we define the diffusion space $\Omega_q \subset \mathbb{R}^3$ (*q*-space) so that the natural orthonormal basis is now $\{\mathbf{u}_x, \mathbf{u}_y, \mathbf{u}_z\}$ and a vector $\mathbf{q} \in \Omega_q$. We model the diffusion MR image as a continuous function E:

$$E : \begin{vmatrix} \Omega_x \times \Omega_q \to \mathbb{R} \\ (\mathbf{x}, \mathbf{q}) \to E(\mathbf{x}, \mathbf{q}) \end{vmatrix} \tag{1}$$

The Fig. 1 illustrate Eq. (1), so that each couple $(\mathbf{x}, \mathbf{q})$, respectively, describing the spatial and the diffusion coordinates, is associated with a diffusion value $E(\mathbf{x}, \mathbf{q})$. For the sake of simplify, we use the equivalent notation $E(\mathbf{q}) = E(\mathbf{x}, \mathbf{q})$ to refer to the diffusion signal inside any voxel $\mathbf{x} \in \Omega_x$ of the image. In the next sections, we detail the acquisition of the position space Ω_x and the diffusion space Ω_q.
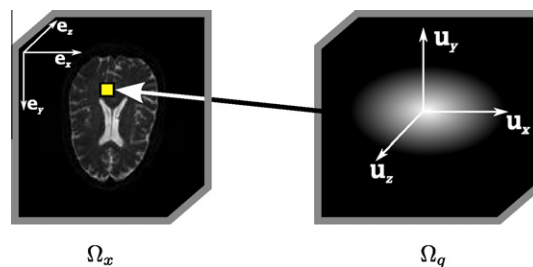

Fig. 1. Our mathematical definition of the diffusion MRI image as expressed in Eq. (1). Left: the position **x**-space Ω_x of the image, which results as the Fourier transform of the acquired *k*-space. Right: the diffusion *q*-space Ω_q for one voxel of the **x**-space (depicted here as a yellow rectangle). (For interpretation of the references to colour in this figure legend, the reader is referred to the web version of this article.)

1.3. Imaging the k-space

The MRI scanner acquires the three-dimensional anatomical image I on a slice-by-slice basis. Let $\Omega_k \subset \mathbb{R}^2$ be the *k*-space (Ljunggren, 1983), a vector space of dimension 2, so that the acquired image I is modeled as the function:

$$I : \begin{vmatrix} \Omega_k \times \mathbb{R} \times \Omega_q \to \mathbb{R} \\ (\mathbf{k}, z, \mathbf{q}) \to I(\mathbf{k}, z, \mathbf{q}) \end{vmatrix} \tag{2}$$

where $\mathbf{k} = (k_x, k_y) \in \Omega_k$ is a vector of the *k*-space proportional to the areas of the imaging gradients and z is the third coordinate of the vector $\mathbf{x} \in \Omega_x$. The gradients are applied along each slice z of the image I; this creates a gradient in the spin phases within this slice and enables one to locate each spin of the image I at coordinates $(\mathbf{k}, z)$. We are interested in the ensemble magnetization vectors image S which characterizes the brain tissue at each voxel **x**. The image S is given by the two-dimensional Fourier transform $\mathcal{F}_{2D}$ of the image I:

$$S(\mathbf{x}, \mathbf{q}) = \int_{\mathbf{k} \in \Omega_k} I(\mathbf{k}, z, \mathbf{q}) \exp(-i2\pi\mathbf{k} \cdot \mathbf{x}_{xy}) d\mathbf{k} \tag{3}$$

where $\mathbf{x}_{xy} = (x, y)$ is a two-dimensional vector so that $\mathbf{x} = (\mathbf{x}_{xy}, z)$. Therefore, if the image is acquired in the *k*-space sampling with sufficient samples of **k** in each slice z, we can recover the image S as illustrated in Fig. 2. For more details on the encoding of the image by MRI magnetic field gradients, readers can refer to (Pipe, 2009). In addition to this anatomical MRI sequence presented in this section, the imaging of the diffusion requires an additional specific acquisition sequence.

1.4. Diffusion gradient sequence

The classical acquisition sequence used in dMRI is the gradient pulsed spin echo (PGSE), introduced by Stejskal and Tanner (1965). This sequence can be explained as follows (as illustrated in Fig. 3):

- the first diffusion gradient pulse $\mathbf{g}(0)$ "labels" the spins of water molecules according to their initial positions at $t = 0$;
- after the 180° radio-frequency signal (which causes an adjustment in spin phases at echo time TE), a second diffusion gradient pulse $\mathbf{g}(\Delta)$ is applied which labels the spins after a diffusion time $t = \Delta$;
- the scanner coils receive the diffusion signal at echo time $t = TE$ and two situations are possible at this point: either the water molecules did not move, so that the spin labels cancel out each other; or some molecules moved during the diffusion time lapse, which leads to a signal loss proportional to the displacement of water molecules.
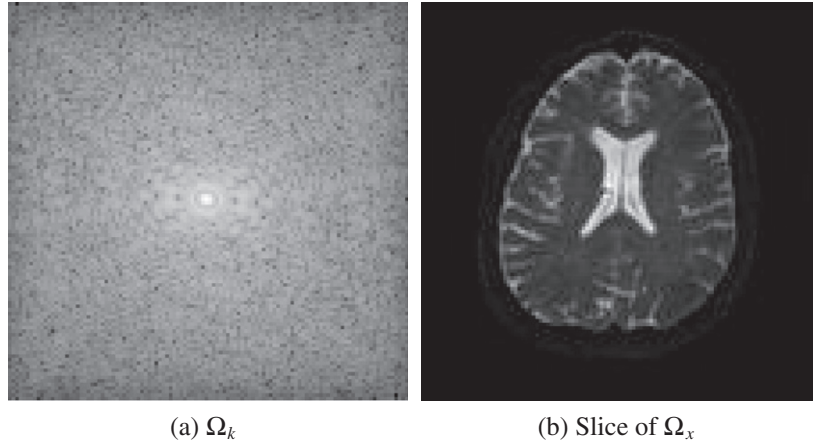
(a) Ω_k

(b) Slice of Ω_x

Fig. 2. Acquisition of a slice of the MRI image. (a) Acquisition is done in the *k*-space on a slice-by-slice basis. (b) Module of the Fourier transform of the image (a).
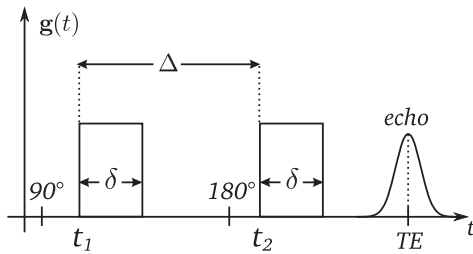

Fig. 3. Pulsed Gradient Spin Echo (PGSE) sequence proposed by Stejskal and Tanner (1965). The echo formation, resulting in the diffusion signal, is acquired at the echo time *TE* after the 90° and 180° radio-frequency pulses.

The diffusion gradient **g** sequence is expressed as a function of time (Stejskal and Tanner, 1965):

$$\mathbf{g}(t) = (H(t_1) - H(t_1 - \delta) + H(t_2) - H(t_2 - \delta))\mathbf{u}, \quad (4)$$

where $t_2 = t_1 + \Delta$, the symbol H being the Heaviside step function and $\mathbf{u} \in \mathcal{S}^2$ representing the gradient direction.

1.5. Unbounded diffusion

The diffusion signal received by the scanner coils was first described by Stejskal and Tanner (1965). Indeed, the incorporation of **g** from Eq. (4) into the Bloch–Torrey equations (Torrey, 1956) leads to the signal attenuation equation as given by Stejskal and Tanner (1965):

$$E(b) = \frac{S(b)}{S(0)} = \exp\left(-\gamma^2\delta^2\left(\Delta - \frac{\delta}{3}\right)\mathbf{g}^{\mathrm{T}}\mathbf{D}\mathbf{g}\right), \quad (5)$$

This equation relates the normalized signal decay E at echo time $t = TE$ with the duration, time separation and strength of the magnetic field pulse gradients (δ, Δ and g, respectively), γ the gyromagnetic ratio, and the apparent diffusion coefficient (ADC) **D**. For simplicity of notation it is convenient to introduce the b factor which groups together the main parameters of the diffusion sequence (Le Bihan, 1991):

$$b = \gamma^2\delta^2(\Delta - \delta/3)\|\mathbf{g}\|^2 \quad (7)$$

Therefore the Stejskal–Tanner equation (5) is commonly written as:

$$E(\mathbf{q}) = \exp(-b\mathbf{D}). \quad (8)$$

where the signal notation was simplified to drop its dependance to the diffusion time Δ, *i.e.*, $E(\mathbf{q}) = E(\mathbf{q}, \Delta)$. The result of Eq. (8) is valid for diffusion in an unrestricted medium and is not restricted to the limit that $\Delta \gg \delta$ as it will be the case in the next section (Tanner and Stejskal, 1968).

1.6. Restricted diffusion

The Stejskal–Tanner equation (8) links the observed diffusion signal to the underlying diffusion coefficient, under the assumption that the diffusion is purely Gaussian. However, this Gaussian hypothesis is often violated when the diffusion is hindered, as is the case in the brain due to the presence of white matter fibers (Niendorf et al., 1996; Assaf and Cohen, 1998).

The propagator formalism enable one to characterize the diffusion without a prior Gaussian assumption (Kärger and Heink, 1983). Within the narrow pulse approximation (NPA) $\delta \rightarrow 0$, the diffusion gradient does not vary with time anymore $\int \mathbf{g}(t)\mathrm{d}t = \mathbf{g}(0) - \mathbf{g}(\Delta)$. This greatly simplifies the relationship between the spin phase difference and the position of the molecules during the gradient pulses (Tanner and Stejskal, 1968; Cory and Garroway, 1990; Callaghan, 1991):

$$E(\mathbf{q}) = \int_{\mathbf{p}_0 \in \Omega_x} \rho(\mathbf{p}_0) \int_{\mathbf{p}_t \in \Omega_x} P(\mathbf{p}_0|\mathbf{p}_\Delta)e^{i2\pi\mathbf{q}\cdot(\mathbf{p}_0 - \mathbf{p}_\Delta)}\mathrm{d}\mathbf{p}_t\mathrm{d}\mathbf{p}_0 \quad (9)$$

where $\rho(\mathbf{p}_0)$ is the spin density at initial time $t = 0$, which is assumed to be constant in the voxel and is zero elsewhere. The propagator $P(\mathbf{p}_0|\mathbf{p}_\Delta)$ gives the probability that a spin at its initial position $\mathbf{p}_0$ will have moved to position $\mathbf{p}_\Delta$ after a time interval Δ. We introduce the wave-vector **q** which is defined as

$$\mathbf{q} = \frac{\gamma}{2\pi}\int_0^t \mathbf{g}(t)\mathrm{d}t = \frac{\gamma}{2\pi}\mathbf{g}\delta \quad (10)$$

where $\mathbf{q} \in \Omega_q$. This simplification occurs in the NPA regime, and as a consequence **q** is not a function of time anymore and only depends on the encoding time δ. An excellent review of the relationship between the Stejskal-Tanner equation and the q-space formalism appears in (Basser, 2002).

Remark. An alternative convention $\mathbf{q} = \gamma\delta\mathbf{g}$ is sometimes found in the diffusion MRI literature, which comes from the convention of the Fourier transform without the exponential term 2π. In this paper, we use the convention described in Eq. (10).

In this formalism, the b factor defined in Eq. (7) can also be expressed as a function of the **q** wave vector:

$$b = (2\pi)^2(\Delta - \delta/3)q^2 \quad (11)$$

where q stands for the norm of the wave-vector, *i.e.*, $q = \|\mathbf{q}\|$. Let **p** be the net displacement vector $\mathbf{p} = \mathbf{p}_\Delta - \mathbf{p}_0$, then the diffusion Ensemble Average Propagator (EAP) $P(\mathbf{p})$ of a voxel is defined as

$$P(\mathbf{p}) = \int_{\mathbf{p}_0 \in \Omega_x} \rho(\mathbf{p}_0) P(\mathbf{p}_0 | \mathbf{p}_0 + \mathbf{p}) \mathrm{d}\mathbf{p}_0 \qquad (12)$$

Therefore, the diffusion signal $E(\mathbf{q})$ at the diffusion time Δ is linked to the EAP by the following relationship (Callaghan, 1991; Cory and Garroway, 1990; Stejskal, 1965):

$$E(\mathbf{q}) = \int_{\mathbf{p} \in \Omega_x} P(\mathbf{p}) \exp\left(i2\pi\mathbf{q}^{\mathrm{T}}\mathbf{p}\right) \mathrm{d}\mathbf{p} = \mathcal{F}_{3\mathrm{D}}^{-1}[P](\mathbf{q}) \qquad (13)$$

Eq. (13) is the inverse three-dimensional Fourier transform $\mathcal{F}_{3\mathrm{D}}^{-1}$ of the average propagator, with respect to the displacement vector $\mathbf{p} \in \Omega_p$ of water molecules inside a voxel at position $\mathbf{p}$. Similarly, the three-dimensional Fourier transform $\mathcal{F}_{3\mathrm{D}}$ of E relates to P:

$$P(\mathbf{p}) = \int_{\mathbf{q} \in \Omega_x} E(\mathbf{q}) \exp(-i2\pi\mathbf{q}^{\mathrm{T}}\mathbf{p}) \mathrm{d}\mathbf{q} = \mathcal{F}_{3\mathrm{D}}[E](\mathbf{p}) \qquad (14)$$

In other words, the diffusion signal E is acquired in the q-space which is the Fourier domain. The q-space formalism (or g-space (Stejskal, 1965)) was introduced by (Stejskal, 1965; Callaghan, 1991; Cory and Garroway, 1990).

The q-space formalism is able to describe in a common framework numerous estimation methods. In this case, the diffusion signal is related to the displacement of the molecules between $t = 0$ and $t = \Delta$ (cf. Fig. 4a). However, this formalism is based on several assumptions about the diffusion signal acquisition (Cory and Garroway, 1990; Callaghan, 1991):

1. It is assumed that the gradient time $\delta \approx 0$ is negligible so that there is no displacement of water molecules during that period. In practice, the gradient duration δ is not always negligible and the measured displacement is related to the mean position of the molecules between time intervals $t = [0, \delta]$ and $t = [\Delta, \delta]$ (cf. Fig. 4b);
2. It is assumed that that the gradient time δ is very short compared to the diffusion time Δ, so that the q wave-vector can be assumed to not be a function of time (cf. Eq. (10)).

In the present paper we assume that these assumptions are valid, since they are necessary for the definition of q-space. Several studies (Blees, 1994; Coy and Callaghan, 1994; Mitra and Halperin, 1995; Mair et al., 2002; Bar-Shir et al., 2008) have shown that when these assumptions do not hold, the Fourier relationship (Eq. (13) and (14)) is still valid, but that the interpretation of the signal should be somewhat different. Instead of the diffusion propagator formalism, a center of mass propagator formalism applies, due to a homothetic transformation of the signal features.
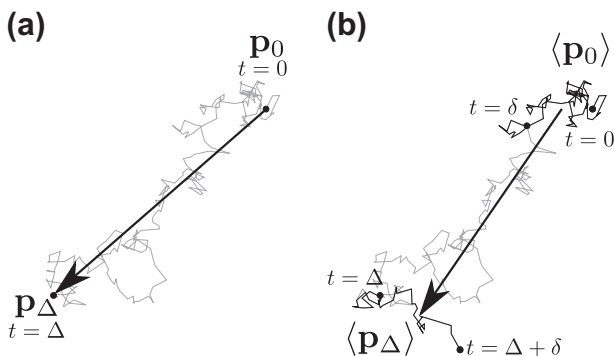

Fig. 4. Simulated random walk as measured by the PGSE sequence. (a) Ideal case ($\delta \approx 0$), (b) real case ($\delta \not\approx 0$). Adapted from (Hagmann, 2005).

Remark. The fundamental explicit relationship between the acquired image I and the diffusion propagator P is expressed by combining Eqs. (3) and (14):

$$P(\mathbf{x}, \mathbf{p}) = \mathcal{F}_{3\mathrm{D}}[E(\mathbf{x}, \mathbf{q})](\mathbf{x}, \mathbf{p}) = \mathcal{F}_{3\mathrm{D}}\left[\frac{\mathcal{F}_{2\mathrm{D}}[I](\mathbf{k}, z, \mathbf{q})}{\mathcal{F}_{2\mathrm{D}}[I](\mathbf{k}, z, 0)}\right](\mathbf{x}, \mathbf{p}) \qquad (15)$$

where $E(\mathbf{x}, \mathbf{q}) = S(\mathbf{x}, \mathbf{q})/S(\mathbf{x}, 0)$ which normalizes the signal so that variations of E along $\mathbf{q}$ can be attributed solely to diffusion.

1.7. Modeling the shape of the diffusion signal

Fig. 5 provides a qualitative sense of the expected diffusion profile in several typical situations in brain white matter. When no fibers are present the diffusion is typically equal in all directions, with a Gaussian distribution radially (Fig. 5a). When a single fibers bundle is present there is maximum diffusion along its direction (Fig. 5b). When two fibers bundles cross there is preferential diffusion in the direction of each (Fig. 5c). Finally, Fig. 5d illustrates a case where there is equal diffusion all directions, but that there is a variation in speed radially which indicates the apparent radius of the fibers bundle.

It is presently impractical to acquire a dense radial and angular sampling of the diffusion space due to the significant acquisition time this would imply. As a result, several advanced methods exist in the dMRI literature to sample and process the signal. The analysis of the diffusion signal is closely related to the sampling of the q-space as illustrated in Fig. 6. In the remainder of this article we review the state of the art methods, organized into three groups: low and high angular sampling methods (Sections 2 and 3), radial sampling methods (Section 4), and methods which combine radial and angular sampling (Section 5). We also include an appendix which reviews the mathematical concepts and tools required to understand and apply these methods.

The description of each method is organized according to the following themes:

1. *Local diffusion modeling*: We express the mathematical models used for the interpretation of the diffusion signal in the q-space, while clarifying the underlying assumptions;
2. *Model estimation from the data*: We describe the model estimation methods from the data acquired from the MRI scanner;
3. *Processing and extraction of diffusion features*: We present common post-processing techniques on the estimated model, to extract features of tissue microstructure;
4. *Advantages and limitations of the method*: We enumerate the main advantages (denoted with the + symbol) and limitations (denoted with a − symbol) of the method.

2. Low angular resolution diffusion imaging (DTI)

Diffusion anisotropy, as captured by diffusion nuclear magnetic resonance (NMR), was pointed out in early investigations involving controlled environments (Stejskal, 1965; Tanner and Stejskal, 1968; Tanner, 1978). This was followed by studies of the diffusion process within brain tissue using dMRI (Moseley et al., 1990). The acquired diffusion image depends on the orientation $\mathbf{u}$ of the diffusion wave-vector $\mathbf{q}$. Hence, the use of a tensor, a rotationally invariant object, is convenient to characterize the anisotropy of the apparent diffusion coefficient (ADC) of brain tissue, as suggested in several studies (Onsager, 1931a; Onsager, 1931b; De Groot and Mazur, 1962; Casimir, 1945; Stejskal, 1965). In this section, we describe the major method used for the characterization of this anisotropy of diffusion, in the case of low angular sampling of the q-space.
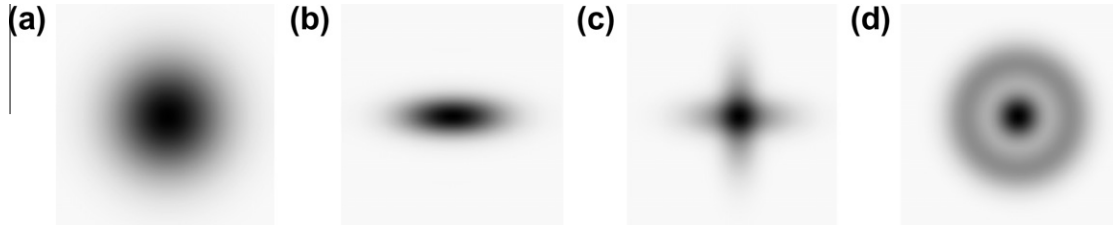
Fig. 5. Examples of local diffusion profiles E observed in the brain matter measured by dMRI. The data are represented here as volumetric images $64 \times 64 \times 64$, where the center of the q-space $\mathbf{q} = 0$ is the center of each image. (a) Free isotropic Gaussian diffusion. (b) Restricted diffusion due to the presence of a single fiber bundle. (c) Restricted diffusion in the presence of two fiber bundles in a crossing configuration. (d) Restricted diffusion which is isotropic in direction, but has a multi-Gaussian profile radially.
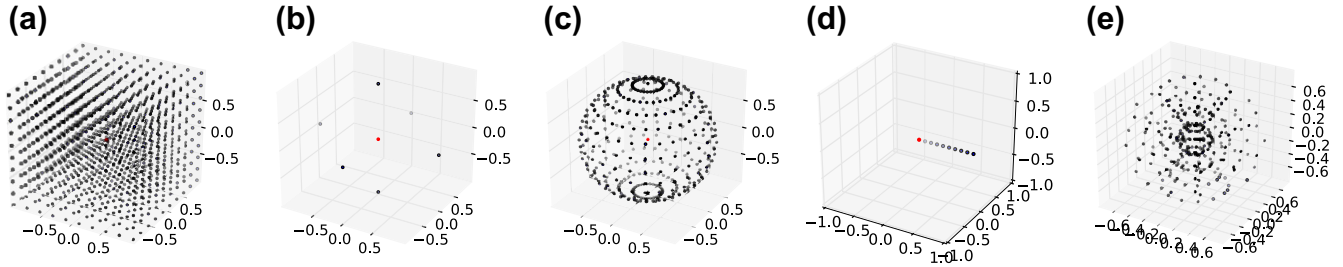

Fig. 6. The analysis of the diffusion signal is closely related to the sampling of the q-space. (a) Full sampling of the q-space is currently impractical *in vivo* due to the significant acquisition time it would imply. (b) Low angular resolution sampling used in DTI. (c) High angular resolution sampling (HARDI). (d) Radial only sampling used in diffusion NMR. (e) Sparse sampling which combines radial and angular measurements.

2.1. Local diffusion modeling

Whereas the scalar ADC measure is modeled with a zeroth-order tensor, DTI introduces the use of a second-order tensor $\mathbf{D}$, allowing a more accurate angular characterization of the diffusion process in the brain (Stejskal, 1965; Moseley et al., 1990; Filler et al., 1992; Basser and LeBihan, 1992). The mathematical framework which explicitly relates the diffusion tensor to the NMR signal was demonstrated by (Stejskal, 1965; Basser and LeBihan, 1992; Basser et al., 1994):

$$E(\mathbf{q}) = \exp(-4\pi^2\tau\mathbf{q}^T\mathbf{D}\mathbf{q}) \tag{16}$$

In this formalism, the average local diffusion process is described by a second-order tensor $\mathbf{D}$, whose coordinates in the q-space basis $\{\mathbf{u}_x, \mathbf{u}_y, \mathbf{u}_z\}$ are given by a 3×3 symmetric and positive-definite matrix:

$$\begin{pmatrix} D_{xx} & D_{xy} & D_{xz} \\ D_{xy} & D_{yy} & D_{yz} \\ D_{xz} & D_{yz} & D_{zz} \end{pmatrix} \tag{17}$$

In a environment such as water, the diffusion process $\mathbf{D}$ is assumed to be symmetric (*i.e.*, $\mathbf{D} = \mathbf{D}^T$) according to the principles of thermodynamics (Onsager, 1931a,b; De Groot and Mazur, 1962; Casimir, 1945; Stejskal, 1965; Basser et al., 1994).

2.2. Model estimation from the data

The apparent diffusion tensor profile $\mathbf{D}$ is expressed as a function of the wave-vector diffusion $\mathbf{q}$ defined in the q-space, so that the logarithm of Eq. (16) is:

$$D(\mathbf{q}) = \mathbf{q}^T\mathbf{D}\mathbf{q} = -\frac{\ln(E(\mathbf{q}))}{4\pi^2\tau} \tag{18}$$

Since the diffusion tensor $\mathbf{D}$ is symmetric, it is entirely defined by six components which can be grouped into a vector $\mathbf{D}$ (Basser et al., 1994):

$$\mathbf{D} = (D_{xx}, D_{xy}, D_{xz}, D_{yy}, D_{yz}, D_{zz})^T. \tag{19}$$

The construction of the sampling matrix of the q-space requires at least $n = 6$ acquisitions $\mathbf{q}_i$, $i \in [1, n]$ and one additional acquisition at $\mathbf{q} = 0$ for normalization (Stejskal, 1965; Basser et al., 1994; Tuch, 2002):

$$\mathbf{B} = 4\pi^2\tau \begin{pmatrix} q_1^x q_1^x & 2q_1^x q_1^y & 2q_1^x q_1^z & q_1^y q_1^y & 2q_1^y q_1^z & q_1^z q_1^z \\ q_2^x q_2^x & 2q_2^x q_2^y & 2q_2^x q_2^z & q_2^y q_2^y & 2q_2^y q_2^z & q_2^z q_2^z \\ \vdots & \vdots & \vdots & \vdots & \vdots & \vdots \\ q_n^x q_n^x & 2q_n^x q_n^y & 2q_n^x q_n^z & q_n^y q_n^y & 2q_n^y q_n^z & q_n^z q_n^z \end{pmatrix} \tag{20}$$

where the wave-vector is decomposed as $\mathbf{q}_i = q_i^x\mathbf{u}_x + q_i^y\mathbf{u}_y + q_i^z\mathbf{u}_z$. The sampling matrix defined in Eq. (20) is traditionally named the $\mathbf{B}$-matrix, in reference to its multiple b-factor entries $b_{ij} = 4\pi^2\tau q_i q_j$ (*cf.* Eq. (7)).

The logarithm of the data samples E_i, $i \in [1, n]$ are grouped in a vector $\mathbf{Y}$:

$$\mathbf{Y} = (-\ln(E_1), -\ldots, -\ln(E_n))^T. \tag{21}$$

Finally, Eq. (16) which links the model to the data, is expressed in the matrix form as:

$$\mathbf{Y} = \mathbf{B}\mathbf{D}. \tag{22}$$

In the case where there are exactly six acquisitions in different orientation of the q-space, the components of the diffusion tensor can be computed by the relationship $\mathbf{D} = \mathbf{B}^{-1}\mathbf{Y}$. However, such a process is very sensitive to the quality of the data and to perturbations due to acquisition noise. In practice, scanners are now able to acquire many mores images (typically up to $n = 60$ directions). From these n images, the tensor is estimated to be the one which minimizes a notion of error to the set of acquired data (Johansen-Berg and Behrens, 2009). There are several methods for the estimation and regularization of second-order tensor fields, including: weighted least squares (Basser et al., 1994), variational methods for the estimation of the image volume with positivity and regularity constraints (Chefd'hotel et al., 2002; Tschumperlé and Deriche, 2003a; Tschumperlé and Deriche, 2003b; Chefd'hotel

et al., 2004; Neji et al., 2007), estimation in a Riemannian space (Lenglet, 2006; Arsigny, 2006; Fillard et al., 2007) and the use of sparse representations (Bao et al., 2009; Luo et al., 2009).

2.3. Processing and extraction of diffusion features

DTI data is often visualized using a field of ellipsoids, where each voxel is represented by an isosurface of the diffusion tensor (Basser, 1995):

$$D(\mathbf{q}) = \mathbf{q}^T \mathbf{D} \mathbf{q} = \text{constant}. \tag{23}$$

In such a visualization, the eigenvectors of D give the principal axes of the ellipsoid, with their lengths scaled by the corresponding eigenvalues. Fig. 7 illustrates DTI data of an adult human brain data. In regions where there is a dominant local fiber direction the ellipsoids appear elongated to reflect it. The formalism of the second-order tensor contains rich information at a voxel scale. Nonetheless, this information is hard to grasp qualitatively in a volumetric image consisting of thousands of voxels. As a result, a wide variety of measures have been proposed to process and simplify the diffusion information reflected in the second-order tensor. In the following paragraphs, we classify these measures into two groups: scalar features and vectorial features.

Scalar features: There are various scalars features based on the second-order tensor which summarize the diffusion information at each voxel, enabling the depiction of qualitative aspects of diffusion on a larger scale (Pierpaoli and Basser, 1996; Papadakis et al., 1999). In contrast to the DWI and ADC methods, these scalar images are *not* dependent on the orientation of the patient with respect to the scanner, and they allow for straightforward inter-subject statistics to be computed. An example of such a scalar feature is the *trace* of the diffusion tensor, which is defined as the sum of the eigenvalues λ_i, computed in the basis of tensor eigenvectors (see Appendix A.2):

$$\text{Trace} = \sum_{i=1}^{3} \lambda_i \tag{24}$$

It is interesting to note that the trace/3 is the mean diffusion in a voxel. In a healthy patient this feature tends to lead to an image with relatively homogeneous intensity (Pierpaoli and Basser, 1996). This is useful in clinical applications since it is likely that any diffusion anomaly (such as due to an acute brain stroke) will lead to a local hyper- or hypo-intensity (Lythgoe et al., 1997).

A second popular feature is the fractional anisotropy (FA) which measures the normalized angular variance of diffusion within a voxel. It is defined as:

$$\text{FA} = \sqrt{\frac{3}{2}} \sqrt{\frac{\sum_{i=1}^{3} (\lambda_i - \langle \lambda \rangle)^2}{\sum_{i=1}^{3} \lambda_i^2}}, \tag{25}$$

where $\langle \lambda \rangle$ is the mean of the eigenvalues λ_i. At a voxel scale, the FA measures the alignment and the coherence of the underlying microstructure. Thus, voxels with compact fibers bundles have a high FA value (*e.g.*, in the corpus callosum), whereas voxels with non-aligned bundles tend to have a low FA value (*e.g.*, as in the case of crossing fibers). The FA is likely the most used scaler anisotropy index in the dMRI literature because it is relatively robust to noise in comparison to other features (Pierpaoli and Basser, 1996).

Several features related to the geometric shape of the second-order tensor have also been proposed in the literature (Basser, 1997; Westin et al., 1997). These are typically based on the ratio between the eigenvalues, sorted in a decreasing order, and can help distinguish between flat, elongated, and other profiles.

Vectorial features: It is often useful to extract vectorial features based on the DTI. A colour-coded orientation map of nerve fibers in the brain (Pajevic and Pierpaoli, 1999) is shown in Fig. 8a. The direction of nerve fibers is also shown using random texture smoothing (Tschumperlé and Deriche, 2005; Weickert and Hagen, 2006) (Fig. 8c) and using three-dimensional curves (Mori et al., 1999; Conturo, 1999; Jones et al., 1999b) (Fig. 8b) The process of tracking to reconstruct fiber bundles in DTI is generally based on a continuous tensor field which requires an interpolation of tensors (Fillard et al., 2007; Pennec et al., 2006; Arsigny, 2006).

2.4. Advantages and limitations of DTI

With improvements in the quality and speed of MRI scanners, the DTI model is somewhat limited. Indeed, it is not uncommon to have an angular acquisition resolution of the q-space of up to 128 directions (in comparison to the minimum seven directions required for a DTI reconstruction). When such angular precision is available, the model over-simplifies the diffusion process. Although the model is valid when there is a single dominant diffusion direction, such as in the corpus callosum (illustrated in Fig. 7), is it not accurate enough to characterize more complex diffusion profiles in the brain. These limits, those of modeling the diffusion coefficient by a second-order tensor, can be analyzed through a Taylor expansion of the diffusion signal E at $\mathbf{q} = 0$. The diffusion sig-
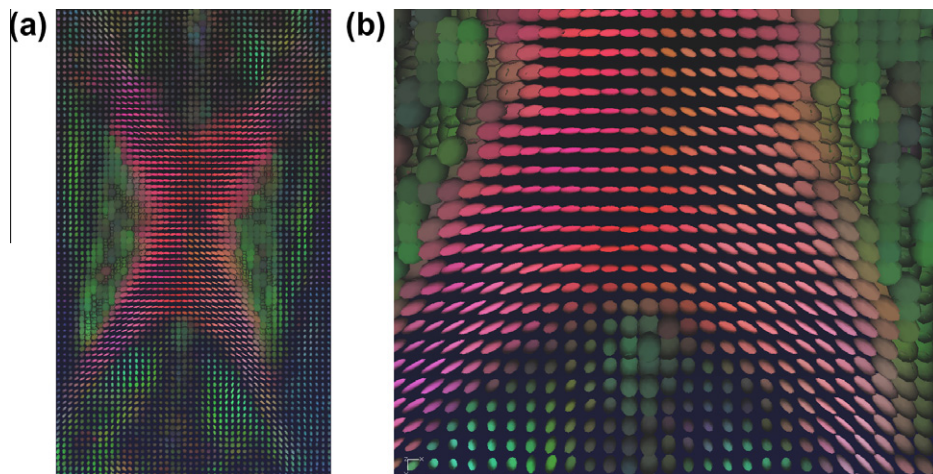
Fig. 7. DTI visualization using ellipsoids: from a global to a local view. (a) Visualization of the corpus callosum by a second-order tensor field. (b) Zoom on the bottom part of the corpus callosum. The privileged diffusion direction is the left–right axis, this is coherent since the corpus callosum links both brain hemispheres. The colours indicate the orientation of the principal eigenvector of each tensor (more details in Fig. 8).
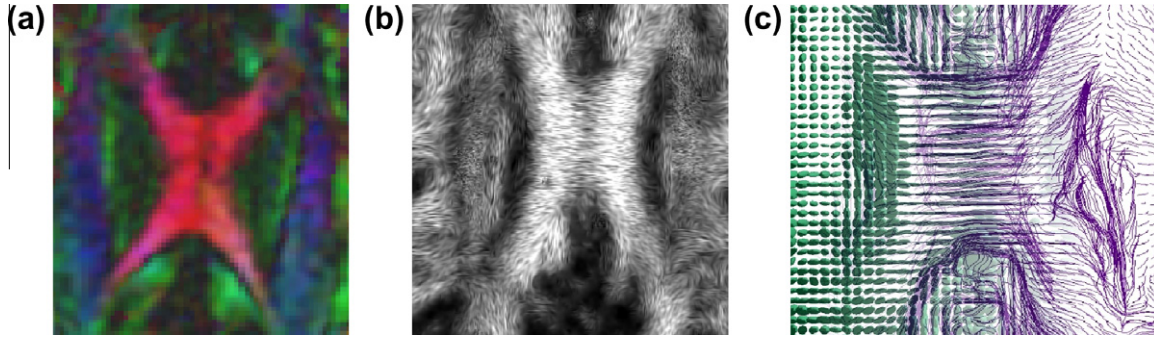
Fig. 8. Some vectorial features based on the principal eigenvector of the DTI (second-order tensor field). (a) The colour encodes the orientation of the vector and its norm is encoded by the brightness (red for left–right, blue for superior–anterior, green for anterior–posterior). (b) The curvature encodes the direction of each fiber and the brightness the smoothness strength. (c) Fiber tracking: A visualization of nerve fiber bundles as three-dimensional curves overlaid on the diffusion ellipsoids. These images are adapted from (Tschumperlé, 2002). (For interpretation of the references to colour in this figure legend, the reader is referred to the web version of this article.)

nal E is usually considered to be a symmetric function, so that the odd terms are equal to zero (Wedeen et al., 2005):

$$E(\mathbf{q}) = \exp\left(0 - \frac{(2\pi)^2}{2}\mathbf{q}^T\left(\langle\mathbf{pp}^T - \langle\mathbf{p}\rangle\langle\mathbf{p}\rangle^T\rangle\mathbf{q} + O\left(\|\mathbf{q}\|^4\right).\right)\right) \qquad (26)$$

Here $\langle\cdot\rangle$ is the expected value and $\langle\mathbf{pp}^T - \langle\mathbf{p}\rangle\langle\mathbf{p}\rangle^T\rangle$ is the covariance matrix of the diffusion propagator. Furthermore, the DTI model discards the terms with order higher than two, under the assumptions that: (i) the diffusion vector $\mathbf{q}$ is small ($\mathbf{q}^T\langle\mathbf{pp}^T\rangle\mathbf{q} \ll 1$ – typically this is true in brain tissues for $b < 1000$ s/mm^2) and (ii) the local diffusion is Gaussian (moments greater than two are zero). Under these assumptions Eq. (26) becomes:

$$E(\mathbf{q}) \approx \exp\left(-\frac{(2\pi)^2}{2}\mathbf{q}^T\langle\mathbf{pp}^T\rangle\mathbf{q}\right) = \exp\left(-4\pi^2\tau\mathbf{q}^T\mathbf{Dq}\right) \qquad (27)$$

where the coefficient $\langle\mathbf{pp}^T\rangle = 2\mathbf{D}\tau$ is given by the Einstein–Smoluchowski relationship (Einstein, 1905), yielding Eq. (16) of DTI.

Since the ADC is estimated with the hypothesis that the local diffusion follows a zero mean Gaussian function, the DTI method is expressed in the diffusion propagator P formalism as:

$$P(\mathbf{p}) = \sqrt{\frac{1}{(4\pi\tau)^3|\mathbf{D}|}}\exp\left(\frac{\mathbf{p}^T\mathbf{D}^{-1}\mathbf{p}}{4\tau}\right), \qquad (28)$$

where $P(\mathbf{p})$ is the probability that a water molecule inside a voxel travels a distance $\mathbf{p}$ during the diffusion time τ. Under these assumptions, the second-order tensor captures the diffusion covariance, which corresponds to the second-order moment of the diffusion propagator P.

The Gaussian hypothesis of the DTI model does not hold in the general case, *e.g.*, when crossing fibers are present (*cf.* Fig. 9b). In such situations the moments of order greater than two are not equal to zero. As a result, the representation of a crossing or any complex sub-voxel geometry is excessively simplified by DTI (Basser et al., 2000). Furthermore, fiber tracking results based solely on DTI can be unreliable in the presence of crossing fibers or other complex geometries (Campbell et al., 2005). We now summarize the advantages and limitations of DTI.

+ The time during which the patient must lie motionless is short, since the reconstruction requires a minimum of only seven acquisitions in q-space.
+ The second-order tensor appears to adequately model brain white matter regions where there is a single dominant direction of diffusion. The measured angle between the principal eigenvector and the ground-truth fiber orientation is approximately 13° (Lin et al., 2001).

+ The DTI model has became a standard method in the dMRI community and there is a vast literature on topics such as noise robustness (Basu et al., 2006), data regularization (Mangin et al., 2002; Tschumperlé and Deriche, 2005), sampling (Poupon, 1999; Jones et al., 1999a) and statistical studies (Chung et al., 2006).
− The modeling of the angular profile of the diffusion signal by a Gaussian function is often violated in the presence of complex geometries, such as fiber crossings, Y-configurations, bottlenecks, *etc.* (Savadjiev et al., 2008).
− Similarly, the modeling of the radial profile of the diffusion signal by a Gaussian function prevents one from retrieving more complete radial information, thus excluding features such as mean cell size, axon diameter, *etc* (Cory and Garroway, 1990; Callaghan et al., 1991; Kuchel et al., 1997; Assaf and Cohen, 1998; Regan and Kuchel, 2003).

3. High angular resolution diffusion imaging (HARDI)

High angular resolution diffusion imaging (HARDI) was proposed by Tuch et al. (1999) to enable a more precise angular characterization of the diffusion signal, while keeping the acquisition time compatible with clinical constraints. HARDI reduces the diffusion signal sampling to a single sphere of the q-space, and has initiated a significant interest in the scientific community as indicated by the numerous methods to tackle the recovery the geometry of crossing fibers, as illustrated in Fig. 9. In the following we describe the principal methods in the literature, which fall into two classes: parametric and non-parametric. The first class represents the diffusion signal as a sum of functions, each of which models a single fiber population. The second represents the diffusion signal as a mathematical series. A detailed quantitative comparison of several of these methods is available in (Jian and Vemuri, 2007; Ramirez-Manzanares et al., 2008).

3.1. Mixture models (parametric)

3.1.1. Local diffusion modeling
A variety of models in the literature assume that the diffusion signal can be decomposed as a weighted sum of generic diffusion models h_i:

$$E(\mathbf{q}) = \sum_{i=1}^{n} f_i h_i(\mathbf{q}) \quad \text{with} \quad \sum_{i}^{n} f_i = 1, \qquad (29)$$

where f_i stands for the weight of the ith bundle of nerve fibers and n is the total number of bundles. The mixture models of the literature can be expressed in the formalism of Eq. 29.
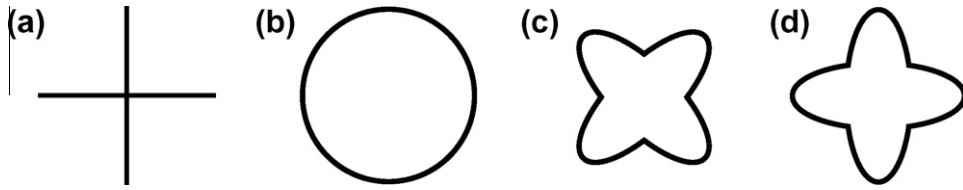
Fig. 9. HARDI sampling of the diffusion signal: a schematic overview of the modeling of an intravoxel crossing of bundles nerve fibers. (a) Two fiber bundles crossing at 90° inside a voxel generate a diffusion signal. (b) ADC modeling using a DTI reconstruction. (c) Generalization of the ADC modeling with HARDI sampling. The maxima of the angular profile do not match the underlying fiber bundle directions given in (a). (d) Angular feature estimation of the diffusion propagator with HARDI sampling. Adapted from (Descoteaux, 2008).

The multi-Gaussian (or multi-DTI) model proposed in (Tuch, 2002) generalizes DTI with the assumption that the diffusion signal is the sum of signals from several bundles of fibers, each modeled as a second-order tensor:

$$h_i(\mathbf{q}) = \exp(-4\pi^2\tau\mathbf{q}^\mathsf{T}\mathbf{D}_i\mathbf{q}). \qquad (30)$$

The parametric "Ball and Stick" (Behrens et al., 2003; Hosey et al., 2005) model describes the signal as a bi-Gaussian function ($n = 2$), where the two components h_{iso} and h_{aniso} correspond respectively to an isotropic ADC D and an anisotropic ADC $\mathbf{D}$:

$$h_{\mathrm{iso}}(\mathbf{q}) = \exp(-4\pi^2q^2\tau D) \qquad (31)$$

$$h_{\mathrm{aniso}}(\mathbf{q}) = \exp(-4\pi^2q^2\tau\mathbf{u}^\mathsf{T}\mathbf{D}\mathbf{u}) \qquad (32)$$

$$\mathrm{with} \quad \mathbf{D} = \mathbf{R}\lambda\mathbf{R}^\mathsf{T} = \mathbf{R}\begin{pmatrix} 1 & 0 & 0 \\ 0 & 0 & 0 \\ 0 & 0 & 0 \end{pmatrix}\mathbf{R}^\mathsf{T} \qquad (33)$$

with the rotation matrix $\mathbf{R}$ being that between the basis of the q-space and the basis defined by the eigenvectors of $\mathbf{D}$.

The CHARMED model (Assaf and Basser, 2005) proposes a parametrization with several components, one for the *hindered* diffusion modeled by a Gaussian function, and the others for the *restricted* diffusion modeled by diffusion inside a cylinder (Neuman, 1974):

$$E(\mathbf{q}) = f^{\mathrm{hind}}h^{\mathrm{hind}}(\mathbf{q}) + \sum_{i=2}^{n} f_i^{\mathrm{restr}}h_i^{\mathrm{restr}}(\mathbf{q})$$

$$h^{\mathrm{hind}}(\mathbf{q}) = \exp\left(-4\pi^2\tau((q^\perp)^2\lambda^\perp + (q^\parallel)^2\lambda^\parallel)\right)$$

$$h_i^{\mathrm{restr}}(\mathbf{q}) = \exp(-4\pi^2 K_i)$$

$$\mathrm{with} \quad K_i = \tau(q^\parallel)^2 D_i^\parallel + (q^\perp)^2\frac{7}{96}\left(2 - \frac{99}{112}\frac{R^2}{D_i^\perp\tau}\right)\frac{R^4}{D_i^\perp\tau}. \qquad (34)$$

The symbols f^{hind} and f^{restr} are the population fractions of the hindered and restricted terms, respectively; $q^\parallel$ and $q^\perp$ are the components of the q vector parallel and perpendicular to the fibers, respectively; $\lambda^\parallel$ and $\lambda^\perp$ are the eigenvalues of the diffusion tensor parallel and perpendicular to the axons (for a single coherent fiber bundle), respectively; $D^{parallel}$ and $D^\perp$ are the parallel and perpendicular diffusion coefficients within the cylinder; R is the cylinder radius; and τ is half of the echo time (Assaf and Basser, 2005).

3.1.2. Model estimation from the data

The estimation of these models is generally non-linear and is obtained by an iterative computation in which various priors (*e.g.*, positivity, tensor shape) on n, $\mathbf{D}_i$ and f_i are introduced to increase the numerical stability of the estimation (Alexander, 2005; Tuch et al., 2002; Chen et al., 2004; Behrens et al., 2003; Hosey et al., 2005). The noise and the number of samples influence the number of parameters and the estimation is carried out by a non-linear iterative numerical process such as gradient descent (Tuch et al., 2002), a Levenberg–Marquardt scheme (Maier et al.,

2004; Assaf and Basser, 2005), a Gauss–Newton scheme (Peled et al., 2006) or an unscented Kalman filter (Malcolm et al., 2010). The choice of the number of components n is either arbitrarily set (Tuch et al., 2002), or is chosen by a statistical criterion (Parker and Alexander, 2003; Tuch et al., 2002; Behrens et al., 2007).

3.1.3. Processing and extraction of diffusion features

The diffusion features which characterize the brain microarchitecture are directly obtained from the estimated model parameters. Thus, no additional postprocessing is required.

3.1.4. Advantages and limitations

+ The modeling of non-Gaussian angular profiles allows crossing fibers to be identified, which is a problematic case for DTI (Frank, 2002; Alexander et al., 2002; Özarslan et al., 2005).
+ The extraction of diffusion features does not require any postprocessing once the reconstructions have been obtained.
+ The number of samples in the q-space is modest, *e.g.*, typically 64 directions on a sphere suffice (Alexander, 2005).
– The estimation of the number of compartments requires additional processing (Behrens et al., 2007). Often the choice is somewhat arbitrary and under or over estimation of this parameter can be problematic.
– The estimation of the diffusion signal is based on an empirical hypothesis of the nature of diffusion within a healthy brain, in a context where the origin of the diffusion is still debated (Niendorf et al., 1996; Cohen and Assaf, 2002). Consequently, there are no guaranties that these models remain valid for the diffusion in other tissues, *e.g.*, in diseased brains, the heart, *etc.*
– The stability and the accuracy of the non-linear estimation step depends on the initial parameters, which vary with data (Aubert and Kornprobst, 2006). The estimation time is notably slower than the linear estimation of DTI, since it requires a iterative minimization process, *e.g.*, this takes approximately 2 h for a slice of 64×64 pixels according to (Assaf and Basser, 2005).
– As is the case with DTI (*cf.* Section 2), the modeling of the radial profile by a Gaussian function is inadequate since it excludes a wide range of features, including mean cell size, axon diameters, *etc.*

3.2. Spherical deconvolution (parametric)

3.2.1. Local diffusion modeling

The dMRI estimation by the spherical deconvolution (SD) was proposed by Anderson and Ding (2002), Tournier et al. (2004), and Jian and Vemuri (2007). Let $\mathbf{S}^2$ be the single sphere domain and $\mathbf{SO}(3)$ the rotation group in $\mathbb{R}^3$. The diffusion signal E is modeled by the convolution of a kernel $h \in L^2(\mathbf{S}^2)$ and a function $f \in L^2(\mathbf{SO}(3)$ which respectively represent the signal response for a single bundle of nerve fibers and the fiber orientation density function (fODF), ideally composed of n Dirac delta functions for n

bundles of fibers. The spherical deconvolution operator is expressed as (Healy et al., 1998):

$$E(\mathbf{q}) = (f * h(q))(\mathbf{u}) = \int_{\mathbf{R} \in \mathbf{SO}(3)} f(\mathbf{R}) h(\mathbf{q}, \mathbf{R}^\mathrm{T} \mathbf{u}) \mathrm{d}\mathbf{R}, \tag{35}$$

where $\mathbf{u} \in \mathbf{S}^2$ and the symbol $\mathbf{u}' = \mathbf{R}^\mathrm{T} \mathbf{u}$ stands for the rotation of the vector $\mathbf{u}$ by the matrix $\mathbf{R}$.

Jian et al. (2007) proposed a kernel based on the Wishart distribution, which is a multidimensional generalization of the χ^2 distribution (Wishart, 1928):

$$h(\mathbf{q}, \mathbf{u}') = \left(1 + 4\pi^2 q^2 \tau \mathbf{u}'^\mathrm{T} \mathbf{D} \mathbf{u}\right)^{-p} \tag{36}$$

with $\mathbf{D} \in P_n$ and P_n the set of the 3×3 positive-definite matrices, i.e., $\mathbf{u}'^\mathrm{T} \mathbf{D} \mathbf{u}' > 0$. The parameter $p \in \mathbb{R}$ should satisfy $p \geqslant n$ with n the degree of freedom and this generalizes other approaches in the literature (Jian et al., 2007). Indeed, when $p \to \infty$, the kernel h given by Eq. (36) is Gaussian as in several methods (Anderson and Ding, 2002; Tournier et al., 2004; Anderson, 2005; Seunarine and Alexander, 2006; Descoteaux et al., 2009a). When $p = 2$, the kernel h follows a Debye–Porod distribution proposed for the use of dMRI in (Sen et al., 1995).

The persistent angular structure (PAS-MRI) method, proposed by Jansons and Alexander (2003), is formally expressed as the function defined on the sphere of radius $k \in \mathbb{R}$ for which the inverse Fourier transform best fits the signal. This method can also be expressed as a deconvolution of the signal E with a kernel h expressed as (Alexander, 2005; Seunarine and Alexander, 2006):

$$h(\mathbf{q}, \mathbf{u}') = k^{-2} \cos\left(kq \mathbf{u}^\mathrm{T} \mathbf{u}'\right). \tag{37}$$

Some other studies propose the use of a kernel h which is dependent on the data, and which is computed by statistical estimation on the whole diffusion image (Tournier et al., 2004; Kaden et al., 2007).

3.2.2. Model estimation from the data

Let f be the orientation density function of fibers. Tournier et al. (2004) propose to express the spherical convolution expressed in Eq. 35) directly in the spherical harmonics domain, as a simple multiplication of the coefficients h_{lm} and f_{lm} (Healy et al., 1998):

$$E = (f * h) = \sum_{l=0}^{\infty} \sum_{m=-l}^{\infty} f_{lm} h_{lm}. \tag{38}$$

The matrix formulation of Eq. (38) is interesting as the f_{lm} can be computed by a simple matrix inversion.

The deconvolution operation is nonetheless unstable in the presence of noisy data, notably when h is an anisotropic kernel. Alexander (2005) and Tournier et al. (2008) suggest to regularize the function f with a Tikhonov filter. This frequency regularization can favourably be expressed in the spherical harmonic basis as a simple linear relationship which is easy to implement (Tournier et al., 2004; Descoteaux et al., 2006; Tournier et al., 2007).

3.2.3. Processing and extraction of diffusion features

The visualization of the distribution of fiber bundles f as a spherical function is useful to indicate the orientations of the sub-voxel fiber bundles (Seunarine and Alexander, 2006; Jansons and Alexander, 2003). This is often used as a preprocessing step in the context of using spherical deconvolution as an input to fiber tracking algorithms, as it reduces the angular estimation error (Descoteaux et al., 2009a; Savadjiev et al., 2008).

3.3. Advantages and limitations

+ When using a spherical harmonics basis the estimation is linear and is hence very fast.

+ In contrast to the mixture models, for which the number of compartments has to be determined a priori (cf. Section 3.1), this parameter can be obtained by simple thresholding of the reconstructed f distribution.

+ The non-Gaussian modeling of the angular profile enables the characterization of regions with crossing fibers.

+ The use of spherical harmonics for HARDI sampling generally requires approximately 60 samples on a sphere in the literature, which leads to a modest acquisition time (Tournier et al., 2004; Alexander, 2005).

– The choice of the deconvolution kernel h is empirical and is based on a priori assumptions about the data.

– As with DTI (cf. Section 2), the Gaussian modeling of the radial profile is inadequate and this excludes several features including apparent cell size, axon diameter, etc.

3.4. High angular ADC (non-parametric)

3.4.1. Local diffusion modeling

The first experiments to characterize multiple fiber bundle configurations were based on the generalization of the modeling of the apparent diffusion coefficient (ADC) from a low to a high angular resolution, without the Gaussian assumption imposed by DTI (Frank, 2002; Alexander et al., 2002; Tuch et al., 2002). Recall that the normalized diffusion signal E is modeled by the Stejskal–Tanner equation (Stejskal and Tanner, 1965):

$$E(\mathbf{q}) = \exp(-4\pi^2 \tau q^2 \mathbf{D}(\mathbf{u})). \tag{39}$$

In contrast to DTI, HARDI sampling allows high angular modeling of the ADC with functions of order higher than the second-order diffusion tensor used in DTI. Thus, Özarslan and Mareci (2003) and Descoteaux et al. (2006) propose to model the ADC by a higher order tensor (HOT):

$$D(\mathbf{u}) = \sum_{j=1}^{J_l} D_j \mu_j \prod_{p=1}^{l} \mathbf{u}_{j(p)}, \tag{40}$$

where the symbol $J_l = (l+1)(l+2)/2$ corresponds to the number of terms of a l-order tensor, $u_{j(p)}$ is the pth value of the jth tensor component D_j and μ_j is the multiplicity index (Özarslan and Mareci, 2003).

In parallel, several studies suggested the use of spherical harmonics (SH) for angular ADC estimation (Frank, 2002; Alexander et al., 2002; Zhan et al., 2003; Chen et al., 2004):

$$D(\mathbf{u}) = \sum_{j=0}^{J_l} D_j y_j(\mathbf{u}), \tag{41}$$

where $J_l = (l+1)(l+2)/2$ corresponds to the number of terms of an order l harmonic expansion (cf. Eq. (133)), the symbols y_j stands for the real and symmetric spherical harmonics, and D_j are the weighting coefficients.

Remark. There is a mathematical equivalence between spherical expansions which use the same order of spherical harmonics (Eq. (40)) and Cartesian tensors (Eq. 41) (Johnston, 1960; Özarslan and Mareci, 2003; Descoteaux et al., 2006).

3.4.2. Model estimation from the data

As with the DTI method detailed in Eq. (16), the high angular ADC coefficients D_j result from the dot product between the log-normalized diffusion signal E and the higher order tensors:

$$D_j = \int_{\mathbf{u} \in \mathbf{S}^2} -\frac{\ln(E)}{4\pi^2 \tau q^2} \mu_j \prod_{p=1}^{l} \mathbf{u}_{j(p)} \mathrm{d}\mathbf{u}. \tag{42}$$

Hence, the ADC is expressed in the spherical harmonics basis as:

$$D_j = \int_{\mathbf{u} \in \mathbf{S}^2} -\frac{\ln(E)}{4\pi^2 \tau q^2} y_j(\mathbf{u}) d\mathbf{u}. \tag{43}$$

In practice, the estimation of the parameters D_j of the HOT (Eq. (40)) and SH (Eq. (41)) models is solved by a linear least squares method because this is simple and fast to compute (Descoteaux et al., 2006), which can be seen as follows. Let us group the parameters into a vector $\mathbf{D}$:

$$\mathbf{D}^{\mathrm{T}} = (D_j)_{1 \leqslant j \leqslant J_l}. \tag{44}$$

The resulting system of linear equations can be written in the matrix form $\mathbf{Y} = \mathbf{MD}$, with $\mathbf{E}$ being the vector of samples given by Eq. (21) and $\mathbf{M}$ being the corresponding basis matrix, that is for the Jth-order tensors

$$\mathbf{M} = \left(\mu_j \prod_{p=1}^{l} \mathbf{u}_{1(p)}^{i} \right)_{1 \leqslant i \leqslant n_q, 1 \leqslant j \leqslant J_l}, \tag{45}$$

with n_q being the number of samples. For a spherical harmonics basis, the basis matrix is written as:

$$\mathbf{M} = (E_j(\mathbf{u}_i))_{1 \leqslant i \leqslant n_q, 1 \leqslant j \leqslant J_l}. \tag{46}$$

Finally, the vector $\mathbf{D}$ of model parameters is given by the pseudo-inverse of the matrix $\mathbf{M}$:

$$\mathbf{D} = (\mathbf{M}^{\mathrm{T}} \mathbf{M})^{-1} \mathbf{M}^{\mathrm{T}} \mathbf{E}. \tag{47}$$

Other studies have proposed the use of estimation techniques that are more robust to noise, which can have a significant effect in MR images (Gudbjartsson and Patz, 1995), notably the use of regularized least squares (Descoteaux et al., 2006) and of a variational estimation framework (Chen et al., 2004).

Whereas Eq. (47) enables a fast estimation, it does not ensure positivity of the vector $\mathbf{D}$. Hence, in (Barmpoutis, 2007), the estimation is expressed as a ternary quartic (a homogeneous polynomial of degree 4 with three variables), such that the Hilbert theorem (Hilbert, 1888) ensures positivity. Alternatively, Ghosh et al. (2008a) proposed the use of a Riemannian metric on the tensor space in order ensure positivity of the components of $\mathbf{D}$.

3.4.3. Processing and extraction of diffusion features

Scalar features: DTI has become a standard method for clinical use. The indices (*i.e.*, scalar features) based on higher order models therefore attempt to overcome the modeling limitations of DTI, particularly the detection of "crossing fibers" in brain tissue. In the following we enumerate three indices extracted from higher order models that are directly computed using the spherical harmonics or higher order tensor coefficients.

In the case of a spherical harmonics expansion of the diffusion signal, Frank (2002) demonstrates that the $\mathbf{D}$ coefficients can discriminate between the cases of isotropic diffusion (index F_0), anisotropic diffusion with a single intravoxel direction (index F_2) and anisotropic diffusion with several intravoxel directions (index F_{multi}):

$$F_0 = |D_0| \qquad F_2 = \sum_{j:l=2} |D_j| \qquad F_{\mathrm{multi}} = \sum_{j:l \geqslant 4} |D_j| \tag{48}$$

Some studies have proposed other scalar features based on a ratio between these three indices ($F_0, F_2, F_{\mathrm{multi}}$) to obtain more accurate results (Chen et al., 2004; Frank, 2002; Chen et al., 2005).

As mentioned in Section 2, fractional anisotropy (FA) is one of the most widely used scalar features of DTI, which motivates a generalization of this index to the higher order models. The generalized fractional anisotropy (GFA) is defined as the normalized variance of a spherical function, here the ADC, and is expressed for a discretization of the sphere in a set of n points by $\{\mathbf{u}_i\}_{1 \leqslant i \leqslant n}$ (Tuch, 2004):

$$\mathrm{GFA}(\mathbf{D}) = \frac{\mathrm{std}(\mathbf{D})}{\mathrm{rms}(\mathbf{D})} = \sqrt{\frac{n}{n-1} \frac{\sum_{i=1}^{n} (\mathbf{D}(\mathbf{k}_i) - \langle \mathbf{D} \rangle)^2}{\sum_{i=1}^{n} \mathbf{D}(\mathbf{k}_i)^2}}. \tag{49}$$

The GFA index can be directly computed using the spherical harmonics basis:

$$\mathrm{GFA}(\mathbf{D}) = \sqrt{1 - \frac{a_0^2}{\sum_{j=0}^{J} a_j^2}}. \tag{50}$$

Like the FA, the GFA is defined on the interval $[0, 1]$: a value of zero indicates a perfectly isotropic diffusion, while a value of one indicates a totally anisotropic diffusion.

Özarslan et al. (2005) proposed an alternative generalization of the FA, for a signal estimation based on higher order tensors. The obtained index, namely the generalized anisotropy (GA), is defined by the generalized trace $\mathrm{Tr}_{\mathrm{gen}}$ and variance $\mathrm{Var}_{\mathrm{gen}}$ operators:

$$\mathrm{Tr}_{\mathrm{gen}}(\mathbf{D}) = \frac{3}{4\pi} \int_{\mathbf{u} \in \mathbf{S}^2} D(\mathbf{u}) d\mathbf{u}$$

$$\mathrm{Var}_{\mathrm{gen}}(\mathbf{D}) = \frac{1}{3} \left(\mathrm{Tr}_{\mathrm{gen}} \left(\frac{\mathbf{D}^2}{\mathrm{Tr}_{\mathrm{gen}}(\mathbf{D})} \right) - \frac{1}{3} \right). \tag{51}$$

The GA is normalized in the interval $[0, 1)$ using an *ad hoc* data-dependent mapping (Özarslan et al., 2005):

$$\mathrm{GA} = 1 - \left(1 + (250 \mathrm{Var}_{\mathrm{gen}})^{f(\mathrm{Var}_{\mathrm{gen}})} \right)^{-1}$$

$$f(\mathrm{Var}_{\mathrm{gen}}) = 1 + (1 + 5000 \mathrm{Var}_{\mathrm{gen}})^{-1}. \tag{52}$$

Further details on this index are described in (Özarslan et al., 2005). Furthermore, a numerical comparison of selected scalar features of the high angular ADC is presented in (Descoteaux, 2008).

Vectorial features: The modeling of the ADC profile by higher order models leads to a more accurate characterization of intravoxel anisotropy than that provided by DTI. However, as illustrated in Fig. 9a and b, the maxima of the estimated ADC do not coincide with the directions of the underlying fiber bundles (von dem Hagen and Henkelman, 2002). Therefore the high angular resolution ADC cannot be used directly to extract meaningful vectorial features, and *a fortiori* for fiber tracking in brain white matter.

3.4.4. Advantages and limitations

+ The non-Gaussian modeling of the angular profile enables the characterization of brain regions with crossing fibers, which is a problematic case for the DTI (Frank, 2002; Alexander et al., 2002; Özarslan et al., 2005).
+ The use of parametric models for HARDI sampling generally requires approximately 60 samples on a sphere in the literature, which leads to a modest acquisition time (Tournier et al., 2004; Alexander, 2005). However this number of samples is variable and depends on the model order in use. The studies in the literature generally recommend an order equal to four or six, which is sufficient for the representation of crossing fibers (Frank, 2002; Alexander et al., 2002).
− The fact that maxima of ADC profile are not aligned with the underlying fiber directions prevents the direct extraction of accurate vectorial features, and *a fortiori* the use of fiber tracking algorithms in brain white matter (von dem Hagen and Henkelman, 2002).

– As is the case with DTI (*cf.* Section 2), the Gaussian modeling of the radial profile is inadequate and this excludes a wide variety of features including apparent cell size, axon diameter, *etc.*

3.5. Q-Ball Imaging (non-parametric)

3.5.1. Local diffusion modeling

Tuch (2004) introduced the technique of Q-Ball Imaging (QBI), which is primarily aimed at extracting the diffusion orientation density function (ODF). The ODF is a spherical feature of the ensemble average propagator, which we shall explain in greater detail after describing the signal modeling process.

In practice, a few samples from a HARDI sampling can be used to infer a continuous approximation process using a spherical basis to reconstruct the signal. In its original version (Tuch, 2004), the authors interpolate the diffusion signal with a spherical Radial Basis Function (sRBF) with a Gaussian kernel (Fasshauer and Schumaker, 1998). Later work (Anderson, 2005; Hess et al., 2006; Descoteaux et al., 2007) suggest the use of the spherical harmonics basis, which lowers the number of samples needed. In the latter basis, the normalized diffusion signal E, sampled by a HARDI acquisition on a sphere of radius q' in the q-space, is expressed as:

$$E(\mathbf{q}) = \sum_{l=0}^{L} \sum_{m=-l}^{l} a_{lm} y_l^m(\mathbf{u}) \delta(q - q'). \tag{53}$$

Several recent studies suggest the use of other spherical functions including: spherical ridgelets (Michailovich et al., 2008), spherical wavelets (Kezele et al., 2008; Khachaturian et al., 2007), or Watson, de von Mises and de la Vallé Poussin density functions (Rathi et al., 2009). The diffusion signal expansion in these latter bases requires fewer samples, but at the expense of a stronger prior assumption on the signal (concentration parameter which narrows the support of the functions).

3.5.2. Model estimation from the data

The coefficients a_{lm} of the signal E in the real spherical harmonic basis y_l^m of order l are the results of the following projection:

$$a_{lm} = \langle E, y_l^m \rangle = \int_{\mathbf{u} \in \mathbf{S}^2} E(\mathbf{u}) y_l^m(\mathbf{u}) d\mathbf{u}. \tag{54}$$

In practice, the $(l+1)(l+2)/2$ system of Eq. (54) is over-determined, and a least squares estimation method is used.

Poupon et al. (2008) tackles the issue of "real-time" QBI estimation, during the repetition time (TR) of the diffusion MRI acquisition sequence. At each new acquisition, the authors recursively estimate the incomplete set of images by a Kalman filter, for which Deriche et al. (2009) proposes an optimal resolution for Q-Ball Imaging.

Following the work of (Lustig et al., 2007), which uses *compressed sensing* to reduce the number of required samples in the k-space and the scanning time *a fortiori*, several studies recently propose the use of *compressed sensing* in the q-space (Landman et al., 2010; Michailovich et al., 2008; Michailovich and Rathi, 2010; Merlet and Deriche, 2010; Michailovich et al., 2010; Yin et al., 2008; Lee and Singh, 2010; Menzel et al., 2010). These estimation methods assume that the diffusion signal is sparse in the basis of modeling functions, *i.e.*, that most coefficients are equal to zero. Thus, the ideal estimation would minimize the number of non-zero coefficients (also known as the L_0 norm). However, solving this problem is not computationally feasible since it is non-deterministic polynomial-time hard (NP-hard). Estimation methods generally approximate this problem by minimizing the L_1 norm instead of the L_0 norm (*e.g.*, Candès et al., 2006; Donoho, 2002).

3.5.3. Processing and extraction of diffusion features

Scalar features: These are the same as the high angular ADC features which have been detailed in Section 3.4.

Spherical features: Eq. (55) links the diffusion orientation density function (ODF) that QBI aims to compute to the ensemble average propagator (EAP) formalism. The computation of the ODF overcomes the limits of ADC by correctly recovering the direction of crossing fibers, and thus is very often used as a preprocessing step for fiber tracking (Savadjiev et al., 2008; Lenglet et al., 2009; Anwander et al., 2007).

The *exact* diffusion ODF is defined as the radial projection of the diffusion EAP P on the unit sphere. Let $\mathbf{k} \in \mathbf{S}^2$ be a point on this sphere. The ODF is then expressed in the following general form (Canales-Rodríguez et al., 2010):

$$\mathrm{ODF}_\kappa(\mathbf{k}) = \frac{1}{Z_\kappa} \int_{p=0}^{\infty} P(p\mathbf{k}) p^\kappa dp, \tag{55}$$

where κ is the order of the radial projection and Z_n is a normalization constant such that $1/Z_\kappa \int_{\mathbf{k} \in \mathbf{S}^2} \mathrm{ODF}_\kappa(\mathbf{k}) = 1$. The classical ODF was introduced in the QBI method by Tuch (2004) as the zero-order radial projection, and will be denoted as ODF_0. Similarly, the second-order radial projection will be referred to as ODF_2. It has been used in other methods including the diffusion spectrum imaging method (DSI, Section 5.1), the diffusion orientation transform (DOT, Section 3.6) and the spherical polar Fourier expansion (SPF, Section 5.8).

Despite the fact that all the above ODF definitions capture angular information of the diffusion propagator, each one leads to slightly different results. Higher values of order κ will favour a longer displacement length.

The classical ODF_0 can be reformulated in the q-space as (Tuch, 2004):

$$\mathrm{ODF}_0(\mathbf{k}) = \frac{1}{Z_0} \int_{\mathbf{p} \in \mathbb{R}^3} P(\mathbf{p}) \delta(1 - \mathbf{r}^\mathrm{T} \mathbf{k}) d\mathbf{p} \tag{56}$$

$$= \int_{\mathbf{q} \in \mathbb{R}^3} E(\mathbf{q}) \delta(\mathbf{u}^\mathrm{T} \mathbf{k}) d\mathbf{q} \tag{57}$$

It is important to remark that the computation of the *exact* ODF_0 requires the value of the signal E in the whole q-space.

Since HARDI limits the samples to lie on a sphere of radius q', the QBI method cannot compute the exact ODF_0 but rather computes an *approximate* ODF_0. More precisely, the QBI method assumes that the diffusion signal is equal to zero outside the HARDI sampling sphere in the q-space, and retrieves an approximate ODF using the Fourier transform, which is equivalent in this particular setting to the Funk–Radon transform $\mathrm{FRT}_{q'}$ (Tuch, 2004):

$$\mathrm{FRT}_{q'}(\mathbf{k}) = \int_{\mathbf{u} \in \mathcal{S}^2} E(q'\mathbf{u}) \delta(\mathbf{u}^\mathrm{T} \mathbf{k}) d\mathbf{u}$$

$$= 2\pi q' \int_{\mathbf{p} \in \mathbb{R}^3} P(\mathbf{p}) J_0(2\pi q' p) \delta(1 - \mathbf{r}^\mathrm{T} \mathbf{k}) d\mathbf{p}, \tag{58}$$

with $\mathbf{k} \in \mathbf{S}^2$, and the symbol J_0 representing the zeroth-order Bessel function of the first kind (Abramowitz and Stegun, 1964):

$$J_0(z) = \sum_{n=0}^{\infty} (-1^n) \frac{z^{2n}}{4^n (n!)^2}. \tag{59}$$

Thus, the ODF given from the QBI Eq. (58) is an approximation of the exact ODF defined in Eq. (55), *i.e.*, $\mathrm{ODF} \approx \mathrm{FRT}_{q'}$.

Some studies propose the use of the spherical harmonics basis for the approximation of the diffusion signal (Anderson, 2005; Hess et al., 2006; Descoteaux et al., 2007), which interestingly simplifies the computation of the Funk-Radon transform as stated by the Funk–Hecke theorem (Andrews et al., 1999):

$$\text{FRT}_{q'}(\mathbf{k}) = \sum_{l=0}^{L} \sum_{m=-l}^{l} 2\pi P_l(0) a_{lm} y_l^m(\mathbf{k}), \qquad (60)$$

The Funk–Radon formulation of Eq. (60) is interesting since the computation involves only a matrix multiplication between the coefficient vectors (a_{lm}) and ($2\pi P_l(0)$).

Note that similar analytical Funk–Radon relationships to Eq. (60) were proposed for the spherical ridgelets functions (Michailo-vich et al., 2008) and the Watson, de von Mises and de la Vallé Poussin density functions (for approximate ODFs) (Rathi et al., 2009).

Extraction of fiber bundle directions: As in the context of fiber tracking in DTI, fiber bundles are usually reconstructed by following the direction of the principle eigenvector of the second-order tensor. When using the QBI method or other models capable of representing complex geometries, such as fiber crossings (illustrated in Fig. 9), the extraction of fiber bundle directions requires post processing.

The numerical lookup of the approximated ODF maxima, discretized on a grid of n points $\{\mathbf{k}_i\}_{i\leqslant n}$ distributed on the sphere for Eq. (60), requires significant computing time and the precision is dependent on the chosen number of points n. More recently, Bloy and Verma (2008) and Ghosh et al. (2008b) have proposed an analytical space reduction for the lookup of the maxima, from the higher order tensor coefficients. These maxima are expressed as fixed points of homogeneous polynomials. Ghosh et al. (2008b) have suggested that these methods can be also applied to spherical harmonics coefficients.

Once the ODF maxima are extracted for each voxel of the image, fiber tracking is carried out on the maxima field using three-dimensional curves (Savadjiev et al., 2006). Some studies have proposed a validation of the fiber tracking based on the QBI method, using a comparison with fiber tracking based on DTI (Campbell et al., 2005; Perrin et al., 2005).

3.5.4. Advantages and limitations

The original QBI method (Tuch, 2004) assumes that $P(\mathbf{p}) \approx P(\mathbf{p}) J_0(2\pi q'p)$. This approximation of the diffusion propagator leads to the corruption of the neighbourhood of direction $\mathbf{k}$ by the Bessel function J_0, which narrows in extent as the value of q' grows (Tuch, 2004). As a consequence, the obtained ODF_0 using the QBI method generally has a low angular contrast.

To solve this problem, the methods in the literature traditionally use an *ad hoc* postprocessing step, such as min–max normalization (Tuch, 2004) or a deconvolution with the Laplace–Beltrami operator (defined in Section A.3.2) (Descoteaux et al., 2009a). Aganj et al. (2009a) has suggested the use of a second-order ODF_2 in place of the zero-order ODF_0 which suppresses the need for such an *ad hoc* normalization (more details in Section 3.6). The advantages and limitations of QBI are summarized below.

+ The estimation of the angular diffusion profile is carried out without any biologic prior assumptions on the signal.
+ The linear estimation algorithm of the ODF in the spherical harmonics basis is very fast.
− As in the case of high angular ADC, described in Section 3.4, QBI requires approximately 60 samples on the sampling sphere.
− The method allows the extraction of only a single spherical feature.
− The estimation of the ODF_0 as proposed in the original QBI method (Tuch, 2004) is an approximation of the exact ODF. The corruption arises from the inappropriate Dirac modeling of the radial decay of the signal.

3.6. Diffusion orientation transform (DOT) (non-parametric)

3.6.1. Local diffusion modeling

Özarslan et al. (2006) proposed the diffusion orientation transform (DOT) method which computes the iso-radius of the diffusion propagator $P(p'\mathbf{k})$, with radius $p' \in \mathbb{R}^+$ and $\mathbf{k} \in \mathbf{S}^2$ a point on the unit sphere. This results in a spherical feature of the diffusion, however it is important to note that the iso-radius is different from the ODF feature proposed by the QBI method (detailed in the previous section). Nonetheless, several groups recently proposed to estimate an approximation of the ODF from the DOT modeling (Aganj et al., 2009a; Tristan-Vega et al., 2009; Canales-Rodríguez et al., 2010). We shall explain these features in greater details after describing the signal modeling process.

Assuming that the radial diffusion follows a Gaussian distribution, the normalized diffusion signal E is modeled by the Stejskal–Tanner equation (Stejskal and Tanner, 1965; Basser et al., 1992):

$$E(\mathbf{q}) = \exp(-4\pi^2 \tau q^2 \mathbf{D}(\mathbf{u})). \qquad (61)$$

However, Özarslan et al. (2006) propose to estimate the Fourier–Bessel transform I_l of the diffusion signal, which is the radial part of the Fourier transform decomposed as a plane wave expansion into the spherical harmonic basis and spherical Bessel of order l:

$$I_l(\mathbf{u}) = 4\pi \int_{q=0}^{\infty} E(\mathbf{q}) j_l(2\pi q p') q^2 \mathrm{d}q$$

$$\text{avec} j_l(z) = (-1)^l z^l \left(\frac{d}{zdz}\right)^l \frac{\sin z}{z} \qquad (62)$$

Here the symbols j_l stand for the spherical Bessel functions (Abramowitz and Stegun, 1964). The use of the Gaussian prior on the radial diffusion profile, as expressed in Eq. (61), enables one to solve Eq. (62) (Özarslan et al., 2006) analytically:

$$I_l(\mathbf{u}) = \frac{R_0^l \Gamma\left(\frac{l+3}{2}\right) 1F1\left(\frac{l+3}{2}; l+\frac{3}{2}; \frac{R_0^2}{\ln(E(\mathbf{u}))(\pi q)^{-2}}\right)}{2^{l+3} \pi^{3/2} \left(-\ln(E(\mathbf{u})) 4^{-1}(\pi q)^{-2}\right)^{(l+3)/2} \Gamma(l+3/2)}, \qquad (63)$$

with 1F1 the confluent hypergeometric function of the first kind (Abramowitz and Stegun, 1964):

$$1F1(a; b; x) = \sum_{k=0}^{\infty} \frac{(a)_k x^k}{(b)_k k!} \quad \text{with} \quad (a)_k = \frac{\Gamma(a+k)}{\Gamma(a)}, \qquad (64)$$

where $(a)_k$ stands for the Pochhammer symbol (Abramowitz and Stegun, 1964).

3.6.2. Model estimation from the data

The a_{lm} coefficient resulting from the expansion of Eq. (63) in the spherical harmonics basis y_l^m is expressed as:

$$a_{lm} = \langle I_l, y_l^m \rangle = \int_{\mathbf{u} \in \mathbf{S}^2} I_l(\mathbf{u}) y_l^m(\mathbf{u}) \mathrm{d}\mathbf{u}. \qquad (65)$$

The system of $(l+1)(l+2)/2$ equations given by Eq. (65) can be solved by a linear least square method.

Özarslan et al. (2006) suggest to speed up the estimation of Eq. (63) by using a table of precomputed values of the confluent hypergeometric 1F1 function defined in Eq. (64).

3.6.3. Processing and extraction of diffusion features

Scalar features: These are the same as the high angular ADC features (detailed in Section 3.4).

Spherical features: As mentioned in Section 3.4, the ADC formalism does not allow for the recovery of fiber bundle orientations.

On the other hand, the classical DOT method, as proposed by Özarslan et al. (2006), uses the diffusion EAP P in order to extract the *iso-radius*, defined as the surface $P(p'\mathbf{k})$ with $\mathbf{k} \in \mathbf{S}^2$ at a constant arbitrary distance $p' \in \mathbb{R}$. This feature can be expressed directly using the signal coefficients of Eq. (65) in the spherical harmonics basis y_l^m (Özarslan et al., 2006):

$$P(p'\mathbf{k}) = \sum_{l=0}^{L} \sum_{m=-l}^{l} a_{lm}(-i)^l y_l^m(\mathbf{k}) d\mathbf{p} \quad \text{with} \quad \mathbf{k} \in \mathbf{S}^2. \tag{66}$$

The estimation of Eq. (66) is fast and precise since it analytically links the EAP iso-radius to the diffusion signal coefficients in the spherical harmonics basis.

More recently, Aganj et al. (2009a), Tristan-Vega et al. (2009), and Canales-Rodríguez et al. (2010) have proposed to extend the DOT method to approximate the ODF. As mentioned for the QBI method (Section 3.5), the *exact* resolution of the $\{ODF_\kappa\}_{\kappa=\{0,2\}}$ requires a complete sampling of the q-space, which is not available for HARDI (spherical sampling). These methods use a single Gaussian prior on the radial diffusion profile E. We detail the more general case of a multi-Gaussian prior in Section 5.3.

3.6.4. Advantages and limitations

+ The estimation of the angular diffusion profile is carried out without any prior biological assumptions about the signal.
+ The linear estimation algorithm of the iso-radius in the spherical harmonics basis is fast.
− As with the case of the high angular ADC, described in Section 3.4, QBI requires approximately 60 samples on the sampling sphere.
− The precision of this method is limited by the mono-Gaussian assumption of the decay of radial diffusion, an assumption that does not always hold (Tanner and Stejskal, 1968; Callaghan et al., 1991; Niendorf et al., 1996; Assaf and Cohen, 1998).

4. Radial reconstruction in diffusion MRI

4.1. Introduction

Radial diffusion analysis by nuclear magnetic resonance (NMR), or q-space imaging (Callaghan, 1991; Cory and Garroway, 1990), favours a dense q-space sampling at the expense of the k-space sampling (see Section 1.3 for details on k-space). The dMRI data can be acquired over a large volume, such as an entire human brain. Diffusion NMR data, on the other hand, is acquired for a much smaller volume, such as a specimen enclosed in a test tube. The resulting image in diffusion NMR is composed of a *single* voxel.

Applications of diffusion NMR include the study of the microscopic geometry of mineralogical environments (sedimentary rock, ground, cement) and biological environments (proteins, lungs, the interstitial space of the skin). In theory, since the average diffusion length during typical measurement duration is close to a cell size, the restricted diffusion in these confined environments can accurately characterize properties of the underlying micro-architecture such as its porosity and tortuosity. Traditionally, this characterization is analyzed with a two-dimensional plot arising from sampling along a line in q-space (Stejskal and Tanner, 1965; Callaghan, 1991). The mathematical methods to analyze this plot are divided into three groups:

1. The methods of the first group take an analytical approach and propose a exact expression of the diffusion signal in q-space (*i.e.*, the Bloch–Torrey equation with the q-space formalism).

Nonetheless, these methods only characterize diffusion in simple models: infinite parallel planes, cylinders and spheres (Robertson, 1966; Tanner and Stejskal, 1968; Tanner, 1978; Brownstein and Tarr, 1979), or bi-compartment models (having a bi-Gaussian distribution) (Niendorf et al., 1996; Clark and Le Bihan, 2000; Le Bihan and van Zijl, 2002).

2. The methods of the second group extend to more complex diffusion situations, which do not have a known analytical solutions. The equations describing the behaviour of the diffusion signal are solved using numerical schemes, namely either: (i) resolution of the Bloch–Torrey equation with finite differences schemes (Wayne and Cotts, 1966; Putz et al., 1992; Zielinski and Sen, 2000) or (ii) by simulating a Brownian motion with the Monte-Carlo method (Mendelson, 1990; Hyslop and Lauterbur, 1991; Coy and Callaghan, 1994; Mitra and Halperin, 1995; Kuchel et al., 1997; Grebenkov et al., 2007).

3. Unlike the methods of the two previous groups which approximate simulations of the diffusion signal with biological models, the methods of the last group propose a functional analysis of the *in vivo* diffusion signal, *e.g.*, by using a discrete Fourier transform (Callaghan et al., 1991; Cory and Garroway, 1990), the Lévy distribution and Kohlrausch–Williams–Watts function (Köpf et al., 1996; Köpf et al., 1998), or cumulant expansion (Mitra and Sen, 1992; Stepisnik, 1981; Callaghan, 1991).

For a more detailed overview of these methods, we refer the reader to (Grebenkov, 2007).

Diffusion NMR studies have revealed that the radial profile of diffusion in brain structures is non-Gaussian (Tanner and Stejskal, 1968; Tanner, 1978; Cory and Garroway, 1990; Callaghan et al., 1991; Niendorf et al., 1996; Assaf and Cohen, 1998). A limitations of these studies, though, is that they typically assume the diffusion signal to be isotropic in its angular profile. Numerous studies have shown that this hypothesis is clearly not valid in the brain (*cf.* Section 2 and 3). In the following we describe two radial reconstruction methods in the literature, the diffusion kurtosis imaging (Jensen et al., 2005) and the simple harmonic oscillator (Özarslan et al., 2008).

4.2. Diffusion kurtosis imaging

4.2.1. Local diffusion modeling

Jensen et al. (2005) proposed the diffusion kurtosis imaging (DKI) method, which approximates the diffusion radial profile by a series of cumulants

$$\ln(E(q)) = -D_{app}(2\pi)^2 \tau q^2 + \frac{1}{6} D_{app}^2 K_{app}(2\pi)^4 \tau^2 q^4 + O(q^5) \tag{67}$$

where the symbols D_{app} and K_{app} refer to the apparent diffusion coefficient (ADC) and the Apparent Kurtosis Coefficient (AKC), respectively. The diffusion time is denoted $\tau = \Delta - \delta/3$. The expansion of Eq. (67) is a special case of the Generalized DTI (GDTI) method restricted to a fourth-order isotropic expansion Eq. (88) (see Section 5.4).

4.2.2. Model estimation from the data

Jensen et al. (2005) fit the diffusion signal on a voxel-by-voxel basis to the model described in the following formula, using the non-linear least square Levenberg–Marquardt method:

$$E(q) = \left(\frac{\eta^2}{E(0)^2} + \left(-D_{app}(2\pi)^2 \tau q^2 + \frac{1}{6} D_{app}^2 K_{app}(2\pi)^4 \tau^2 q^4 \right)^2 \right)^{1/2}, \tag{68}$$

where η is the background noise, which is estimated *a priori* as the mean signal intensity in air.
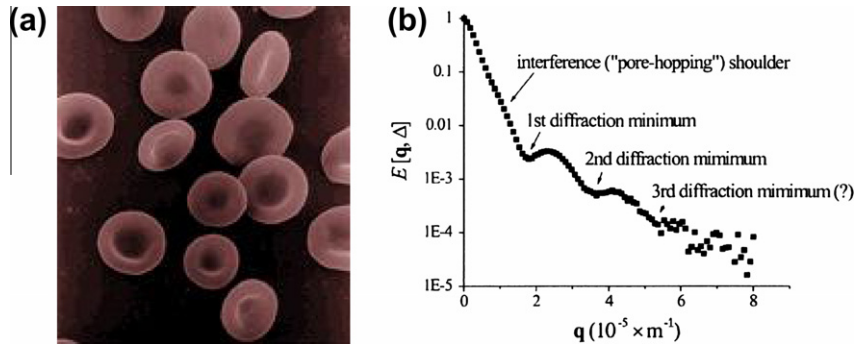
Fig. 10. A plot of the radial diffusion in an environment composed of red blood cells. It is important to note that the radial decay is not Gaussian, but a "diffusion–diffraction" pattern occurs (Cory and Garroway, 1990; Callaghan et al., 1991; Kuchel et al., 1997; Regan and Kuchel, 2003) where the position of the minima are related to cell size and extra-cellular average size. (a) A micrograph of red blood cells (adapted from Noguchi, Rodjers and Schechter, NIDDK, under free licence). (b) Signal intensity E as a function of q. Adapted from (Regan and Kuchel, 2003).

4.2.3. Processing and extraction of diffusion features

Scalar Features: In (Jensen et al., 2005), the authors compute an image of the apparent diffusion coefficient D_{app} and kurtosis K_{app}. The latter quantifies the degree to which the water diffusion is non-Gaussian. It is hypothesized that the kurtosis K_{app} can be altered by the space between the barriers and their porosity (also refereed to as "water exchange").

4.2.4. Advantages and limitations

+ The apparent diffusion kurtosis coefficient quantifies the degree to which the water diffusion is non-Gaussian, and thus reveals brain microstructure information hidden to DTI.
+ The number of samples in the q-space required for the estimation of the apparent diffusion kurtosis coefficient is small (minimum of six samples) (Jensen et al., 2005).
– The diffusion kurtosis imaging (DKI) method does not consider the angular profile of the diffusion signal, and essentially assumes that it is isotropic in direction. This assumption is clearly violated in the human brain (Moseley et al., 1990) and may lead to erroneous interpretation of the results.

4.3. Simple harmonic oscillator

4.3.1. Local diffusion modeling

Özarslan et al. (2008) propose an approximation of the diffusion radial profile in the basis of Φ_n functions, which is made up of Hermite polynomials H_n:

$$E(q) = \sum_{n=0}^{N-1} a_n \Phi_n(q, \alpha), \tag{69}$$

with $\quad \Phi_n(q, \alpha) = i^n (2^n n!)^{-1/2} \exp(-2\pi^2 q^2 \alpha^2) H_n(2\pi\alpha q). \tag{70}$

where $\alpha \in \mathbb{R}$ stands for the scale factor of the basis Φ_n functions.

4.3.2. Model estimation from the data

The coefficients a_n of the diffusion signal E in the basis of functions Φ_n are obtained with a dot product:

$$a_n = \langle E, \Phi_n \rangle = \int_{q=0}^{\infty} E(q) \Phi_n(q, \alpha) dq. \tag{71}$$

In practice, Özarslan et al. (2008) suggest that the coefficients a_n should be estimated using least squares techniques.

4.3.3. Processing and extraction of diffusion features

Scalar features: The m-order moments of the ensemble average propagator (EAP) P can be expressed as (Özarslan et al., 2008):

$$\langle p^m \rangle = \alpha^m \sum_{k=0,2,...}^{N-1} \frac{(k+m-1)!!}{k!} \sum_{l=0,2,...}^{N-k-1} (-1)^{l/2} \frac{\sqrt{2^{k-l}(k+l)!}}{(l/2)!} a_{k+l} \tag{72}$$

where k is even is m is even, otherwise k is odd.

Besides, the functions Φ_n are eigenfunctions of the Fourier transform, which allows the radial EAP to be directly expressed as a function of the signal coefficients a_n:

$$P(p) = \sum_{n=0}^{N-1} \frac{(-i)^n}{\sqrt{2\pi\alpha}} a_n \Phi_n(p, (2\pi\alpha)^{-1}). \tag{73}$$

4.3.4. Advantages and limitations

+ The radial diffusion profile is estimated without prior assumptions.
+ The diffusion EAP and its moments can be estimated using linear methods, which are very fast.
+ The Gauss–Hermite functions can approximate complex signals with relatively few samples of the q-space (33 according to (Özarslan et al., 2008)).
– This method does not consider the angular profile of the diffusion signal, and essentially assumes that it is isotropic in direction. This assumption is clearly violated in the human brain (Moseley et al., 1990).

## 5. Combining angular and radial reconstruction

5.1. Diffusion spectrum imaging (DSI)

5.1.1. Local diffusion modeling

Diffusion Spectrum Imaging (DSI) is based on the direct sampling of the diffusion signal E, leading to the EAP P using the q-space formalism (Wedeen et al., 2000; Wedeen et al., 2005; Lin et al., 2003; Tuch, 2002; Wu and Alexander, 2007; Wu et al., 2008; Assaf and Basser, 2005; Hagmann et al., 2004; Kuo et al., 2008). Since the diffusion signal sampling is carried out using practically the entire q-space *in three dimensions*, DSI does not require local diffusion modeling.

Nevertheless, in practice, the diffusion signal E samples are multiplied by an observation window to ensure a smooth decay of E at high values of the diffusion wave-vector norm $q = \|\mathbf{q}\|$. In (Wedeen et al., 2005), the authors use the Hann window, which is expressed as (Blackman and Tukey, 1959):

$$f(q) = \frac{1}{2}\left(1 + \cos\left(\frac{\pi q}{2a}\right)\right), \tag{74}$$
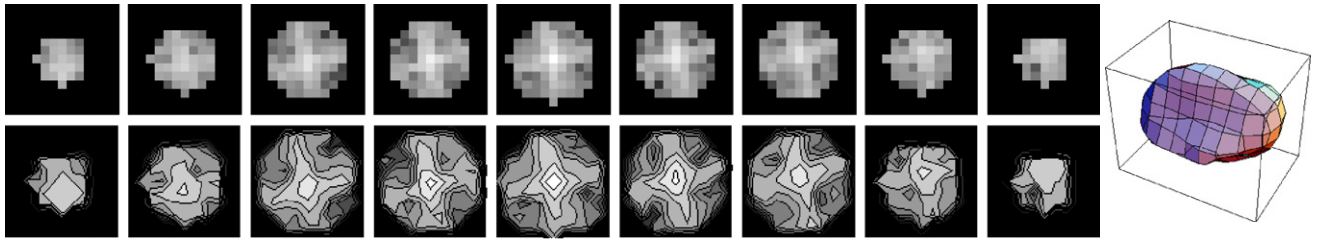
(a) First row: The raw diffusion data $E[\mathbf{q}]$ visualized as consecutive 2D planes of the q-space. Second row: The iso-contours in two dimensions. Right: An iso-surface in three dimensions.
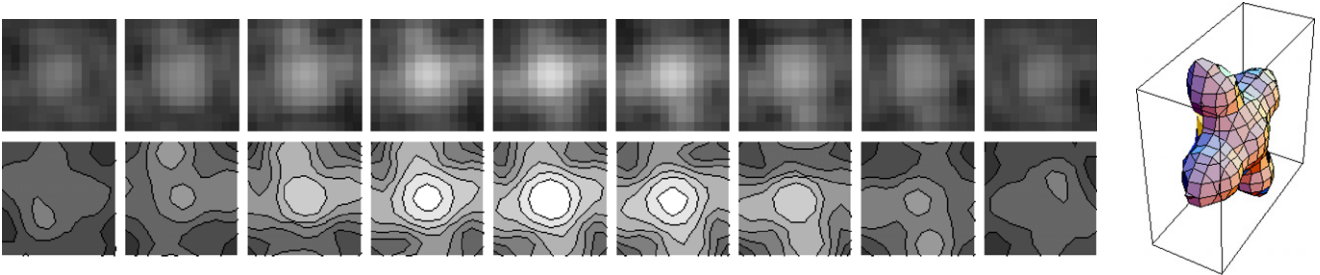
(b) First row: The diffusion propagator $P[\mathbf{p}]$ reconstructed with the Fourier transform of E and visualized as consecutive 2D planes of the q-space. Second row: Iso-contours in two dimensions. Right: An iso-surface in three dimensions.

Sequence	Image size	Voxel size (mm^3)	TE/TR (ms)	q-space samples
Single-shot, single slice	$64 \times 64 \times 1$	$3.6 \times 3.6 \times 3.6$	156/3000	512

Δ/δ (ms)	g_{max}(mT/m)	b_{max} (s/mm^2)	p_{min} (μm)	FOV (μm)	Time (min)
66/60	40	17 000	10	50	~ 25

(c) DSI acquisition sequence parameters (Wedeen et al., 2005).

Fig. 11. The DSI method for imaging in the coronal plane of a human brain. Note the non-Gaussian profile of the diffusion propagator P. Adapted from (Wedeen et al., 2005).

Sequence	Image size	Voxel size (mm^3)	TE/TR (ms)	q-space samples
DW-EPI	$64 \times 64 \times 10$	$3 \times 3 \times 3$	133/2700	169

Δ/δ (ms)	g_{max}(mT/m)	b_{max} (s/mm^2)	p_{min} (μm)	FOV (μm)	Time (min)
53/47	34	10 000	10.8	–	~ 17

(a) Parameters of the acquisition sequence of the CHARMED method, proposed by (Assaf and Basser, 2005).

Sequence	Image size	Voxel size (mm^3)	TE/TR (ms)	q-space samples
SS-SE-EPI	$128 \times 128 \times 30$	$2 \times 2 \times 3$	122/11700	102

Δ/δ (ms)	g_{max}(mT/m)	b_{max} (s/mm^2)	p_{min} (μm)	FOV (μm)	Time (min)
56/45	40	9375	13.2	65.8	~ 30

(b) Parameters of the acquisition sequence of the HYDI method, proposed by (Wu et al., 2008; Wu and Alexander, 2007).

Fig. 12. Parameters of two acquisition sequences, resulting in a sparse sampling of the q-space. (a) CHARMED (Assaf and Basser, 2005); (b) HYDI (Wu and Alexander, 2007; Wu et al., 2008).

where the symbol $a \in \mathbb{R}$ stands for the full width at half maximum of the window (FWHM) f.

5.1.2. Model estimation from the data

As mentioned above, DSI does not require modeling of the local diffusion so there is no model estimation step.

5.1.3. Processing and extraction of diffusion features

The diffusion propagator P is related to the diffusion signal E by the three-dimensional Fourier transform $\mathcal{F}_{3D}$ (Stejskal, 1965):

$$P(\mathbf{p}) = \int_{\mathbf{q} \in \Omega_q} E(\mathbf{q}) \exp\left(-i2\pi\mathbf{q}^T\mathbf{p}\right) d\mathbf{q}. \tag{75}$$

In practice, (Wedeen et al., 2005) use the discrete three-dimensional Fourier transform. Fig. 11 illustrates the DSI method for a slice of size $64 \times 64 \times 1$ taken from a human brain, acquired in 25 min with the parameters shown (see Fig. 12).

The majority of the features defined in previous sections can be computed *numerically* using the DSI method, *e.g.*, anisotropy indices, fiber bundle directions (Wedeen et al., 2008), apparent axon diameter (Weng et al., 2007), *etc*. Notably, using DSI one can compute the *exact* second-order ODF$_2$ as opposed to the *approximate*

ODF$_2$ of the DOT method (Section 3.6) or the zero-order ODF$_0$ of QBI (*cf.* Section 3.5).

5.1.4. Advantages and limitations

Given that the origin of the diffusion process is still debated, DSI offers the advantage that the diffusion propagator P is estimated without a model or prior assumptions about the angular or radial diffusion profiles.

Although DSI is one of the most accurate methods, two major issues make it unfit for clinical use:

1. DSI requires a very long acquisition time for the entire q-space to be sampled with sufficient density (Wedeen et al., 2008).
2. DSI requires very high magnetic gradients to explore the q-space, *e.g.*, $b = 17,000$ s/mm^2 according to (Wedeen et al., 2005).

In the literature, these two limitations restrict the use of DSI to animal *ex vivo* studies for which the acquisition time and the strength of the gradients are not limited. Alternatively, it is possible to limit the total acquisition time by reducing the k-space sampling, which is equivalent to scaling down the spatial resolution of the image. Typically, Wedeen et al. (2005) suggests the use of a voxel size equal to $3.6 \times 3.6 \times 3.6$ mm^3, versus $2 \times 2 \times 2$ mm^3 for current HARDI acquisitions (Tournier et al., 2008), leading to a total acquisition time of 25 min for an image size equal to $64 \times 64 \times 1$. We summarize the advantages and limitations of DSI below.

+ The radial and angular diffusion profiles are estimated without prior assumptions.
+ All the features of the local diffusion propagator can be computed.
– The hardware requirements to image the brain image lead to a very long acquisition time (typically several hours), which is incompatible with clinical applications.
– The use of the FFT algorithm imposes a rectangular sampling of the q-space, which is typically not suited to MRI scanners.

The remaining methods we describe utilize sparse or hybrid sampling of the q-space (Assaf and Basser, 2005; Wu and Alexander, 2007), in contrast to the dense sampling of the DSI method. In the literature, this sampling is traditionally carried out on several spheres of different radii, discretized in q-space. This sparse sampling enables both an angular *and* radial analysis of the diffusion signal, as opposed to the methods of the previous sections (Sections 2–4). Whereas we refer to "sparse sampling" in a broad sense, to our knowledge there is no mention of sampling other than multi-spherical sampling in the literature. We refer the reader to (Assemlal et al., 2009b) for a multi-sphere sampling model which unifies most of the existing sampling methods in the literature.

5.2. Hybrid diffusion imaging

5.2.1. Local diffusion modeling

Hybrid diffusion imaging (Wu et al., 2008) uses the raw diffusion data acquired in several spheres of the q-space, without any modeling or interpolation of the local diffusion signal.

5.2.2. Model estimation from the data

Since this method does not use any local diffusion model, the diffusion propagator is obtained with the Fast Fourier Transform (FFT). Since the FFT requires the data to lie on a rectangular grid Wu and Alexander (2007) and Wu et al. (2008) propose to adjust the diffusion signal to a $9 \times 9 \times 9$ Cartesian grid, using bilinear interpolation. On the other hand, Assaf and Basser (2005) interpo-

late the signal with a bi-Gaussian parametric model (CHARMED), as detailed in Section 3.1.

5.2.3. Processing and extraction of diffusion features

Wu et al. (2008) have also introduced an alternative approach, which does not require any adjustment of the diffusion signal to a Cartesian grid. The authors propose the computation of three features of the data samples, two of which are scalar and one of which is spherical.

Scalar features: The return to zero probability $P(0)$ is defined as (Wu et al., 2008):

$$P(0) = \int_{\mathbf{p} \in \mathbb{R}^3} P(\mathbf{p})\delta(\mathbf{p})\mathrm{d}\mathbf{p} = \int_{\mathbf{q} \in \mathbb{R}^3} E(\mathbf{q})\mathrm{d}\mathbf{q}. \tag{76}$$

The root mean square (RMS) is defined as (Wu et al., 2008):

$$\begin{aligned} \mathrm{RMS} = \langle \mathbf{p}^{\mathrm{T}}\mathbf{p} \rangle &= \int_{\mathbf{p} \in \mathbb{R}^3} P(\mathbf{p})\|\mathbf{p}\|^2 \mathrm{d}\mathbf{p} = \int_{p=0}^{\infty} P_s(p)p^2 \mathrm{d}p \\ &= \mathrm{Var}(P_m), \end{aligned} \tag{77}$$

with $P_m(p)$ the mean probability of P on the sphere of radius p. According to (Wu et al., 2008), the formulation of Eq. (77) in the q-space depends on the geometric mean (GM) of the signal E on the sphere of radius q:

$$rmRMS = \mathrm{Var}(\mathcal{F}_{1D}[\mathrm{GM}(E)])$$

$$\mathrm{GM}(E)(q) = \exp\left(\frac{1}{n}\sum_{i=1}^{n}\ln(E[q\mathbf{u}_i])\right) \tag{78}$$

where $\mathcal{F}_{1D}$ is the unidimensional Fourier transform and the family $\{q\mathbf{u}_i\}_{1 \leqslant i \leqslant n}$ constitutes the set of n sampling points of the sphere of radius q.

Spherical features: The exact ODF$_2$ is defined by Eq. (56).

Tridimensional features: Wu and Alexander (2007) and Assaf and Basser (2005) also compute the diffusion propagator P with the Fourier transform of E, first preprocessing the data with an interpolation step, as described above.

5.2.4. Advantages and limitations

The Fourier transform applied to the raw signal is quite sensitive to numerical inaccuracies since it is not based on a continuous approximation of the diffusion signal and the set of available samples is small.

+ The sparse sampling proposed in the literature results in similar acquisition times to HARDI (typically less than 30 min) and similar numbers of samples in the q-space (approximately 130) (Wu et al., 2008; Assaf and Basser, 2005).
+ Wu et al. (2008) have proposed the computation of three features of the diffusion propagator, which characterize properties of both the angular and the radial profiles of the signal.
– The numerical accuracy of the computations suffers from the *ad hoc* signal interpolation used to retrieve the diffusion propagator (Wu and Alexander, 2007; Assaf and Basser, 2005).

5.3. Generalized ODF

5.3.1. Local diffusion modeling

As mentioned in our discussion of the QBI and DOT methods in Sections 3.5 and 3.6, the estimation of the exact ODF$_\kappa$ of any order κ requires a full radial sampling. This is not the case for HARDI sampling and therefore only an *approximate* ODF$_\kappa$ can be computed.

Aganj et al. (2009b) model the diffusion signal E with N Gaussian functions α_k weighted by the coefficients λ_k:

$$E(\mathbf{q}) = \sum_{k=1}^{N} \lambda_k(\mathbf{u})\alpha_k(\mathbf{u})^{q^2}$$

$$\text{with} \quad \alpha_k(\mathbf{u})^{q^2} = \exp(q^2 \ln \alpha_k(\mathbf{u})), \tag{79}$$

where $N \leqslant (M-1)/2$, with M standing for the number of sampling spheres in the q-space. This multi-Gaussian approximation of the signal E allows one to analytically express the spherical Laplacian ∇_b^2 of the restriction of E to the plane orthogonal to the vector $\mathbf{k}$:

$$\int_{\mathbf{q}\perp\mathbf{k}} \frac{1}{q}\nabla_b^2 E(\mathbf{q})\mathrm{d}\mathbf{q} = -\frac{1}{2}\int_{\mathbf{u}\perp\mathbf{k}} \nabla_b^2 I(\mathbf{u})\mathrm{d}\mathbf{u}, \tag{80}$$

where the function $I(\mathbf{u})$ is defined as a function of coefficients λ_k and α_k (Aganj et al., 2009b):

$$I(\mathbf{u}) = \sum_{k=1}^{N} \lambda_k(\mathbf{u})\ln(-\ln\alpha_k(\mathbf{u})). \tag{81}$$

5.3.2. Model estimation from the data

Aganj et al. (2009b) propose the numerical estimation of the parameters λ_k and α_k with the confidence region algorithm (Branch et al., 2000) in the general case, i.e., for any number N of Gaussian functions. They also propose an analytical formulation for the special case of a mono or bi-Gaussian decay ($N = \{1, 2\}$).

Once the parameters λ_k and α_k are estimated, the function I defined in Eq. (81) is approximated in the basis of the spherical harmonics functions y_l^m:

$$a_{lm} = \langle I, y_l^m \rangle = \int_{\mathbf{u}\in\mathbf{S}^2} I(\mathbf{u})y_l^m(\mathbf{u})\mathrm{d}\mathbf{u} \tag{82}$$

In practice, (Aganj et al., 2009b) estimates Eq. (82) with the linear least squares method. Furthermore, the numerical computation of the l function as defined in Eq. (81) can be instable, requiring the introduction of some regularization (Aganj et al., 2009b).

5.3.3. Processing and extraction of diffusion features

Exact ODF: Aganj et al. (2009b) propose a second-order ODF$_2$ estimation based on an multi-Gaussian interpolation:

$$\text{ODF}_2(\mathbf{k}) = \int_{p=0}^{\infty} P(p\mathbf{k})p^2 dp \tag{83}$$

$$= -\frac{1}{8\pi^2}\int_{\mathbf{q}\perp\mathbf{k}} \nabla^2 E(\mathbf{q})\mathrm{d}\mathbf{q}$$

$$= -\frac{1}{8\pi^2}\int_{\mathbf{q}\perp\mathbf{k}} \frac{1}{q}\frac{\partial^2}{\partial q^2}(qE) + \frac{1}{q^2}\nabla^2 E(\mathbf{q})\mathrm{d}\mathbf{q}. \tag{84}$$

The radial Laplacian is simplified under the assumptions that the diffusion signal is equal to zero when $q \to \infty$, and that the signal derivative has a supremum. Combining Eq. (80) and (83) leads to the following relationship:

$$\text{ODF}_2(\mathbf{k}) = \frac{1}{4\pi} + \frac{1}{16\pi^2}\text{FRT}\left[\nabla_b^2 I(\mathbf{u})\right], \tag{85}$$

where the FRT acronym stands for the Funk-Radon transform operator defined in Eq. (58). Since the spherical harmonics are the eigenfunctions of the Laplace–Beltrami operator ∇_b^2 (cf. Section A.3.2), the combination of Eqs. (82) and (85) leads to the simplification of the ODF expressions (Aganj et al., 2009b):

$$\text{ODF}_2(\mathbf{k}) = \frac{1}{4\pi} + \frac{1}{8\pi}\sum_{l}^{L}\sum_{m=-l}^{l} P_l(0)a_{lm}.y_l^m(\mathbf{k}) \tag{86}$$

As with the case of the QBI method based on HARDI sampling (one sphere in the q-space), the relationship described by Eq. (86) is interesting because it linearly relates the generalized ODF to the coefficients a_{lm} of the function I.

Fusion ODF: Khachaturian et al. (2007) propose an alternative for the computation of the ODF$_0$ for the special case of two sampling spheres in the q-space. They estimate the ODF independently in each sphere in the spherical Gabor wavelets domain (Freeden et al., 1998), which results, respectively, in the set of coefficients a_i and b_i. They then merge these coefficients using the non-linear maxmod operator (Burt and Adelson, 1983; Li et al., 1995):

$$\text{maxmod}(a_i, b_i) = \begin{cases} a_i & \text{if } |a_i| \geqslant |b_i| \\ b_i & \text{otherwise} \end{cases} \tag{87}$$

5.3.4. Advantages and limitations

+ Aganj et al. (2009b) propose a linear and fast computation of the second-order ODF$_2$ in the spherical harmonics basis for a sparse sampling of the q-space.
+ The second-order ODF$_2$ does not require any post-processing to sharpen the ODF angular profile.
+ In contrast to the approximate ODF, for which the shape depends on the radius of the HARDI sphere sampling, the generalized ODF is theoretically independent of the sparse sampling, and this eases inter-subject comparison.
+ The number of q-space samples required for the ODF estimation is moderate (Wu et al., 2008; Assaf and Basser, 2005).
– The multi-Gaussian prior on the radial profile of the diffusion signal prevents the accurate approximation of a profile with a "diffusion–diffraction" pattern, as reported in (Callaghan et al., 1991; Cory and Garroway, 1990).
– The proposed method can extract only one feature of the diffusion propagator, namely the ODF.
– The fusion ODF is an *ad hoc* extension of the QBI method for multi-sphere sampling.

5.4. Generalized DTI

5.4.1. Local diffusion modeling

Liu et al. (2004) propose to extend the second-order tensor modeling of the diffusion signal by taking advantage of a sparse sampling instead of HARDI. This approach, called generalized diffusion tensor imaging (GDTI), differs from the HOT method presented in Section 3.4, for which the higher order tensors capture only the angular profile while the radial profile is assumed to be Gaussian. In the GDTI formalism, the coefficients of the fourth-order tensor or higher capture the difference with a purely Gaussian profile (captured by the second-order DTI). The diffusion signal E is expressed as:

$$E(\mathbf{q}) = \exp\left(\sum_{l=2}^{L}(i)^l(2\pi)^l\left(\varDelta - \frac{l-1}{l+1}\delta\right)D_{i_1,\dots,i_l}\mathbf{q}_{i_1}\mathbf{q}_{i_2}\dots\mathbf{q}_{i_l}\right). \tag{88}$$

As noted by Liu et al. (2004), the diffusion signal E can also be interpreted as a characteristic function, i.e., the Fourier transform of the water displacement PDF. Such a characteristic function is usually expressed by a cumulant-generating function $Q_{i_1,\dots,i_l}$ of order l:

$$E(\mathbf{q}) = \exp\left(\sum_{l=1}^{L}\frac{(-i2\pi)^l}{l!}Q_{i_1,\dots,i_l}\mathbf{q}_{i_1}\dots\mathbf{q}_{i_l}\right), \tag{89}$$

where the cumulants $Q_{i_1,\dots,i_l}$ of order l are the Taylor expansion coefficients of the characteristic function logarithm. These cumulants are proportional to the diffusion tensor of the same order $D_{i_1,\dots,i_l}$ defined in Eq. (88), so that

$$Q_{i_1,\dots,i_l} = (-1)^l l! D_{i_1,\dots,i_l}\left(\varDelta - \frac{l-1}{l+1}\delta\right). \tag{90}$$

We point out that for the special case of second-order tensors $L = 2$, as used in the DTI method (*cf.* Section 2), Eq. (90) simplifies to the well known Einstein–Smoluchowski equation (Einstein, 1905; Smoluchowski, 1916):

$$Q_{i_1,i_2} = \langle \mathbf{p}\mathbf{p}^T \rangle = 2D_{i_1,i_2}(\Delta - \delta/3). \tag{91}$$

5.4.2. Model estimation from the data

As for the higher order tensor used in HARDI sampling (*cf.* Section 3.4), (Liu et al., 2004) estimates the tensors $D_{i_1,\dots,i_l}$ of order l with a matrix formulation of the n_q system of equations Eq. (88), where n_q is the number of samples of the q-space. The basis matrix $\mathbf{M}$, for the n_q samples set located at $\{q^k\}_{1 \leqslant k \leqslant n_q}$ in the q-space is:

$$\mathbf{M} = \left((i)^l (2\pi)^l \left(\Delta - \frac{l-1}{l+1}\delta \right) \mathbf{q}_{i_1}^k \mathbf{q}_{i_2}^k \dots \mathbf{q}_{i_l}^k \right)_{1 \leqslant k \leqslant n_q, 1 \leqslant l \leqslant L}. \tag{92}$$

Liu et al. (2004) estimate the vector made of tensor components $D_{i_1,\dots,i_l}$ of order l with Singular Value Decomposition (SVD) (Stewart and Stewart, 1973). The cumulants $Q_{i_1,\dots,i_n}$ are then computed using Eq. (90).

5.4.3. Processing and extraction of diffusion features

Diffusion propagator: The estimated cumulants $Q_{i_1,\dots,i_n}$ are analytically related to the diffusion propagator by a Gram–Charlier A series (Kendall and Stuart, 1977; McCullagh, 1987; Liu et al., 2004):

$$P(\mathbf{p}) = \frac{1}{\sqrt{2\pi Q_{i_1,i_2}}} \exp\left(-\frac{\mathbf{p} \cdot \mathbf{p}}{2Q_{i_1,i_2}} \right) \left(1 + \sum_{l=3}^{L} \frac{Q_{i_1,\dots,i_l}}{l!} H_{i_1,\dots,i_l}(\mathbf{p}) \right), \tag{93}$$

where $H_{i_1,\dots,i_n}(\mathbf{p})$ stands for the Grad Hermite of order n defined as (Grad, 1949):

$$H_{i_1,\dots,i_l}(\mathbf{p}) = (-1)^l \exp\left(\frac{\mathbf{p}^2}{2} \right) \left(\frac{\partial}{\partial_{p_{i_1}}} \frac{\partial}{\partial_{p_{i_2}}} \cdots \frac{\partial}{\partial_{p_{i_l}}} \right) \exp\left(\frac{\mathbf{p}^2}{2} \right). \tag{94}$$

GDTI can also be interpreted as a multidimensional generalization of the simple harmonic oscillators presented in Section 4.3, which approximates the radial diffusion signal in one dimension in the basis of Hermite functions. This technique enables one to retrieve the complete diffusion propagator P without any prior assumptions on the diffusion signal E. From P, Liu et al. (2004) compute the iso-radius $P(p'\mathbf{k})$, $\mathbf{k} \in \mathbf{S}^2$ of radius p', the skewness and the kurtosis map.

5.4.4. Advantages and limitations

+ The diffusion signal is estimated without prior assumptions about its radial or angular profile.
+ An analytical relationship exists between the diffusion signal approximation in the tensor basis and the diffusion propagator.
+ The number of samples in the q-space required for the estimation of the diffusion signal is moderate (Wu et al., 2008; Assaf and Basser, 2005).
– The cumulant expansion of the diffusion signal is not guaranteed to converge for large values of the diffusion, and may in fact diverge in practice (Cramér, 1957; Kendall and Stuart, 1977; Frøhlich et al., 2006).

5.5. Diffusion propagator imaging (DPI)

5.5.1. Local diffusion modeling

The spherical harmonics functions, which are often used by the methods based on HARDI sampling, are the solution of the angular part of the Laplace equation, expressed in spherical coordinates (see Section A.3). The solution of the full Laplace equation (*i.e.*, with both angular and radial parts) results in the solid harmonics.

Descoteaux et al. (2009b) proposed diffusion propagator imaging (DPI), which approximates the diffusion signal E in the solid harmonics basis:

$$E(\mathbf{q}) = \sum_{l=0}^{\infty} \sum_{m=-l}^{l} \left[\frac{c_{lm}}{q^{l+1}} + d_{lm}q^l \right] y_l^m(\mathbf{u}) \tag{95}$$

5.5.2. Model estimation from the data

The signal approximation in the solid harmonics basis defined in Eq. (95) requires the computation of the coefficients c_{lm} and d_{lm}:

$$c_{lm} = \int_{\mathbf{q} \in \mathbb{R}^3} E(\mathbf{q}) \frac{y_l^m(\mathbf{u})}{q^{l+1}} d\mathbf{q} \quad \text{and} \quad d_{lm} = \int_{\mathbf{q} \in \mathbb{R}^3} E(\mathbf{q}) q^l y_l^m(\mathbf{u}) d\mathbf{q}. \tag{96}$$

For a set of n_q samples in the q-space, the computation of the coefficients c_{lm} and d_{lm} leads to a system of n_q linear equations, which can be solved using linear weighted least squares methods (Descoteaux et al., 2009b).

5.5.3. Processing and extraction of diffusion features

Diffusion propagator: Once the diffusion signal is estimated in the solid harmonics basis, resulting in the coefficients c_{lm} and d_{lm}, it is possible to analytically compute, in the same basis, the diffusion propagator P for any arbitrary value of water displacement p' (iso-radius) (Descoteaux et al., 2009b):

$$P(\mathbf{p}) = 2\sum_{l=0}^{\infty} \sum_{m=-l}^{l} \frac{(-1)^{l/2} 2\pi^{l-1} p^{l-2}}{(2l-1)!!} c_{lm} y_l^m(\mathbf{p}). \tag{97}$$

As mentioned in (Descoteaux et al., 2009b), the expression of P in Eq. (97) does not depend on the coefficients d_{lm}, but these are still required for the signal estimation in the solid harmonics basis. Furthermore, the radial functions of Eq. (95) $1/q^{l+1}$ and q^l, do not seem to be well adapted to the multi-Gaussian decay empirical observations of the signal.

5.5.4. Advantages and limitations

+ The diffusion signal is estimated without prior assumptions about its radial or angular profile.
+ An analytical relationship exists between the diffusion signal approximation in the solid harmonics basis and the diffusion propagator.
+ The number of samples in the q-space required for the estimation of the diffusion signal is moderate (Wu et al., 2008; Assaf and Basser, 2005).
– It is unclear how the radial diffusion basis functions is adapted to the multi-Gaussian decay of the signal reported by empirical observations (Niendorf et al., 1996) or to the "diffusion–diffraction" pattern (Callaghan et al., 1991; Cory and Garroway, 1990).

5.6. Generalized DOT

5.6.1. Local diffusion modeling

Özarslan et al. (2006) propose an extension of the DOT method for the case of multi-spherical sampling of the q-space, and generalize the original method to the multi-Gaussian case. The modeling of the diffusion signal E by n Gaussian functions is expressed as:

$$E(\mathbf{q}) = \sum_{i=1}^{n} f_i(\mathbf{u}) \exp\left(-4\pi^2 q^2 \tau D_i(\mathbf{u}) \right), \tag{98}$$

where f_i stands for the weight of the ith Gaussian function while the sum satisfies $\sum_{i=1}^{n} f_i(\mathbf{u}) = 1$.

5.6.2. Model estimation from the data

The generalized DOT requires an estimation of the parameters f_i and D_i, but the authors of (Özarslan et al., 2006) do not provide details of the method they use. It seems conceivable to use the non-linear least squares Levenberg–Marquardt technique (Marquardt, 1963).

Once the parameters f_i and D_i are estimated, the computation of the original function I_l of the mono-Gaussian case (cf. Eq. (65)) is generalized to the multi-Gaussian case:

$$I_l(\mathbf{u}) = \sum_{i=1}^{n} f_i(\mathbf{u}) I_{l_i}(\mathbf{u}) = \sum_{i=1}^{n} f_i(\mathbf{u}) \left[4\pi \int_{q=0}^{\infty} E_i(\mathbf{q}) j_l(2\pi q p') q^2 dq \right]. \quad (99)$$

The function I_l is then approximated in the spherical harmonics basis, resulting in the set of coefficients $\{a_{lm}\}_{0 \leqslant l \leqslant L}$, which is similarly to the original DOT method (see Section 3.6 for further details):

$$a_{lm} = \langle I_l, y_l^m \rangle = \int_{\mathbf{u} \in \mathbf{S}^2} I_l(\mathbf{u}) y_l^m(\mathbf{u}).d\mathbf{u} \quad (100)$$

5.6.3. Processing and extraction of diffusion features

The iso-radius spherical feature is extracted directly from the coefficients a_{lm} of Eq. (100), as in the case of the original DOT method presented in Section 3.6.

5.6.4. Advantages and limitations

+ The diffusion signal is estimated without prior assumptions about its angular profile.
+ An analytical relationship exists between the diffusion signal model and the diffusion propagator.
+ The number of samples in the q-space required for the estimation of the diffusion signal is moderate (Wu et al., 2008; Assaf and Basser, 2005).
− The multi-Gaussian prior on the radial diffusion prevents the accurate approximation of the observed "diffusion–diffraction" pattern (Callaghan et al., 1991; Cory and Garroway, 1990). Therefore it is not clear that this relatively constrained multi-Gaussian model results in accurate diffusion features.
− The proposed method can extract analytically only spherical features of the diffusion propagator, namely, the iso-radius and the ODF.
− The non-linear pre-estimation of the parameters f_i and D_i may causes stability and accuracy issues since they depend on the initial values, which vary with data (Aubert and Kornprobst, 2006).

5.7. Tomographic reconstruction

5.7.1. Local diffusion modeling

Pickalov and Basser (2006) propose to consider the Fourier transform which relates the diffusion signal E to its propagator P by the projection-slice theorem:

$$E(\mathbf{q}) = \int_{\mathbf{p} \in \mathbb{R}^3} P(\mathbf{p}) \exp\left(-i2\pi \mathbf{q}^T \mathbf{p}\right) d\mathbf{p} \quad (101)$$

$$= \int_{\mathbf{p} \| \mathbf{q}} \left(\int_{\mathbf{p}' \perp \mathbf{q}} P(\mathbf{p}') \exp\left(-i2\pi \mathbf{q}^T \mathbf{p}'\right) d\mathbf{p}' \right)$$
$$\exp\left(-i2\pi \mathbf{q}^T \mathbf{p}\right) d\mathbf{p}. \quad (102)$$

One recognizes the Radon transform of the marginal density $p_\mathbf{q}$ of the propagator P (Radon, 1917):

$$E(\mathbf{p}) = \int_{\mathbf{p} \| \mathbf{q}} p_\mathbf{q}(\mathbf{p}) \exp\left(-i2\pi \mathbf{q}^T \mathbf{p}\right) d\mathbf{p}. \quad (103)$$

The sampling of the diffusion signal along radial lines of the q-space enables one to compute the diffusion propagator P using the inverse Radon transform of $p_\mathbf{q}$, which is explicitly expressed as:

$$p_\mathbf{q}(\mathbf{p}) = \int_{\mathbf{q} \| \mathbf{p}} E(\mathbf{q}) \exp\left(i2\pi \mathbf{q}^T \mathbf{p}\right) d\mathbf{q}. \quad (104)$$

5.7.2. Model estimation from the data

The inversion of the Radon transform as described in Eq. (104) is not numerically usable due to instability issues. This is a problem that is common to many fields beyond dMRI (Deans, 1983). Therefore, numerous methods for a stable inversion of the Radon transform have been devised and Pickalov and Basser (2006) propose to use the iterative algorithm of Gerchberg and Papoulis (Defrise and De Mol, 1983; Veretennikov et al., 1992).

To ensure the numerical stability of the reconstruction process, the authors introduce regularity on the signal E and on the diffusion propagator P, based on Tikhonov regularization.

5.7.3. Processing and extraction of diffusion features

The full diffusion propagator P is directly estimated by the inverse Fourier transform. Nonetheless, to our knowledge there is no method based on this formalism for the extraction of features of P.

5.7.4. Advantages and limitations

+ The diffusion signal is estimated without prior assumptions about its radial or angular profile.
+ A large literature exists on the stable inversion of the Radon transform.
− The number of q-space samples required to estimate the propagator estimation is relatively high (496 according to (Pickalov and Basser, 2006)).
− Tikhonov regularization of the diffusion signal might result in overly smooth reconstruction.

5.8. Spherical polar Fourier expansion (SPF)

5.8.1. Local diffusion modeling

To take advantage of whatever the acquisition protocol may be (generally one or several spheres in the q-space), Assemlal et al. (2009a) define an orthonormal basis from a combination of angular and radial elementary functions expressed in spherical coordinates. The authors then expand the MR signal attenuation E as the following series in the orthonormal basis Spherical Polar Fourier (SPF):

$$E(\mathbf{q}) = \sum_{n=0}^{\infty} \sum_{l=0}^{\infty} \sum_{m=-l}^{l} \Psi_{nlm}(\mathbf{q}) \quad \text{with} \quad \Psi_{nlm}(\mathbf{q}) = R_n(q) y_l^m(\mathbf{u}), \quad (105)$$

so that $n \in \mathbb{N}$ is the radial index, and $l \in \mathbb{N}$, $m \in \mathbb{Z}, -l \leqslant m \leqslant l$ are the angular indexes. The symbols $a_{n,l,m}$ are the series coefficients, y_l^m are the real spherical harmonics (SH), and R_n is an orthonormal radial basis function made of Gaussian–Laguerre (GL) functions.

The radial component of the MR signal is reconstructed by the functions R_n. Since the number of radial samples is highly limited, the radial signal is expected to be sparse in R_n in the basis, i.e., to capture the radial attenuation of E with a few orders n. Assemlal et al. (2009a) propose a general estimation method for the radial part of the signal attenuation E using a normalized basis of generalized Gaussian–Laguerre polynomials R_n:
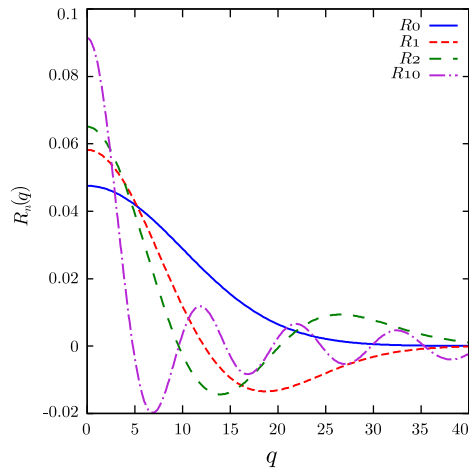
Fig. 13. The first few basis functions of the radial orthonormal basis R_n, with scaling factor $\zeta = 100$. Low order n functions exhibit Gaussian attenuation behaviour whereas higher order n are helpful to capture oscillating components of the MR signal.

$$R_n(q) = \kappa_n(\zeta) \exp\left(-\frac{q^2}{2\zeta}\right) L_n^{1/2}\left(\frac{q^2}{\zeta}\right), \tag{106}$$

$$\kappa_n(\zeta) = \left[\frac{2}{\zeta^{3/2}} \frac{n!}{\Gamma(n+3/2)}\right]^{1/2} \tag{107}$$

$$L_n^{(\alpha)}(x) = ((\alpha+1)_n/n!)1F1(-n, \alpha+1, x), \tag{108}$$

where ζ denotes the scale factor and $L_n^{(\alpha)}(x)$ are the generalized Laguerre polynomials which are the eigenfunctions of the Fourier–Bessel transform (Abramowitz and Stegun, 1964). A low order N assumes a radial Gaussian behaviour, as in (Özarslan et al., 2006; Assaf and Basser, 2005). In contrast, a high order N leads to a model-free estimation. Fig. 13 illustrates the actual adequacy of the first R_n functions in an experimental MR signal from erythrocytes (cf. Fig. 10). The scale factor ζ can be easily estimated from experimental values of decay on data samples.

5.8.2. Model estimation from the data

The signal approximation in the SPF basis defined in Eq. (105) requires the computation of the coefficients c_{lm} and d_{lm}:

$$a_{nlm} = \int_{\mathbf{q} \in \mathbb{R}^3} E(\mathbf{q}) \Psi_{nlm}(\mathbf{q}) d\mathbf{q}. \tag{109}$$

For a set of n_q samples in the q-space, the computation of the coefficients a_{lm} leads to a system of n_q linear equations, which can be solved using linear weighted least squares. In the case where the noise is prominent, Assemlal et al. (2009a) use a variational framework to simultaneously estimate and regularize the diffusion

image. The estimation process is based on a maximum a posteriori Rician probability (MAP), which takes into account the empirical nature of the noise.

5.8.3. Processing and extraction of diffusion features

Additionally, Assemlal et al. (2009a) introduce a generic framework for the extraction of various features of the diffusion, and *a fortiori* of brain microstructure at a local voxel scale. Since we have a continuous representation of E from the SPF coefficients, let $\mathcal{G}(\mathbf{k}) = \int P(\mathbf{p}) h_{\mathbf{k}}(\mathbf{p}) d\mathbf{p}$ be a characteristic $\mathcal{G}$ of the PDF at point $\mathbf{k}$, where $h_{\mathbf{k}}$ denotes a projection function at point $\mathbf{k}$. Table 1 represents several popular characteristics $\mathcal{G}$ which can be evaluated using this computational scheme. As a result, any characteristic $\mathcal{G}$ defined from Eq. (110) can be computed directly from the SPF coefficients. Indeed, since the SPF are an orthonormal basis the following relation holds:

$$\mathcal{G}(\mathbf{k}) = \int_{\mathbf{p} \in \mathbb{R}^3} P(\mathbf{p}) H_{\mathbf{k}}(\mathbf{p}) d\mathbf{p} = \int_{\mathbf{q} \in \mathbb{R}^3} E(\mathbf{q}) h_{\mathbf{k}}(\mathbf{q}) d\mathbf{q}$$
$$= \sum_{n,l,m}^{\infty} a_{n,l,m} b_{n,l,m}^{\mathbf{k}}. \tag{110}$$

where $H_{\mathbf{k}}$ is the inverse three-dimensional Fourier transform of $h_{\mathbf{k}}$ and $a_{nlm}, b_{nlm}^{\mathbf{k}}$ respectively denote the SPF expansion of E and $H_{\mathbf{k}}$. Therefore, the computation of a propagator feature $\mathcal{G}(\mathbf{k})$ from Eq. (110) simply turns into a very fast dot product between two vectors of SPF coefficients.

In addition, to the above framework, Cheng et al. (2010b), Cheng et al. (2010a) have recently demonstrated analytical solutions for the diffusion propagator (PDF) and the ODF (see Table 1).

5.8.4. Advantages and limitations

+ The diffusion signal is estimated without any prior assumptions about its radial or angular profile.
+ The number of samples in the q-space required for the estimation of the full diffusion signal is moderate (approximately 120 samples as reported in (Assemlal et al., 2009a)).
+ In addition to the fast linear estimation, the variational framework enables a robust estimation which takes into account the Rician distribution of the noise.
+ The SPF expansion method enables the linear extraction of various propagator features *directly* from the SPF coefficients. It does not require the reconstruction of the full diffusion propagator at first to extract one feature. in contrast to the DSI, GDTI, DPI and Tomographic reconstruction methods, and thus avoid unnecessary computations which may compromise the numerical accuracy.
+ Albeit not required, the analytical formula of the diffusion propagator features given in Table 1 improve the accuracy of the results.

Table 1
Some features $\mathcal{G}$ of the diffusion propagator P which can be computed in the SPF framework (Assemlal et al., 2009a; Assemlal, 2010), with their respective projection functions, $H_{\mathbf{k}}$.

Features, $\mathcal{G}$	Projection functions, $\bar{h}_{\mathbf{k}}$
Zero displacement probability	$4\sqrt{\pi}(-1)^n \gamma^{3/4} \sqrt{\frac{\Gamma(n+3/2)}{n!}} \delta_{l0}\delta_{m0}$
Funk-Radon Transform (FRT)	$q'^2 R_n(q') 2\pi P_l(0) y_l^m(\mathbf{k})$
Zeroth-order orientation density function (ODF$_0$)	$\frac{2\pi\zeta}{2} \sum_{j=0}^n \kappa_n(\zeta) \binom{j-1/2}{j} (-1)^{n-j} P_l(0) y_l^m(\mathbf{k})$
Second-order orientation density function (ODF$_2$)	$4\pi(-1)^n \gamma^{3/4} \sqrt{\frac{\Gamma(n+3/2)}{n!}} P_l(0) y_l^m(\mathbf{k})$
Diffusion Propagator (PDF)	$4(-1)^{l/2} \frac{\zeta^{(l+3)/2}\pi^{l+3/2}k^l}{\Gamma(l+3/2)} \kappa_n(\zeta)$
	$\sum_{j=0}^n \frac{(-1)^j}{j!} \binom{n+1/2}{n-j} 2^{l/2+j-1/2} \Gamma(l/2+j+3/2)1F1\left(\frac{2j+l+3}{2}; l+\frac{3}{2}; -2\pi^2 k^2\zeta\right) y_l^m(\mathbf{k})$

Table 2
The main q-space sampling methods in dMRI, their respective hardware requirements and the features which can be extracted using each.

Type of sampling	Number of samples standard acquisition	Gradient maximum (s/mm^2)	Type of features
Single	1	$\leqslant 1000$	Scalar
Low angular resolution (LARDI)	$\geqslant 7$	$\leqslant 1500$	Scalar, angular
High angular resolution (HARDI)	$\geqslant 25$	$\leqslant 3000$	Scalar, angular
Radial only (RMN)	$\geqslant 20$	$\leqslant 10,000$	Scalar, radial
Sparse sampling	$\geqslant 100$	$\leqslant 5000$	Scalar, radial, angular
Full sampling (DSI)	$\geqslant 200$	$\leqslant 8000$	Scalar, radial, angular

- The robust estimation is based on a slow iterative process, approximately one hour for a $128 \times 128 \times 64$ image with 65 samples in the q-space (Assemlal et al., 2009a).
- The diffusion is a positive process (Wedeen et al., 2005), however the linear estimation gives no guarantee that the approximated diffusion signal in the SPF basis remains positive.

6. Conclusion

Despite its many successes, diffusion MRI has one major weakness – the acquisition time for a diffusion image sequence of a brain at full resolution is approximately one hour. During this time the patient must lie motionless, which is infeasible for clinical applications. The methods described in this review of the literature suggest a possible way to overcome this constraint, namely, by sparse sampling of q-space combined with angular and radial reconstruction. The existing methods in the literature can be classified into three groups, based on the nature of sampling used:

- *Angular* sampling only: These can be used for ODF reconstruction, for finding isoprobability surfaces, and for fiber tracking in brain white matter.
- *Radial* sampling only: These can be used for measurement of the apparent kurtosis coefficient and of the "diffusion–diffraction" phenomena, and
- *Combined* angular and radial sampling: These can be used for improved ODF reconstruction and for inferring the full diffusion propagator (PDF).

For each manner of q-space sampling, Table 2 summarizes the hardware requirements and the main features that have been proposed in the literature.

Due to the limited number of samples of the diffusion signal in practice, a direct processing of the input data is typically not reliable. Therefore numerous reconstruction models have been proposed in the literature, of which a large set have been described in this review. These methods can be grouped into two categories:

1. Those for which the estimation of the signal with parametric models is based on strong prior assumptions. Such models can drastically reduce the number of required samples, provided their complexity remains manageable (*i.e.*, only a few parameters characterize the model). Nonetheless, a simple model may not be adequate particularly in situations where the cause and nature of the diffusion process is under investigation; and

2. Those for which the reconstruction of the diffusion signal is carried out without prior assumptions, by factorizing using a infinite number of basis functions. Mathematically, such methods ensure a perfect reconstruction of the signal. In practice, however, the low number of samples of the diffusion signal leads to the constraint that the infinite summation must be truncated. As a consequence, these methods impose a weak, implicit prior which depends on the particular choice of basis functions used.

Looking at the issue of clinical feasibility, the DTI method is the most popular since it has several advantages. It is fast and easy to implement and leads to an acceptable and reproducible approximation when the underlying microstructure is relatively coherent, *i.e.*, oriented in one single direction.

Although the error of the DTI method in modeling the diffusion signal at a voxel scale is modest, it can be amplified by iterative fiber tracking algorithms, resulting in non-reproducible neural pathways. In addition, DTI cannot detect subtle modifications in the diffusion pattern induced by various neuronal diseases. Therefore it is already apparent that there is a strong need to move from DTI to HARDI acquisitions. Yet, which modeling method to choose among those that are presently clinically feasible is non-trivial and the answer depends on several constraints including the actual application, the scan time and the scanner performance. The Q-Ball Imaging technique (Section 3.5) was the first method to take advantage of HARDI acquisition and as such is still widely successful, since it exhibits relatively little variation in the results when compared with other HARDI modeling methods.

At first sight, it might seem that the development of highly precise modeling methods of the diffusion signal is inappropriate in contrast to DTI given the constant reduction of voxel size in the last two decades. Indeed, one might envision voxel size converging to the dimension of an axon in the future, thus eliminating the need for higher order models altogether. In reality, such voxel size reduction will not be feasible in the current state since it would dramatically decrease the SNR as fewer and fewer water molecules would generate the diffusion signal. Introducing higher magnetic field strength in MRI scanners while keeping within the limits that can be tolerated by human subjects, might compensate for this loss in SNR.

Appendix A

In this section, we review the mathematical notation and the tools required for understanding the estimation methods used in DMRI analysis and reconstruction.

A.1. Spherical coordinates

Recall that $\mathbf{q} = (2\pi)\gamma\delta\mathbf{g}$, this suggests that the spherical nature of q-space sampling arises from the gradient hardware limitations of MRI scanners. Whereas there are virtually no limit to the number of orientations $\mathbf{q}/\|\mathbf{q}\|$ of the q-space one can acquire, the radial sampling using different diffusion wave-vector norm $\|\mathbf{q}\|$ pushes the gradient hardware of MRI scanners to its limits. This leads naturally to the processing of the acquired data in a spherical coordinates system.

We define the radius as $q \in [0,\infty[$, the colatitude angle $\theta \in [0,\pi]$ and the longitudinal angle $\phi \in [0,2\pi[$ in accordance with the conventions of physics. Fig. 14 illustrates the definition of spherical coordinates for a point $\mathbf{q} \in \mathbb{R}^3$ (see Fig. 15):

$$\mathbf{q} = q \cdot \mathbf{u}, \text{with } q = \|\mathbf{q}\| \text{ and } \mathbf{u} = \frac{\mathbf{q}}{\|\mathbf{q}\|} \in \mathcal{S}^2. \tag{111}$$

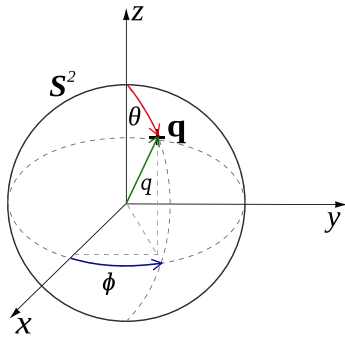**Fig. 14.** An illustration of spherical coordinates. The point $\mathbf{q} \in [0, \infty)$ is defined by its radius q, and its two angles θ, ϕ.
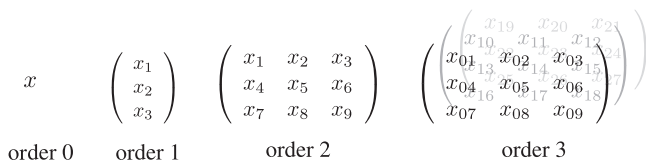

Fig. 15. Tensors components of increasing order. Left to right: a scalar, a vector, a matrix and a tensor of order 3.

The Cartesian coordinates are expressed as:

$$x = q\cos(\phi)\sin(\theta) \quad q = \sqrt{x^2 + y^2 + z^2} \tag{112}$$

$$y = q\sin(\phi)\sin(\theta) \quad \theta = \arccos(z/q) \tag{113}$$

$$z = q\cos(\theta) \quad \phi = \arctan(z/q) \tag{114}$$

The infinitesimal differential elements of surface area $d\mathbf{u}$ and volume $d\mathbf{q}$ are defined as:

$$d\mathbf{u} = \sin(\theta)\,d\theta d\phi, \tag{115}$$

$$d\mathbf{q} = q^2\sin(\theta)\,dq d\theta d\phi. \tag{116}$$

In the following, we review two mathematical tools that are widely used in DMRI, since they ease the modeling of the diffusion image from experimental observations: tensors and spherical harmonics.

A.2. Tensors

A.2.1. Definition

A *tensor* is a mathematical object which generalizes the notion of scalars (order 0 tensors), vectors (order 1 tensors) and matrices (order 2 tensors). A tensor does not depend on a reference system, indeed the tensor object $\mathbf{T}$ should not confused with its components $T_{j_1 \ldots j_q}^{i_1 \ldots i_p}$ which do depend on the choice of a specific coordinate system. The tensor object itself $\mathbf{T}$, however, remains invariant under changes in the coordinate system.

Let V be a finite-dimensional vector space. A tensor $\mathbf{T}$ of type (m, n) and of order $m + n$ is defined by a multilinear application $T^{(m,n)}(V) \to \mathbb{R}$ (Borisenko and Tarpov, 1980; Abraham et al., 1988):

$$T^{(m,n)}(V) = \underbrace{V \otimes \ldots \otimes V}_{m} \otimes \underbrace{V^* \otimes \ldots \otimes V^*}_{n} \tag{117}$$

where $\otimes$ stands for the tensor product and V^* is the symbol for the dual of V, defined as the vector space of the linear functional on V. Let $\{\mathbf{e}_1, \ldots, \mathbf{e}_m\} \in V$ and $\{\mathbf{e}^1, \ldots, \mathbf{e}^n\} \in V^*$ be the respective basis in V and V^*. The components of the tensor $\mathbf{T} \in T^{(m,n)}(V)$ are then expressed as:

$$\mathbf{T} = T_{j_1 \ldots j_n}^{i_1 \ldots i_p}\left(\mathbf{e}_{i_1} \otimes \ldots \otimes \mathbf{e}_{i_m} \otimes \mathbf{e}^{j_1} \otimes \ldots \otimes \mathbf{e}^{j_n}\right). \tag{118}$$

The notation for tensor components $T_{j_1 \ldots j_n}^{i_1 \ldots i_m}$ is quite similar to that for matrices ($\mathbf{T} = (T_{ij})$). A matrix is a tensor of type $(1, 1)$ so that $\mathbf{T} \in T^{(1,1)}$ and is written as $\mathbf{T} = T_i^j(\mathbf{e}_i \otimes \mathbf{e}^j)$ in tensor notation. However, unlike a matrix which has two indexes, a tensor has $m + n$ indices. We refer the reader to (Borisenko and Tarpov, 1980; Abraham et al., 1988), for a more precise definition of tensors and their properties.

A.2.2. The second-order tensor

In DMRI, the diffusion tensor refers to the generalization of the apparent diffusion coefficient D to a second-order tensor $\mathbf{D}$, which is symmetric and with positive entries, i.e., $\forall \mathbf{x} \in \mathbb{R}^3, \mathbf{x}^T\mathbf{D}\mathbf{x} \geqslant 0$. Under this assumption, the components $\mathbf{D}^{XYZ}$ of the tensor in an XYZ frame of reference are expressed as a 3×3 symmetric and positive-definite matrix:

$$\mathbf{D}_{XYZ} = \begin{pmatrix} D_{xx} & D_{xy} & D_{xz} \\ D_{xy} & D_{yy} & D_{yz} \\ D_{xz} & D_{yz} & D_{zz} \end{pmatrix}. \tag{119}$$

The orientation of this tensor is often expressed by using a basis consisting of eigenvectors $\mathbf{e} = (\mathbf{e}_1, \mathbf{e}_2, \mathbf{e}_3)$, so that the tensor components form a diagonal matrix $\mathbf{D}_\lambda$ whose elements λ_i are the eigenvalues. In this setting, the tensor $\mathbf{D}$ is often visualized as an ellipsoid with its major axis directions and lengths given by the eigenvectors and eigenvalues (see Fig. 16). As illustrated in Fig. 17, the expression of $\mathbf{D}$ in its own basis allows for the extraction of diffusion features: orientation of the diffusion by the principal eigenvector, and anisotropy using computations based on eigenvalues.

A.2.3. A tensor field

A tensor field is a tensor valued function defined on a topological space. In other words, each point of the field is associated with a tensor $\mathbf{T}$. In the same fashion that a tensor object can be represented in several ways (using an ellipsoid, a parallelepiped, *etc.*), there are several graphical representations of tensor fields, as shown in Fig. 18. Fig. 19 gives examples of first-order and second-order tensor fields. We refer the reader to (Tschumperlé and Deriche, 2005; Weickert and Hagen, 2006) for an introduction to tensor fields and their applications.
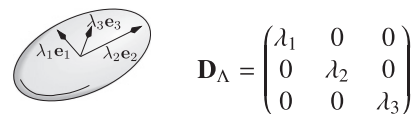

Fig. 16. The second-order diffusion tensor represented by an ellipsoid whose components are defined by a 3×3 symmetric positive-definite matrix. When the diffusion tensor is expressed in the basis of eigenvectors $\mathbf{e}_i$ and eigenvalues λ_i, the matrix components $\mathbf{D}_\Lambda$ are diagonal.

$$\mathbf{D}_\Lambda = \begin{pmatrix} \lambda_1 & 0 & 0 \\ 0 & \lambda_2 & 0 \\ 0 & 0 & \lambda_3 \end{pmatrix}$$

$$\begin{pmatrix} 1 & 0 & 0 \\ 0 & 1 & 0 \\ 0 & 0 & 1 \end{pmatrix} \quad \begin{pmatrix} 1 & 0 & 0 \\ 0 & 0.5 & 0 \\ 0 & 0 & 0.5 \end{pmatrix} \quad \begin{pmatrix} 1 & 0.4 & 0.2 \\ 0.4 & 0.8 & 0.9 \\ 0.2 & 0.9 & 0.2 \end{pmatrix}$$
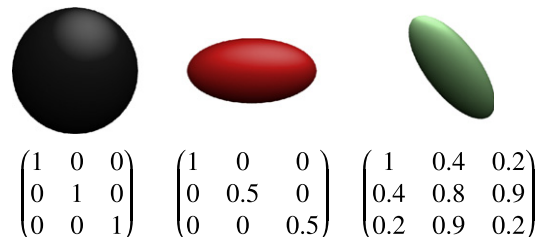
Fig. 17. Examples of second-order diffusion tensors and their corresponding matrices. From left to right: isotropic diffusion, diffusion that is dominant in the direction of the X axis; and diffusion in an oblique direction.
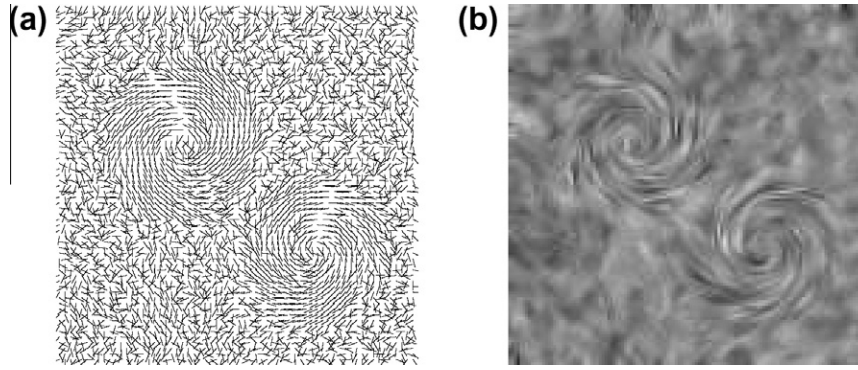
Fig. 18. Some possible representations of a first-order tensor field: (a) Representation by a set of icons (arrows). (b) An image whose intensity varies with the strength and direction of smoothing of a random image using *line integral convolution* (LIC) (Cabral and Leedom, 1993; Stalling and Hege, 1995; Tschumperlé and Deriche, 2005).
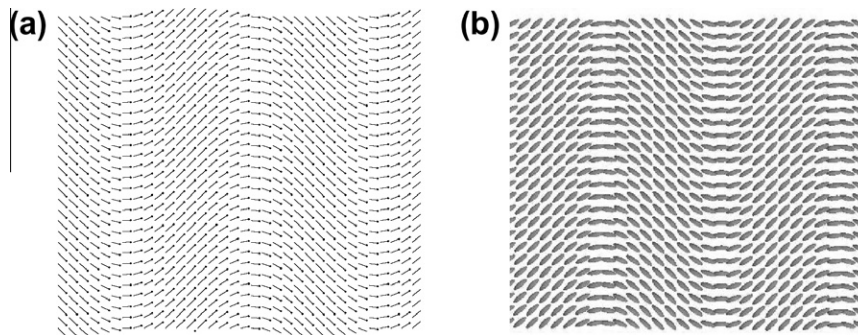

Fig. 19. The concept of a tensor field (b) generalizes the notion of a vector field (a). The topological space used here is the two-dimensional Euclidean space, where each tensor is represented by (a) an arrow for a first-order tensor of $T^{((1,0))}(\mathbb{R}^3)$ and (b) an ellipsoid for a second-order tensor of $T^{((1,1))}(\mathbb{R}^3)$.

The modeling of the diffusion image by a tensor field was proposed in the classical method of diffusion tensor imaging (DTI) (Basser et al., 1994), where diffusion in the q-space is modeled by a tensor of order two. We now discuss another model that is adapted to a spherical sampling of q-space, namely, spherical harmonics.

A.3. The spherical harmonics

There are many functions to approximate a function on the sphere. Among these possibilities spherical harmonics (SH) are particularly suited to the processing of diffusion images, because they have the following advantages:

1. This basis is adapted to a spherical sampling of the q-space commonly called high angular resolution imaging (HARDI) (Tuch et al., 1999).
2. The spherical harmonic (SH) representation can express most signals in spherical media that are sufficiently compact and smooth, with a small number of coefficients.
3. The SH are the eigenfunctions of the Laplace–Beltrami operator, which allows one to sharpen or smooth the spherical shape by exploiting a simple linear relationship.
4. The rotation of the SH is expressed by a simple formula, which offers particular advantages in the SPF framework (as discussed in Section 5.8).

We refer the reader to (Arfken et al., 1985; Healy et al., 1998) for a comprehensive overview of the properties of spherical harmonics. In the following we present the definition of complex spherical harmonics, followed by a discussion of the subset of real symmetric spherical harmonics, with properties that are suitable for diffusion images.

A.3.1. Definitions

A function f is called *harmonic* when it satisfies the Laplace equation, whose expression in Cartesian coordinates (x, y, z) is given by:

$$\nabla^2 f = \left[\frac{\partial^2}{\partial x^2} + \frac{\partial^2}{\partial y^2} + \frac{\partial^2}{\partial z^2} \right] f = 0. \tag{120}$$

Eq. (120) is rewritten in spherical coordinates (q, θ, ϕ) as:

$$\frac{1}{q^2} \left[\frac{\partial}{\partial q} \left(q^2 \frac{\partial}{\partial r} \right) + \frac{1}{\sin\theta} \frac{\partial}{\partial \theta} \left(\sin\theta \frac{\partial}{\partial \theta} \right) + \frac{1}{\sin^2\theta} \frac{\partial^2}{\partial \phi^2} \right] f = 0 \tag{121}$$

The method of separation of variables q, θ and ϕ is used to solve the spherical Laplace Eq. (121), so we assume that f is written as (Courant and Hilbert, 1962):

$$f(q, \theta, \phi) = q^l \Theta(\theta) \Phi(\phi). \tag{122}$$

We are interested in solutions to the angular part of the Laplace Eq. (121). The combination of Eq. (121) and (122) gives:

$$\left[\frac{1}{\sin\theta} \frac{\partial}{\partial \theta} \left(\sin\theta \frac{\partial}{\partial \theta} \right) + \frac{1}{\sin^2\theta} \frac{\partial^2}{\partial \phi^2} + l(l+1) \right] f = 0. \tag{123}$$

Finally, the solutions of Eq. (123) are called *spherical harmonics* and are written for $l \in \mathbb{N}$ and $m \in \mathbb{Z}, m \in [-l, l]$ (Arfken et al., 1985) as:
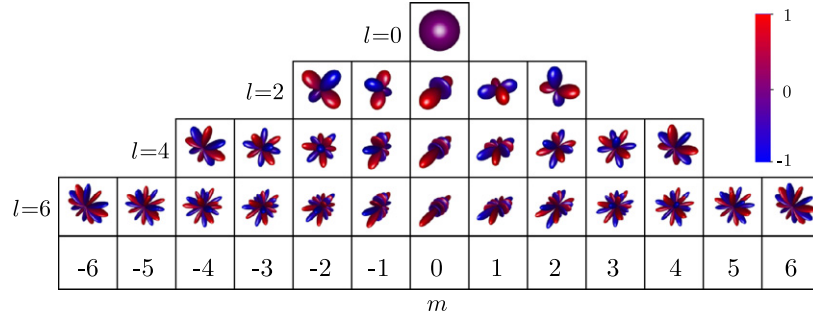
Fig. 20. The real and symmetric spherical harmonics (SH) for orders l = 0, 2, 4, 6. Blue indicates a negative value and red a positive value. The SH are normalized to lie in the range $[-1, 1]$. (For interpretation of the references to colour in this figure legend, the reader is referred to the web version of this article.)

$$Y_l^m(\theta, \phi) = \sqrt{\frac{2l+1}{4\pi}\frac{(l-m)!}{(l+m)!}}P_l^m(\cos\theta)e^{im\phi}, \qquad (124)$$

with P_l^m the generalized Legendre polynomials defined on the interval $[-1, 1]$:

$$P_l^m(x) = \begin{cases} \frac{1}{2^l l!}\frac{d}{dx^l}(x^2-1)^l & \text{si} \quad m = 0 \\ (-1)^m(1-x^2)^{m/2}\frac{d^m}{dx^m}P_l(x) & \text{si} \quad m > 0 \\ (-1)^{|m|}\frac{(l-|m|)!}{(l+|m|)!}P_l^{|m|}(x) & \text{si} \quad m < 0 \end{cases} \qquad (125)$$

The complex spherical harmonics Y_l^m from Eq. (124) form a basis of orthonormal functions:

$$\int_{\theta=0}^{\pi}\int_{\phi=0}^{2\pi} Y_l^m(\theta, \phi)\overline{Y_{l'}^{m'}}(\theta, \phi)\sin(\theta)d\theta d\phi = \delta_{ll'}\delta_{mm'} \qquad (126)$$

with $\overline{(z)}$ the complex conjugate and $\delta_{jj'}$ the Kronecker symbol, which is equal to one if $j = j'$ and is zero otherwise.

To simplify the notation, we introduce the following equivalence relation:

$$Y_l^m(\mathbf{u}) = Y_l^m(\theta, \phi). \qquad (127)$$

A.3.2. The Laplacian operator on the sphere

The Laplace–Beltrami operator is denoted by Δ_b and generalizes the Laplace operator for functions defined on surfaces and in particular on spheres. This operator is defined by:

$$\Delta_b = \frac{1}{\sin\theta}\frac{\partial}{\partial\theta}\left(\sin\theta\frac{\partial}{\partial\theta}\right) + \frac{1}{\sin^2\theta}\frac{\partial^2}{\partial\phi^2}. \qquad (128)$$

Since the Laplace-Beltrami operator is involved in the angular Laplace equation given by Eq. (123), the spherical harmonics satisfy the relation:

$$\Delta_b Y_l^m = -l(l+1)Y_l^m. \qquad (129)$$

This relationship is used in several approaches to the regularization and enhancement of spherical functions (Descoteaux et al., 2007; Assemlal et al., 2009a).

A.3.3. A real and symmetric subset

The number of samples of the observed signal determines the number of coefficients in the reconstruction by a sum of basis functions, here the SH. For a fixed number of coefficients, one should not "waste" these coefficients for the estimation of impossible or uninteresting shapes, but rather should use them wisely to gain accuracy. For this, two prior assumptions are commonly used in DMRI, which restrict the definition domain of spherical harmonics to the ideal diffusion signal (Alexander et al., 2002; Frank, 2002): (i) The signal is antipodally symmetric on the unit sphere, and (ii) it is real and positive.

Many approaches in the literature assume that the diffusion at a voxel-scale is symmetric on the sphere. For this, the SH has an interesting property when subjected to a transformation T:

$$T : (\theta, \phi) \rightarrow (\pi - \theta, \pi + \phi)$$

$$Y_l^m(T(\theta, \phi)) = \begin{cases} Y_l^m(\theta, \phi) & \text{if} \quad l \in 2\mathbb{N} \\ -Y_l^m(\theta, \phi) & \text{if} \quad l \notin 2\mathbb{N} \end{cases} \qquad (130)$$

Eq. (130) implies that when the l is even, the spherical function is symmetric on the unit sphere. Also, a symmetric function on the sphere can be expressed as a series of SH with even order l.

In addition, although in theory the diffusion MRI signal E is captured in the complex domain $\mathcal{C}$, in practice the use of the real part of E allows one to overcome the sensitivity due to phase artifacts, which can be generally regarded as noise (Tuch, 2002; LeBihan et al., 2006).

Using these two prior assumptions we can define a new basis of real *and* symmetric SH (Frank, 2002; Anderson, 2005; Hess et al., 2006; Descoteaux et al., 2007):

$$y_l^m = \begin{cases} \sqrt{2}\Re(Y_l^m) & \text{if} \quad 0 < m \leqslant l \\ Y_l^0, & \text{if} \quad m = 0 \qquad \text{avec } l \in 2\mathbb{N} \\ \sqrt{2}\Im(Y_l^{|m|}) & \text{if} \quad -l \leqslant m < 0 \end{cases} \qquad (131)$$

Fig. 20 illustrates the SH y_l^m for the first few orders of l, which capture the low frequencies on the unit sphere. In the following, we introduce the equivalent notation to facilitate the presentation:

$$j(l, m) = \frac{l(l+1)}{2} + m \quad \text{avec } l \in 2\mathbb{N} \qquad (132)$$

$$y_j(\theta, \phi) = y_l^m(\theta, \phi). \qquad (133)$$

The real and symmetric spherical harmonics form an *orthonormal* basis on the unit sphere (Blanco et al., 1997):

$$\int_{\mathbf{u}\in\mathcal{S}^2} y_j(\mathbf{u})y_{j'}(\mathbf{u})d\mathbf{u} = \delta_{jj'}. \qquad (134)$$

We have seen that the basis of spherical harmonics $\{y_j\}$ breaks down most spherical continuous functions into a Fourier series expansion on the sphere.

A.3.4. Rotation of spherical harmonics

We now review the mathematical tools that are necessary for understanding the rotation of real spherical harmonics, namely the Euler angles and the Wigner rotation matrix.

Euler angles: The Euler angles have been developed to describe the rotation of a rigid object in three-dimensional Euclidean space $\mathbb{R}^3$. The specific orientation of an object is obtained by a sequence of three successive rotations given by the Euler angles, as illustrated in Fig. 21:
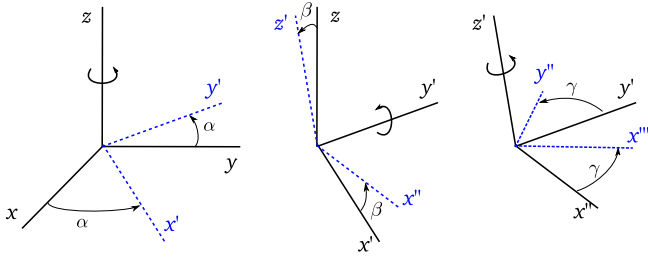
Fig. 21. Rotation with Euler angles (α, β, γ) in the *zyz* configuration. From left to right: rotation around the axis *z*, *y′* and *z′*. The axes after rotation are shown in dotted lines.

1. the rotation by angle α around the axis *z* which transforms the frame of reference from *xyz* to *x′y′z*;
2. the rotation by angle β around the axis *y′* which transforms the frame of reference from *x′y′z* to *x″y′z′*;
3. the rotation by angle γ around the axis *z′* which transforms the frame of reference *x″y′z′* to *x‴y″z′*.

Remark. There are twelve variants of the rotation scheme of Euler angles, which differ in the axis of rotation chosen from each of the three previous steps. In this paper, we adopt, without loss of generality, the configuration *zyz* (Blanco et al., 1997).

Wigner rotation matrix: When subject to a rotation expressed in terms of Euler angles (α, β, γ), complex spherical harmonics Y_l^m of order *l* can be expressed as a linear combination of spherical harmonics of even order $Y_l^{m'}$:

$$\text{Rot}_{\alpha,\beta,\gamma}\left[Y_l^m(\theta,\phi)\right] = \sum_{m'=-l}^{l} Y_l^{m'}(\theta,\phi)\left[e^{-im'\alpha} d_{m'm}^{(l)}(\beta) e^{-im\gamma}\right] \quad (135)$$

with the *d-small Wigner matrix* defined as (Su and Coppens, 1994):

$$d_{m'm}^{(l)}(\beta) = \left[\frac{(l+m')!(l-m')!}{(l+m)!(l-m)!}\right]^{1/2}$$
$$\sum_{k=\max(0,m-m')}^{\min(l-m',l+m)}\left[(-1)^{k+m'-m}\binom{l+m}{k}\binom{l-m}{l-m'-k}\right.$$
$$\left.(\cos\beta/2)^{2l+m-m'-2k}(\sin\beta/2)^{2k+m'-m}\right]. \quad (136)$$

We are interested in the *real* Wigner rotation matrix $D(M'M)((l))$ such that

$$\text{Rot}_{\alpha,\beta,\gamma}[y_l^m(\theta,\phi)] = \sum_{m'=-l}^{l} y_l^{m'}(\theta,\phi) D_{m'm}^{(l)}(\alpha,\beta,\gamma). \quad (137)$$

We saw in Eq. (131) that real spherical harmonics are defined by a linear combination of complex spherical harmonics. Then the *d*-small Wigner matrix of Eq. (136), for real spherical harmonics is expressed as (Ritchie, 1998) Appendix B.4:

$$D_{m'm}^{(l)} = \begin{cases} d_{m'm}^{(l)}(\beta)\cos(F) + (-1)^{m'} d_{-m'm}^{(l)}(\beta)\cos(G) & m' \geqslant 0, m \geqslant 0 \\ (-1)^{m'+1} d_{m'm}^{(l)}(\beta)\sin(F) + d_{-m'm}^{(l)}(\beta)\sin(G) & m' < 0, m \geqslant 0 \\ (-1)^{m} d_{m'm}^{(l)}(\beta)\sin(F) + (-1)^{m+m'} d_{-m'm}^{(l)}(\beta)\sin(G) & m' \geqslant 0, m < 0 \\ (-1)^{m+m'} d_{m'm}^{(l)}(\beta)\cos(F) + (-1)^{m+1} d_{-m'm}^{(l)}(\beta)\cos(G) & m' < 0, m < 0 \end{cases}$$
$$\quad (138)$$

with $F = m\gamma + m'\alpha$ and $G = m\gamma - m'\alpha$.

References

Aganj, I., Lenglet, C., Sapiro, G., 2009a. ODF reconstruction in q-ball imaging with solid angle consideration. In: IEEE International Symposium on Biomedical Imaging: From Nano to Macro, 2009 (ISBI'09). IEEE, pp. 1398–1401.

Aganj, I., Lenglet, C., Sapiro, G., Yacoub, E., Ugurbil, K., Harel, N., 2009b. Multiple Q-shell ODF reconstruction in Q-ball imaging. In: International Conference on Medical Image Computing and Computer-Assisted Intervention. Medical Image Computing and Computer-Assisted Intervention (MICCAI), vol. 12, p. 423.

Alexander, D., 2005. Maximum entropy spherical deconvolution for diffusion MRI. Image Processing in Medical Imaging, 76–87.

Alexander, D., Barker, G., Arridge, S., 2002. Detection and modeling of non-Gaussian apparent diffusion coefficient profiles in human brain data. Magnetic Resonance Imaging 48, 331–340.

Anderson, A., 2005. Measurement of fiber orientation distributions using high angular resolution diffusion imaging. Magnetic Resonance in Medicine 54 (5).

Anderson, A., Ding, Z., 2002. Sub-voxel measurement of fiber orientation using high angular resolution diffusion tensor imaging. In: Proceedings of the 10th Annual Meeting of ISMRM, p. 440.

Andrews, G., Askey, R., Roy, R., 1999. Special Functions. Cambridge University Press.

Anwander, A., Tittgemeyer, M., Von Cramon, D., Friederici, A., Knosche, T., 2007. Connectivity-based parcellation of Broca's area. Cerebral Cortex 17 (4), 816.

Arfken, G., Weber, H., Weber, H., 1985. Mathematical Methods for Physicists. Academic Press, New York.

Arsigny, V., 2006. Processing data in Lie groups: an algebraic approach. application to non-linear registration and diffusion tensor MRI. Ph.D. thesis, École polytechnique.

Assaf, Y., Basser, P.J., 2005. Composite hindered and restricted model of diffusion (charmed) mr imaging of the human brain. NeuroImage 27, 48–58.

Assaf, Y., Cohen, Y., 1998. In vivo and in vitro bi-exponential diffusion of n-acetyl aspartate (naa) in rat brain: a potential structural probe? NMR in Biomedicine, 11.

Assemlal, H.-E., 2010. Traitement et analyse d'images IRM de diffusion pour l'estimation de l'architecture locale des tissus. Ph.D. thesis, Université de Caen.

Assemlal, H.-E., Tschumperlé, D., Brun, L., 2009a. Efficient and robust computation of pdf features from diffusion mr signal. Medical Image Analysis 13 (5), 715–729.

Assemlal, H.-E., Tschumperlé, D., Brun, L., 2009b. Evaluation of q-space sampling strategies for the diffusion magnetic resonance imaging. In: Proceedings of the 12th International Conference on Medical Image Computing and Computer-Assisted Intervention: Part II. Springer-Verlag, pp. 406–414.

Aubert, G., Kornprobst, P., 2006. Mathematical Problems in Image Processing: Partial Differential Equations and the Calculus of Variations. Springer-Verlag New York Inc..

Bao, L., Zhu, Y., Liu, W., Croisille, P., Pu, Z., Robini, M., Magnin, I., 2009. Denoising of human cardiac diffusion tensor magnetic resonance images using sparse representation combined with segmentation. Physics in Medicine and Biology 54, 1435–1456.

Bar-Shir, A., Avram, L., Özarslan, E., Basser, P.J., Cohen, Y., 2008. The effect of the diffusion time and pulse gradient duration ratio on the diffraction pattern and the structural information estimated from q-space diffusion MR: experiments and simulations. Journal of Magnetic Resonance (San Diego, CA: 1997) 194 (2), 230–236.

Barmpoutis, A., Jian, B., Vemuri, B.C., Shepherd, T.M., 2007. Symmetric positive 4th order tensors & their estimation from diffusion weighted MRI. In: Proceedings of IPMI, pp. 308–319.

Basser, P., 1995. Inferring microstructural features and the physiological state of tissues from diffusion-weighted images. NMR in Biomedicine 8 (7).

Basser, P., 1997. New histological and physiological stains derived from diffusion-tensor MR images. Annals of the New York Academy of Sciences 820 (1 Imaging Brain Structure and Function: Emerging Technologies in the Neurosciences), 123–138.

Basser, P., 2002. Relationships between diffusion tensor and q-space MRI. Magnetic Resonance in Medicine 47 (2), 392–397.

Basser, P., LeBihan, D., 1992. Fiber orientation mapping in an anisotropic medium with nmr diffusion spectroscopy. In: Proceedings of the 11th Society of Magnetic Resonance in Medicine, p. 1221.

Basser, P., Mattiello, J., LeBihan, D., 1992. Diagonal and off-diagonal components of the self-diffusion tensor: their relation to and estimation from the nmr spin-echo signal. In: Proceedings of the 11th Society of Magnetic Resonance in Medicine, vol. 1, p. 1222.

Basser, P., Pajevic, S., Pierpaoli, C., Duda, J., Aldroubi, A., 2000. In vivo fiber tractography using dt-mri data. Magnetic Resonance in Medicine 44 (4), 625–632.

Basser, P.J., Mattiello, J., LeBihan, D., 1994. Estimation of the effective self-diffusion tensor from the nmr spin echo. Journal of Magnetic Resonance 103, 247–254.

Basu, S., Fletcher, T., Whitaker, R., 2006. Rician noise removal in diffusion tensor MRI. In: MICCAI, pp. 117–125.

Behrens, T., Berg, H., Jbabdi, S., Rushworth, M., Woolrich, M., 2007. Probabilistic diffusion tractography with multiple fibre orientations: what can we gain? NeuroImage 34 (1), 144–155.

Behrens, T., Woolrich, M., Jenkinson, M., Johansen-Berg, H., Nunes, R., Clare, S., Matthews, P., Brady, J., Smith, S., 2003. Characterization and propagation of uncertainty in diffusion-weighted MR imaging. Magnetic Resonance in Medicine 50 (5), 1077–1088.

Blackman, R., Tukey, J., 1959. The Measurement of Power Spectra: From the Point of View of Communications Engineering. Dover Publications, New York.

Abraham, R., Marsden, J., Ratio, T., 1988. Manifolds, Tensor Analysis, and Applications. Springer.

Abramowitz, M., Stegun, I., 1964. Handbook of Mathematical Functions with Formulas, Graphs, and Mathematical Tables. Dover Publications.

Blanco, M.A., Flórez, M., Bermejo, M., 1997. Evaluation of the rotation matrices in the basis of real spherical harmonics. Journal of Molecular Structure 419, 19–27.

Blees, M., 1994. The effect of finite duration of gradient pulses on the pulsed-field-gradient NMR method for studying restricted diffusion. Journal of Magnetic Resonance, Series A 109 (2), 203–209.

Bloy, L., Verma, R., 2008. On computing the underlying fiber directions from the diffusion orientation distribution function. In: Metaxas, D., Axel, L., Fichtinger, G., Székely, G. (Eds.), Proceeding of Medical Image Computing and Computer-Assisted Intervention (MICCAI), LNCS, vol. 5241. Springer, pp. 1–8.

Borisenko, A., Tarpov, I., 1980. Vector and Tensor Analysis with Applications. Dover, New York.

Branch, M., Coleman, T., Li, Y., 2000. A subspace, interior, and conjugate gradient method for large-scale bound-constrained minimization problems. SIAM Journal on Scientific Computing 21 (1), 1–23.

Brownstein, K.R., Tarr, C.E., 1979. Importance of classical diffusion in nmr studies of water in biological cells. Physical Review A 19 (6), 2446–2453.

Burt, P., Adelson, E., 1983. The Laplacian pyramid as a compact code. IEEE Transactions on Communications 31 (4), 532–540.

Cabral, B., Leedom, L., 1993. Imaging vector fields using line integral convolution. In: Proceedings of the 20th Annual Conference on Computer Graphics and Interactive Techniques. ACM, New York, NY, USA, pp. 263–270.

Callaghan, P., 1991. Principles of Nuclear Magnetic Resonance Microscopy. Oxford University Press, USA.

Callaghan, P., Coy, A., MacGowan, D., Packer, K., Zelaya, F., 1991. Diffraction-like effects in nmr diffusion studies of fluids in porous solids. Nature 351 (6326), 467–469.

Campbell, J., Siddiqi, K., Rymar, V., Sadikot, A., Pike, G., 2005. Flow-based fiber tracking with diffusion tensor and q-ball data: validation and comparison to principal diffusion direction techniques. NeuroImage 27 (4), 725–736.

Canales-Rodríguez, E., Lin, C., Iturria-Medina, Y., Yeh, C., Cho, K., Melie-García, L., 2010. Diffusion orientation transform revisited. NeuroImage 49 (2), 1326–1339.

Candès, E., Romberg, J., Tao, T., 2006. Robust uncertainty principles: exact signal reconstruction from highly incomplete frequency information. IEEE Transactions on Information Theory 52 (2), 489–509.

Casimir, H.B.G., 1945. On onsager's principle of microscopic reversibility. Reviews of Modern Physics 17 (2-3), 343–350.

Chefd'hotel, C., Tschumperlé, D., Deriche, R., Faugeras, O., 2002. Constrained flows of matrix-valued functions: application to diffusion tensor regularization. In: Proceedings of the 7th European Conference on Computer Vision – Part I. Springer-Verlag, Copenhagen, Denmark, pp. 251–265.

Chefd'hotel, C., Tschumperlé, D., Deriche, R., Faugeras, O., 2004. Regularizing flows for constrained matrix-valued images. Journal of Mathematical Imaging and Vision 20 (1-2), 147–162.

Chen, Y., Guo, W., Zeng, Q., Yan, X., Huang, F., Zhang, H., He, G., Vemuri, B., Liu, Y., 2004. Estimation, smoothing, and characterization of apparent diffusion coefficient profiles from high angular resolution dwi. CVPR 1, 588–593.

Chen, Y., Guo, W., Zeng, Q., Yan, X., Rao, M., Liu, Y., 2005. Apparent diffusion coefficient approximation and diffusion anisotropy characterization in DWI. In: Proceedings of the 19th International Conference on Information Processing in Medical Imaging (IPMI). Springer, Glenwood Springs, CO, USA, pp. 246–257.

Cheng, J., Ghosh, A., Deriche, R., Jiang, T., 2010a. Model-free, regularized, fast, and robust analytical orientation distribution function estimation. In: Jiang, T., Navab, N., Pluim, J., Viergever, M. (Eds.), Proceedings of the Medical Image Computing and Computer-Assisted Intervention (MICCAI), Lecture Notes in Computer Science, vol. 6361. Springer, Berlin/Heidelberg, pp. 648–656.

Cheng, J., Ghosh, A., Jiang, T., Deriche, R., 2010b. Model-free and analytical EAP reconstruction via spherical polar fourier diffusion MRI. In: Proceedings of the Medical Image Computing and Computer-Assisted Intervention (MICCAI). Springer, pp. 590–597.

Chung, S., Lu, Y., Henry, R., 2006. Comparison of bootstrap approaches for estimation of uncertainties of DTI parameters. NeuroImage 33 (2), 531–541.

Clark, C., Le Bihan, D., 2000. Water diffusion and anisotropy at high b values in the human brain. Magnetic Resonance in Medicine 44, 852–859.

Cohen, Y., Assaf, Y., 2002. High b-value q-space analyzed diffusion-weighted mrs and MRI in neuronal tissues – a technical review. NMR in Biomedicine 15, 516–542.

Conturo, T., Lori, N., Cull, T., Akbudak, E., Snyder, A., Shimony, J., McKinstry, R., Burton, H., Raichle, M., 1999. Tracking neuronal fiber pathways in the living human brain. Proceedings of the National Academy of Sciences, vol. 96. National Acad Sciences, pp. 10422–10427.

Cory, D., Garroway, A., 1990. Measurement of translational displacement probabilities by nmr: an indicator of compartmentation. Magnetic Resonance in Medicine 14 (3), 435–444.

Courant, R., Hilbert, D., 1962. Methods of Mathematical Physics. Interscience, New York.

Coy, A., Callaghan, P., 1994. Pulsed gradient spin echo nuclear magnetic resonance for molecules diffusing between partially reflecting rectangular barriers. The Journal of Chemical Physics 101, 4599.

Cramér, H., 1957. Mathematical Methods of Statistics. Princeton University Press.

De Groot, S., Mazur, P., 1962. Non Equilibrium Thermodynamics. North Holland, Amsterdam.

Deans, S., 1983. The Radon Transform and Some of Its Applications. A Wiley-Interscience Publication, New York.

Defrise, M., De Mol, C., 1983. A regularized iterative algorithm for limited-angle inverse Radon transform. Journal of Modern Optics 30 (4), 403–408.

Deriche, R., Calder, J., Descoteaux, M., 2009. Optimal real-time q-ball imaging using regularized kalman filtering with incremental orientation sets. Medical Image Analysis 13 (4), 564–579.

Descoteaux, M., 2008. High angular resolution diffusion MRI: from local estimation to segmentation and tractography. Ph.D. thesis, University of Nice-Sophia Antipolis.

Descoteaux, M., Angelino, E., Fitzgibbons, S., Deriche, R., 2006. Apparent diffusion coefficients from high angular resolution diffusion imaging: estimation and applications. Magnetic Resonance in Medicine 56 (2).

Descoteaux, M., Angelino, E., Fitzgibbons, S., Deriche, R., 2007. Regularized, fast and robust analytical q-ball imaging. Magnetic Resonance in Medicine 58, 497–510.

Descoteaux, M., Deriche, R., Knosche, T.R., Anwander, A., 2009a. Deterministic and probabilistic tractography based on complex fibre orientation distributions. IEEE Transactions on Medical Imaging 28 (2), 269–286.

Descoteaux, M., Deriche, R., Le Bihan, D., Mangin, J., Poupon, C., 2009b. Diffusion propagator imaging: using Laplace's equation and multiple shell acquisitions to reconstruct the diffusion propagator. In: Proceedings of the Information Processing in Medical Imaging. Springer, pp. 1–13.

Donoho, D., 2002. De-noising by soft-thresholding. IEEE Transactions on Information Theory 41 (3), 613–627.

Einstein, A., 1905. On the movement of small particles suspended in stationary liquids required by the molecular-kinetic theory of heat. Annalen der Physik 17, 549–560.

Fasshauer, G., Schumaker, L., 1998. Scattered data fitting on the sphere. In: Mathematical Methods for Curves and Surfaces II.

Fillard, P., Pennec, X., Arsigny, V., Ayache, N., 2007. Clinical dt-mri estimation, smoothing, and fiber tracking with log-euclidean metrics. IEEE Transactions on Medical Imaging 26 (11), 1472–1482.

Filler, A., Tsuruda, J.S., Richards, T.L., Howe, F., 1992. Images, apparatus, algorithms and methods. UK Patent Office GB9210810.

Frank, L., 2002. Characterization of anisotropy in high angular resolution diffusion-weighted MRI. Magnetic Resonance in Medicine 47, 1083–1099.

Freeden, W., Gervens, T., Schreiner, M., 1998. Constructive Approximation on the Sphere. Clarendon Press.

Frøhlich, A., Østergaard, L., Kiselev, V., 2006. Effect of impermeable boundaries on diffusion-attenuated MR signal. Journal of Magnetic Resonance 179 (2), 223–233.

Ghosh, A., Descoteaux, M., Deriche, R., 2008a. Riemannian framework for estimating symmetric positive definite 4th order diffusion tensors. In: Metaxas, D., Axel, L., Fichtinger, G., Székely, G. (Eds.), Proceedings of the Medical Image Computing and Computer-Assisted Intervention (MICCAI), LNCS, vol. 5241. Springer, pp. 858–865.

Ghosh, A., Tsigaridas, E., Descoteaux, M., Comon, P., Mourrain, B., Deriche, R., 2008b. A polynomial based approach to extract the maxima of an antipodally symmetric spherical function and its application to extract fiber directions from the orientation distribution function in diffusion MRI. In: The Workshop on Computational Diffusion MRI (in MICCAI). Citeseer, pp. 237–248.

Grad, H., 1949. Note on N-dimensional Hermite polynomials. Communications on Pure and Applied Mathematics 2 (4).

Grebenkov, D., 2007. NMR survey of reflected Brownian motion. Reviews of Modern Physics 79 (3), 1077–1137.

Grebenkov, D., Guillot, G., Sapoval, B., 2007. Restricted diffusion in a model acinar labyrinth by NMR: theoretical and numerical results. Journal of Magnetic Resonance 184 (1), 143–156.

Gudbjartsson, H., Patz, S., 1995. The rician distribution of noisy MRI data. Magnetic Resonance in Medicine 34, 910–914.

Hagmann, P., 2005. From diffusion MRI to brain connectomics. Ph.D. thesis, École polytechnique fédérale de Lausanne.

Hagmann, P., Reese, T., Tseng, W., Meuli, R., Thiran, J., Wedeen, V., 2004. Diffusion spectrum imaging tractography in complex cerebral white matter: an investigation of the centrum semiovale. In: Proc. Intl. Soc. Mag. Reson. Med., vol. 12, pp. 15–21.

Healy, D., Hendriks, H., Kim, P., 1998. Spherical deconvolution. Journal of Multivariate Analysis 67 (1), 1–22.

Hess, C., Mukherjee, P., Han, E., Xu, D., Vigneron, D., 2006. Q-ball reconstruction of multimodal fiber orientations using the spherical harmonic basis. Magnetic Resonance in Medicine 56 (1), 104–117.

Hilbert, D., 1888. Ueber die Darstellung definiter Formen als Summe von formenquadraten. Mathematische Annalen 32 (3), 342–350.

Hosey, T., Williams, G., Ansorge, R., 2005. Inference of multiple fiber orientations in high angular resolution diffusion imaging. Magnetic Resonance in Medicine 54 (6), 1480–1489.

Hyslop, W., Lauterbur, P., 1991. Effects of restricted diffusion on microscopic NMR imaging. Journal of Magnetic Resonance 94 (3), 501–510.

Jansons, K., Alexander, D., 2003. Persistent angular structure: new insights from diffusion magnetic resonance imaging data. Inverse Problems 19 (5), 1031–1046.

Jensen, J., Helpern, J., Ramani, A., Lu, H., Kaczynski, K., 2005. Diffusional kurtosis imaging: the quantification of non-Gaussian water diffusion by means of magnetic resonance imaging. Magnetic Resonance in Medicine 53 (6), 1432–1440.

Jian, B., Vemuri, B.C., 2007. A unified computational framework for deconvolution to reconstruct multiple fibers from diffusion weighted MRI. IEEE Transactions on Medical Imaging 26 (11), 1464–1471.

Jian, B., Vemuri, B.C., Özarslan, E., Carney, P.R., Mareci, T.H., 2007. A novel tensor distribution model for the diffusion-weighted mr signal. NeuroImage 37, 164–176.

Johansen-Berg, H., Behrens, T., 2009. Diffusion MRI: From Quantitative Measurement to In Vivo Neuroanatomy. Academic Press, Elsevier.

Johnston, T.W., 1960. Cartesian tensor scalar product and spherical harmonic expansions in Boltzmann's equation. Physical Review 120 (4), 1103–1111.

Jones, D., Horsfield, M., Simmons, A., 1999a. Optimal strategies for measuring diffusion in anisotropic systems by magnetic resonance imaging. Magnetic Resonance in Medicine 42 (3), 515–525.

Jones, D., Simmons, A., Williams, S., Horsfield, M., 1999b. Non-invasive assessment of axonal fiber connectivity in the human brain via diffusion tensor MRI. Magnetic Resonance in Medicine 42 (1).

Kaden, E., Knösche, T., Anwander, A., 2007. Parametric spherical deconvolution: inferring anatomical connectivity using diffusion MR imaging. NeuroImage 37 (2), 474–488.

Kärger, J., Heink, W., 1983. The propagator representation of molecular transport in microporous crystallites. Journal of Magnetic Resonance 51 (1), 1–7.

Kendall, M., Stuart, A., 1977. The Advanced Theory of Statistics, furth ed. Distribution Theory, vol. 1 Griffin, London.

Kezele, I., Descoteaux, M., Poupon, C., Abrial, P., Poupon, F., Mangin, J., 2008. Multiresolution decomposition of HARDI and ODF profiles using spherical wavelets. In: The Computational Diffusion MRI Workshop (CDMRI'08), New York, pp. 225–234.

Khachaturian, M., Wisco, J., Tuch, D., 2007. Boosting the sampling efficiency of q-ball imaging using multiple wavevector fusion. Magnetic Resonance in Medicine 57, 289–296.

Köpf, M., Corinth, C., Haferkamp, O., Nonnenmacher, T., 1996. Anomalous diffusion of water in biological tissues. Biophysical Journal 70 (6), 2950–2958.

Köpf, M., Metzler, R., Haferkamp, O., Nonnenmacher, T., 1998. NMR studies of anomalous diffusion in biological tissues: experimental observation of Lévy stable processes. Fractals in Biology and Medicine 2, 354–364.

Kuchel, P., Coy, A., Stilbs, P., 1997. NMR diffusion–diffraction of water revealing alignment of erythrocytes in a magnetic field and their dimensions and membrane transport characteristics. Magnetic Resonance in Medicine 37 (5), 637–643.

Kuo, L.-W., Chen, J.-H., Wedeen, V.J., Tseng, W.-Y.I., 2008. Optimization of diffusion spectrum imaging and q-ball imaging on clinical MRI system. NeuroImage 41 (1), 7–18.

Landman, B.A., Wan, H., Bogovic, J.A., Bazin, P.-L., Prince, J.L., 2010. Resolution of crossing fibers with constrained compressed sensing using traditional diffusion tensor MRI. In: Proceedings of SPIE, vol. 7623, p. 76231H.

Le Bihan, D., 1991. Molecular diffusion nuclear magnetic resonance imaging. Magnetic Resonance Quarterly 7 (1), 1–30.

Le Bihan, D., van Zijl, P., 2002. from the diffusion coefficient to the diffusion tensor. NMR in Biomedicine 15 (7–8), 431–434.

LeBihan, D., Poupon, C., Amadon, A., Lethimonnier, F., 2006. Artifacts and pitfalls in diffusion MRI. Journal of Magnetic Resonance Imaging 24, 478–488.

Lee, N., Singh, M., 2010. Compressed sensing based diffusion spectrum imaging. In: Proceedings of the ISMRM, Stockholm, Sweden, pp. 1–8.

Lenglet, C., 2006. Geometric and variational methods for diffusion tensor MRI processing. Ph.D. thesis, University Nice Sophia-Antipolis.

Lenglet, C., Campbell, J., Descoteaux, M., Haro, G., Savadjiev, P., Wassermann, D., Anwander, A., Deriche, R., Pike, G., Sapiro, G., Siddiqi, K., Thompson, P., 2009. Mathematical methods for diffusion MRI processing. NeuroImage 45 (1, Suppl. 1), S111–S122.

Li, H., Manjunath, B., Mitra, S., 1995. Multisensor image fusion using the wavelet transform. Graphical Models and Image Processing 57 (3), 235–245.

Lin, C., Tseng, W., Cheng, H., Chen, J., 2001. Validation of diffusion tensor magnetic resonance axonal fiber imaging with registered manganese-enhanced optic tracts. NeuroImage 14 (5), 1035–1047.

Lin, C.-P., Wedeen, V.J., Chen, J.-H., Yao, C., Tseng, W.-Y.I., 2003. Validation of diffusion spectrum magnetic resonance imaging with manganese-enhanced rat optic tracts and ex vivo phantoms. NeuroImage 19 (3), 482–495.

Liu, C., Bammer, R., Acar, B., Moseley, M., 2004. Characterizing non-Gaussian diffusion by using generalized diffusion tensors. Magnetic Resonance in Medicine 51, 924–937.

Ljunggren, S., 1983. A simple graphical representation of fourier-based imaging methods. Journal of Magnetic Resonance 54, 338–343.

Luo, J., Zhu, Y., Magnin, I., 2009. Denoising by averaging reconstructed images: application to magnetic resonance images. IEEE Transactions on Biomedical Engineering 56 (3), 666–674.

Lustig, M., Donoho, D., Pauly, J., 2007. Sparse MRI: the application of compressed sensing for rapid MR imaging. Magnetic Resonance in Medicine 58 (6), 1182–1195.

Lythgoe, M., Busza, A., Calamante, F., Sotak, C., King, M., Bingham, A., Williams, S., Gadian, D., 1997. Effects of diffusion anisotropy on lesion delineation in a rat model of cerebral ischemia. Magnetic Resonance in Medicine 38 (4), 662–668.

Maier, S., Vajapeyam, S., Mamata, H., Westin, C., Jolesz, F., Mulkern, R., 2004. Biexponential diffusion tensor analysis of human brain diffusion data. Magnetic Resonance in Medicine 51 (2), 321–330.

Mair, R., Sen, P., Hürlimann, M., Patz, S., Cory, D., Walsworth, R., 2002. The narrow pulse approximation and long length scale determination in xenon gas diffusion NMR studies of model porous media. Journal of Magnetic Resonance 156 (2), 202–212.

Malcolm, J.G., Shenton, M.E., Rathi, Y., 2010. Filtered multi-tensor tractography. IEEE Transactions on Medical Imaging 29, 1664–1675.

Mangin, J., Poupon, C., Clark, C., Le Bihan, D., Bloch, I., 2002. Distortion correction and robust tensor estimation for MR diffusion imaging. Medical Image Analysis 6 (3), 191–198.

Marquardt, D., 1963. An algorithm for least-squares estimation of nonlinear parameters. Journal of the Society for Industrial and Applied Mathematics 11 (2), 431–441.

McCullagh, P., 1987. Tensor Methods in Statistics. Chapman and Hall, London.

Mendelson, K., 1990. Percolation model of nuclear magnetic relaxation in porous media. Physical Review B 41 (1), 562–567.

Menzel, M.I., Khare, K., King, K.F., Tao, X., Hardy, C.J., Marinelli, L., 2010. Accelerated diffusion spectrum imaging in the humain brain using compressed sensing. In: Proceedings of the ISMRM, Stockholm, Sweden, pp. 1–8.

Merlet, S., Deriche, R., 2010. Compressed Sensing for Accelerated EAP Recovery in Diffusion MRI. In: MICCAI, Beijing, China, p. 14. <http://hal.inria.fr/inria-00536278/en/>.

Michailovich, O., Rathi, Y., 2010. Fast and accurate reconstruction of hardi data using compressed sensing. In: Jiang, T., Navab, N., Pluim, J., Viergever, M. (Eds.), Proceedings of the Medical Image Computing and Computer-Assisted Intervention (MICCAI), Lecture Notes in Computer Science, vol. 6361. Springer, Berlin/Heidelberg, pp. 607–614.

Michailovich, O., Rathi, Y., Shenton, M., 2008. On approximation of orientation distributions by means of spherical ridgelets. In: Proceedings of the Int. Symp. on Biomedical Imaging, pp. 939–942.

Michailovich, O.V., Rathi, Y., Dolui, S., 2010. Spatially regularized compressed sensing of diffusion MRI data. CoRR abs/1009.1889.

Mitra, P., Halperin, B., 1995. Effects of finite gradient-pulse widths in pulsed-field-gradient diffusion measurements. Journal of Magnetic Resonance, Series A 113 (1), 94–101.

Mitra, P.P., Sen, P.N., 1992. Effects of microgeometry and surface relaxation on nmr pulsed-field-gradient experiments: simple pore geometries. Physical Review B 45 (1), 143–156.

Mori, S., Crain, B., Chacko, V., Van Zijl, P., 1999. Three-dimensional tracking of axonal projections in the brain by magnetic resonance imaging. Annals of Neurology 45 (2).

Moritani, T., Ekholm, S., Westesson, P., 2004. Diffusion-Weighted MR Imaging of the Brain. Springer-Verlag.

Moseley, M.E., Cohen, Y., Kucharczyk, J., Mintorovitch, J., Asgari, H.S., Wendland, M.F., Tsuruda, J., Norman, D., 1990. Diffusion-weighted MR imaging of anisotropic water diffusion in cat central nervous system. Radiology 176 (2), 439–445.

Neji, R., Azzabou, N., Paragios, N., Fleury, G., 2007. A Convex Semi-definite Positive Framework for DTI Estimation and Regularization. Lecture Notes in Computer Science 4841, 220.

Neuman, C., 1974. Spin echo of spins diffusing in a bounded medium. The Journal of Chemical Physics 60, 4508.

Niendorf, T., Dijkhuizen, R., D.G., N., van Lookeren, C.M., Nicolay, K., 1996. Biexponential diffusion attenuation in various states of brain tissue: implications for diffusion-weighted imaging. Magnetic Resonance in Medicine 36, 847–857.

Onsager, L., 1931a. Reciprocal relations in irreversible processes: I. Physical Review 37 (4), 405–426.

Onsager, L., 1931b. Reciprocal relations in irreversible processes: II. Physical Review 38 (12), 2265–2279.

Özarslan, E., Koay, C., Basser, P., 2008. Simple harmonic oscillator based estimation and reconstruction for one-dimensional q-space. In: Proc. Intl. Soc. Mag. Reson. Med., vol. 16, p. 35.

Özarslan, E., Mareci, T., 2003. Generalized diffusion tensor imaging and analytical relationships between diffusion tensor imaging and high angular resolution diffusion imaging. Magnetic Resonance in Medicine 50 (5), 955–965.

Özarslan, E., Sherperd, T.M., Vemuri, B.C., Blackband, S.J., Mareci, T.H., 2006. Resolution of complex tissue microarchitecture using the diffusion orientation transform (dot). NeuroImage 31, 1086–1103.

Özarslan, E., Vemuri, B., Mareci, T., 2005. Generalized scalar measures for diffusion MRI using trace, variance, and entropy. Magnetic Resonance in Medicine 53 (4).

Pajevic, S., Pierpaoli, C., 1999. Color schemes to represent the orientation of anisotropic tissues from diffusion tensor data: application to white matter fiber tract mapping in the human brain. Magnetic Resonance in Medicine 42 (3), 526–540.

Papadakis, N., Xing, D., Houston, G., Smith, J., Smith, M., James, M., Parsons, A., Huang, C., Hall, L., Carpenter, T., 1999. A study of rotationally invariant and symmetric indices of diffusion anisotropy. Magnetic Resonance Imaging 17 (6), 881.

Parker, G., Alexander, D., 2003. Probabilistic Monte Carlo based mapping of cerebral connections utilising whole-brain crossing fibre information. Lecture Notes in Computer Science, 684–696.

Peled, S., Friman, O., Jolesz, F., Westin, C., 2006. Geometrically constrained two-tensor model for crossing tracts in DWI. Magnetic Resonance Imaging 24 (9), 1263–1270.

Pennec, X., Fillard, P., Ayache, N., 2006. A Riemannian framework for tensor computing. International Journal of Computer Vision 66 (1), 41–66.

Perrin, M., Poupon, C., Rieul, B., Leroux, P., Constantinesco, A., Mangin, J., LeBihan, D., 2005. Validation of q-ball imaging with a diffusion fibre-crossing phantom on a clinical scanner. Philosophical Transactions of the Royal Society B: Biological Sciences 360 (1457), 881.

Pickalov, V., Basser, P.J., 2006. 3D tomographic reconstruction of the average propagator from MRI data. In: Proceedings of the ISBI, p. 710–713.

Pierpaoli, C., Basser, P.J., 1996. Toward a quantitative assessment of diffusion anisotropy. Magnetic Resonance Medicine 36 (6), 893–906.

Pipe, J., 2009. Diffusion MRI: From Quantitative Measurement to In Vivo Neuroanatomy. Academic Press, Elsevier. Chapter: Pulse Sequences for Diffusion-weighted MRI, pp. 11–35.

Poupon, C., 1999. Détection des faisceaux de fibres de la substance blanche pour l'étude de la connectivité anatomique cérébrale. Ph.D. thesis, École nationale supérieure des télécommunications.

Poupon, C., Roche, A., Dubois, J., Mangin, J.-F., Poupon, F., 2008. Real-time MR diffusion tensor and Q-ball imaging using Kalman filtering. Medical Image Analysis 12 (5), 527–534.

Putz, B., Barsky, D., Schulten, K., 1992. Edge enhancement by diffusion in microscopic magnetic resonance imaging. Journal of Magnetic Resonance 97, 27–53.

Radon, J., 1917. Über die Bestimmung von Funktionen durch ihre Integralwerte längs gewisser Mannigfaltigkeiten. Berichte Sächsische Akademie der Wissenschaften, Leipzig, Mathematisch-Physikalische Klasse 69, 262–277.

Ramirez-Manzanares, A., Cook, P., Gee, J., 2008. A comparison of methods for recovering intra-voxel white matter fiber architecture from clinical diffusion imaging scans. In: Proceedings of the 11th International Conference on Medical Image Computing and Computer-Assisted Intervention – Part I. Springer, pp. 305–312.

Rathi, Y., Michailovich, O., Shenton, M., Bouix, S., 2009. Directional functions for orientation distribution estimation. Medical Image Analysis 13 (3), 432–444.

Regan, D., Kuchel, P., 2003. NMR studies of diffusion-coherence phenomena in red cell suspensions: current status. Israel Journal of Chemistry 43 (1), 45–54.

Ritchie, D., September 1998. Parametric protein shape recognition. Ph.D. thesis, University of Aberdeen, UK

Robertson, B., 1966. Spin-echo decay of spins diffusing in a bounded region. Physical Review 151 (1), 273–277.

Ron, M., Robbins, T. (Eds.), 2003. Disorders of Brain and Mind. Cambridge University Press.

Savadjiev, P., Campbell, J., Descoteaux, M., Deriche, R., Pike, G., Siddiqi, K., 2008. Labeling of ambiguous subvoxel fibre bundle configurations in high angular resolution diffusion MRI. NeuroImage 41 (1), 58–68.

Savadjiev, P., Campbell, J., Pike, G., Siddiqi, K., 2006. 3D curve inference for diffusion MRI regularization and fibre tractography. Medical Image Analysis 10 (5), 799–813.

Sen, P., Hürlimann, M., de Swiet, T., 1995. Debye-Porod law of diffraction for diffusion in porous media. Physical Review B 51 (1), 601–604.

Seunarine, K., Alexander, D., 2006. Linear persistent angular structure MRI and non-linear spherical deconvolution for diffusion MRI. In: Proceedings of the ISMRM, p. 2726.

Smoluchowski, M.V., 1916. Drei vortrage uber diffusion, brownsche bewegung und koagulation von kolloidteilchen. Zeitschrift fur Physik 17, 557–585.

Stalling, D., Hege, H., 1995. Fast and resolution independent line integral convolution. In: Proceedings of the 22nd Annual Conference on Computer Graphics and Interactive Techniques. ACM, New York, NY, USA, pp. 249–256.

Stejskal, E., 1965. Use of spin echoes in a pulsed magnetic-field gradient to study anisotropic, restricted diffusion and flow. The Journal of Chemical Physics 43 (10), 3597–3603.

Stejskal, E., Tanner, J., 1965. Spin diffusion measurements: spin echoes in the presence of a time-dependent field gradient. Journal of Chemical Physics 42, 288–292.

Stepisnik, J., 1981. Analysis of NMR self-diffusion measurements by a density matrix calculation. Physica B 104, 350–364.

Stewart, G., Stewart, G., 1973. Introduction to Matrix Computations. Academic press, New York.

Su, Z., Coppens, P., 1994. Rotation of real spherical harmonics. Foundations of Crystallography 50 (5), 7673.

Tanner, J., 1978. Transient diffusion in a system partitioned by permeable barriers. application to nmr measurements with a pulsed field gradient. The Journal of Chemical Physics 69 (4), 1748–1754.

Tanner, J., Stejskal, E., 1968. Restricted self-diffusion of protons in colloidal systems by the pulsed-gradient, spin-echo method. Journal of Chemical Physics 49, 1768–1777.

Torrey, H.C., 1956. Bloch equations with diffusion terms. Physical Review 104 (3), 563–565.

Tournier, J., Calamante, F., Connelly, A., 2007. Robust determination of the fibre orientation distribution in diffusion MRI: non-negativity constrained super-resolved spherical deconvolution. NeuroImage 35 (4), 1459–1472.

Tournier, J., Calamante, F., Gadian, D., Connely, A., 2004. Direct estimation of the fiber orientation density function from diffusion-weighted MRI data using spherical deconvolution. NeuroImage 23, 1179–1185.

Tournier, J., Yeh, C., Calamante, F., Cho, K., Connelly, A., Lin, C., 2008. Resolving crossing fibres using constrained spherical deconvolution: validation using diffusion-weighted imaging phantom data. NeuroImage 42 (2), 617–625.

Tristan-Vega, A., Westin, C.-F., Aja-Fernandez, S., 2009. Estimation of fiber orientation probability density functions in high angular resolution diffusion imaging. NeuroImage 47 (2), 638–650.

Tschumperlé, D., 2002. Pde's based regularization of multivalued images and applications. Ph.D. thesis, Université de Nice-Sophia-Antipolis, UFR Sciences.

Tschumperlé, D., Deriche, R., 2003a. Tensor field visualization with pde's and application to dt-mri fiber visualization. In: Proceedings of the VLSM, Nice, France, pp. 255–262.

Tschumperlé, D., Deriche, R., 2003b. Variational frameworks for DT-MRI estimation, regularization and visualization. In: Proceedings of the Ninth IEEE International Conference on Computer Vision, vol. 2, pp. 116–121.

Tschumperlé, D., Deriche, R., 2005. Vector-valued image regularization with PDEs: A common framework for different applications. IEEE Transactions on Pattern Analysis and Machine Intelligence, 506–517.

Tuch, D., 2002. Diffusion MRI of complex tissue structure. Ph.D. thesis, Harvard University – MIT Division of Health Sciences and Technology.

Tuch, D., 2004. Q-ball imaging. Magnetic Resonance in Medicine 52, 1358–1372.

Tuch, D., Reese, T., Wiegell, M., Makris, N., Belliveau, J., Wedeen, V., 2002. High angular resolution diffusion imaging reveals intravoxel white matter fiber heterogeneity. Magnetic Resonance in Medicine 48 (4).

Tuch, D., Weisskoff, R., Belliveau, J., Wedeen, V., 1999. High angular resolution diffusion imaging of the human brain. In: Proceedings of the ISMRM, p. 321.

Veretennikov, V., Koshevoi, M., Panferov, N., Pikalov, V., Rupasov, A., Semenov, O., Shikanov, A., 1992. Emission tomography of a micropinch discharge plasma. Soviet Journal of Plasma Physics 18 (2).

von dem Hagen, E., Henkelman, M., 2002. Orientational diffusion reflects fiber structure within a voxel. Magnetic Resonance in Medicine 48 (3).

Wayne, R., Cotts, R., 1966. Nuclear-magnetic-resonance study of self-diffusion in a bounded medium. Physical Review 151 (1), 264–272.

Wedeen, V., Hagmann, P., Tseng, W., Reese, T., Weisskoff, R., 2005. Mapping complex tissue architecture with diffusion spectrum magnetic resonance imaging. Magnetic Resonance in Medicine 54 (6).

Wedeen, V., Reese, T., Tuch, D., Weigl, M., Dou, J.-G., Weiskoff, R., Chesler, D., 2000. Mapping fiber orientation spectra in cerebral white matter with fourier transform diffusion MRI. In: Proceedings of the ISMRM, p. 82.

Wedeen, V., Wang, R., Schmahmann, J., Benner, T., Tseng, W., Dai, G., Pandya, D., Hagmann, P., D'Arceuil, H., de Crespigny, A., 2008. Diffusion spectrum magnetic resonance imaging (DSI) tractography of crossing fibers. NeuroImage 41 (4), 1267–1277.

Weickert, J., Hagen, H., 2006. Visualization and Image Processing of Tensor Fields. Springer, Heidelberg.

Weng, J.-C., Chen, J.-H., Kuo, L.-W., Wedeen, V.J., Tseng, W.-Y.I., 2007. Maturation-dependent microstructure length scale in the corpus callosum of fixed rat brains by magnetic resonance diffusion–diffraction. Magnetic Resonance Imaging 25 (1), 78–86.

Westin, C., Peled, S., Gudbjartsson, H., Kikinis, R., Jolesz, F., 1997. Geometrical diffusion measures for MRI from tensor basis analysis. In: Proceedings of the ISMRM, p. 1742.

Wishart, J., 1928. The generalised product moment distribution in samples from a normal multivariate population. Biometrika 20 (1), 32–52.

Wu, Y., Field, A., Alexander, A., 2008. Computation of diffusion function measures in q-space using magnetic resonance hybrid diffusion imaging. IEEE Transactions on Medical Imaging 27 (6), 858–865.

Wu, Y.-C., Alexander, A.L., 2007. Hybrid diffusion imaging. NeuroImage 36.

Yin, W., Osher, S., Goldfarb, D., Darbon, J., 2008. Bregman iterative algorithm for l-1 minimization with application to compressed sensing. SIAM Journal Imaging Sciences 1 (1), 143–168.

Zhan, W., Gu, H., Xu, S., Silbersweig, D., Stern, E., Yang, Y., 2003. Circular spectrum mapping for intravoxel fiber structures based on high angular resolution apparent diffusion coefficients. Magnetic Resonance in Medicine 49 (6), 1077–1088.

Zielinski, L., Sen, P., 2000. Relaxation of nuclear magnetization in a nonuniform magnetic field gradient and in a restricted geometry. Journal of Magnetic Resonance 147 (1), 95–103.